Julius-Maximilians-Universität Würzburg
Graduate School of Science and Technology

Doctoral thesis

for the doctoral degree

Doctor rerum naturalium (Dr. rer. nat.)

Development of Dynamic Self-Initiated Photografting and Photopolymerization

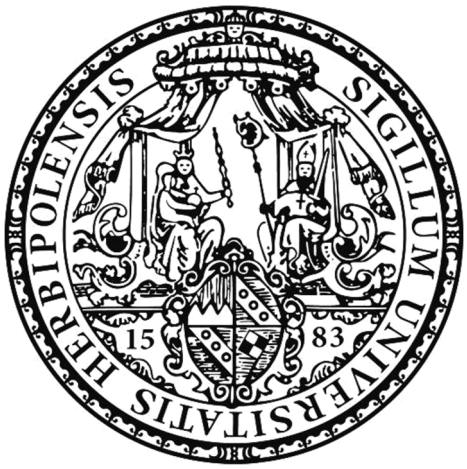

Submitted by

Jochen Löblein

from

Würzburg

Würzburg, 2021

Submitted on: August 4th, 2021

Members of thesis committee

Chairperson:
Dr. habil. Torsten Staab

1. Reviewer and Examiner:
Prof. Dr. Robert Luxenhofer

2. Reviewer and Examiner:
Prof. Dr. Paul Dalton

3. Examiner:
Dr. Rylie Green

Day of thesis defense:

December 17th, 2021

It is not our part to master all the tides of the world, but to do what is in us for the succor of those years wherein we are set, uprooting the evil in the fields that we know, so that those who live after may have clean earth to till.

— Gandalf

The presented work was done from March 2018 until Mai 2021 at the chair of chemical technology of material synthesis at the Julius-Maximilians-Universität Würzburg under the supervision of Prof. Dr. Robert Luxenhofer

Danksagung

Zuerst möchte ich Prof. Dr. Robert Luxenhofer großen Dank für die Betreuung und auch für die Hilfestellungen bei dieser Arbeit aussprechen. Ebenso hat Prof. Dr. Paul Dalton viel zum Gelingen der Arbeit beigetragen, wofür ich mich sehr bedanken möchte. Auch Dr. Rylie Green gilt mein Dank für ihren Beitrag zum Gelingen der Arbeit. Ebenfalls Dank gebührt der Volkswagen-Stiftung, die durch die Finanzierung des Projektes *„Coaxial 3D Printing of Actuating Electroactive Scaffolds for Muscle Regeneration“* die Grundlage für das Zustandekommen dieser Arbeit gelegt hat.

Großer Dank gilt auch den Mitarbeitern des Instituts, die immer gute Ansprechpartner waren und dafür gesorgt haben, dass jeder seine Arbeit machen kann. Zu nennen wären dabei Diana, Christian, Sandra, Guntram, Anna, Steffi und Frau Midtbö. Darüber hinaus möchte ich mich besonders bei meinen Kollegen Robin, Haider, Lukas, Daniel, Juliane, Julian, Stefan, Solomiia, Christine, Mira, Mengshi, Chen, Sebastian, Ezgi, Michael und Thomas für die schöne Zeit, die gute Zusammenarbeit und die tollen Gespräche bedanken. Für die Messungen und Hilfestellungen am REM möchte dabei auch Philipp Stahlhut danken, sowie Andreas Frank für die Messungen am ESEM. Für die *Dynamic Vapour Sorption*-Experimente möchte ich Stephan Braxmeier und Philipp Potsch danken. Dank gilt auch Tobias Kielholz und Prof. Dr. Maike Windbergs für die Zusammenarbeit und die Messungen am Raman-Spektrometer. Ein besonderer Dank gilt auch Julian Glock, Nadine Munker, Simon Hammer und Isabelle Böswald, die mich bei meiner Arbeit mit Abschlussarbeiten oder Praktika (oder sogar mit beidem) unterstützt haben.

Ein besonders großer Dank gilt auch meinen Freunden, die mich während meiner Doktorarbeit begleitet haben und dabei mein Leben bereichert haben: Matt, Michi, Chris, Sabine, Caro, Juli, Markus, Lena, Kathi, Catrin, Jenny, Timo, Sebastian.

Der größte Dank gilt aber meinen Eltern, die mich schon während meines Studiums unterstützt und mir damit alles erst ermöglicht haben. Ein ebenso großer Dank gilt dabei auch Stefan und Juliana, und auch meiner Freundin Franzi, die zu jeder Zeit für mich da war.

List of Publications

Hailmann, M.; Konieczka, S. Z.; Himmelspach, A.; Löblein, J.; Reiss, G. J.; Finze, M. *Inorganic Chemistry*, **2014**, *53* (17), 9385–9399.

Löblein, J.; Lorson, T.; Komma, M.; Kielholz, T.; Windbergs, M.; Dalton, P.; Luxenhofer, R. *Beilstein Journal of organic Chemistry,* **2021**, 17, 2095–2101.

Contents

List of Abbreviations

AA	acrylic acid
AIBN	Azobisisobutyronitrile
AMPS	2-acrylamido-2-methylpropane-sulphonic acid
ATRP	Atom-transfer radical polymerization
BBB	Bottle-Brush Brushes
CLPE	cross-linked polyethylene
CNC	cellulose nanocrystal
CNT	carbon nanotube
DAPI	4´,6-diamidino-2-phenylindole
DLP	digital light processing
d_{ls}	distance between light source and sample
EEMA	2-ethoxyethyl methacrylate
et al.	et alii (and others)
FDA	U.S. Food and Drug Administration
GC	glassy carbon
GO	graphene oxide
HEMA	2-Hydroxyethyl methacrylate
hESCs	human embryonic stem cells
iPSCs	induced pluripotent stem cells
IR	infrared
ISC	intersystem crossing
LCROP	living cationic ring-opening polymerization
LDPE	low density polyethylene
MAA	methacrylamid
MEDSAH	[2-(Methacryloyloxy)ethyl]dimethyl-(3-sulfoproply)ammonium hydroxide
METAC	[2-(Methacryloyloxy)ethyl]trimethylammonium chloride
MEW	Melt Electrowriting
MMA	methylmethacrylate

OEGMA	oligoethylene glycol methacrylates
P(VDF-CTFE-TrFE)	Poly(vinylidenfluoride-clorotrifluoroethylene-trifluoroethylene)
P(VDF-TrFE)	Poly(vinylidenfluoride-trifluorethylene)
P2VP	poly(2-vinylpyridine)
P4VP	poly(4-vinylpyidine)
PCL	Poly(ε-caprolactone)
PCPOEA	poly(2-(2-chloropropanoyloxy)ethyl acrylate)
PDMAEMA	Poly(N,N-dimethylaminoethyl methacrylate)
PEG	polyethylene glycol
PEGMA	polyethyleneglycol methacrylate
PET-RAFT	photoinduced electron transfer-reversible addition-fragmentation chain transfer
PGA	poly(glycolic acid)
PHEMA	poly(2-hydroxyethyl methacrylate)
PIPOx	poly(2-isopropenyl-2-oxazoline
PLA	poly(lactic acid)
PMMA	polymethylmethacrylate
PP	poly(propylene)
PS	polystyrene
PTMC	poly(trimethylene carbonate)
PVA	polyvinylalcohol
PVC	polyvinylchloride
PVDF	Polyvinylidene fluoride
RAFT	Reversible addidion-fragmentation chain transfer
r_{fl}	flow rate
RT	room temperature
S_D	swelling degree
SERS	surface enhanced Raman spectroscopy
SI-ATRP	Surface-initiated atom-transfer radical polymerization
SIPGP	Self-initiated photografting and photopolymerization
St	styrene

T_0	temperature after 0 s of irradiation
T_t	temperature after 60 s of irradiation
THR	total hip arthroplasty
t_i	irradiation time
TKA	total knee arthroplasty
TPO	diphenyl(2,4,6-trimethylbenzoyl)phosphine oxide
UNCD	ultrananocrystalline diamond
UV	ultra violet
W_d	dried weight of bulk polymer
W_s	swollen weight of bulk polymer
WST	water soluble tetrazolium

List of Symbols

°	degree
°C	degree Celsius
µ	micro, 10^{-6}
c	centi, 10^{-2}
d	day
G	gram
H	hour
Hz	hertz
J	joule
l	litre
m	meter
m	milli, 10^{-3}
min	minute
Pa	pascal
S	second
W	watt
wt%	weight percent

1 Introduction

Surface modifications are playing a major role in modern technology. The surface of a product is the part that is interacting with its environment. There are numerous reactions or coating techniques and every one of them has certain fields or applications where it is the best to use. However, with advancing science and technology the requirements for surfaces get more diverse, challenging and specific. Especially in medicine, the requirements are exceptionally high. For this reason, many materials are not suitable to be used for example as implants. However, with the right coating or coating method the number of possibly useful materials can be highly increased. So far, implants usually consist of metals, especially on their surfaces. Organic polymers on the other hand play a minor role in this field.

However, coatings can also be utilized to improve the biological properties of materials, which are already used in biomedical applications, such as PVDF (poly(vinylidenedifluoride)), which is used as hernia meshes or can be used as transvaginal meshes for cystocele repair in the future.[1,2] PVDF is commonly used as an insulator, but there are also co- and terpolymers of PVDF that show piezoelectric properties. Where the copolymer P(VDF-TrFE) (poly(vinylidenedifluoride-tetrafluorethene)) shows properties of a sensor, the terpolymer P(VDF-TrFE-CTFE) (poly(vinylidenedifluoride-tetrafluorethene-chlorotetrafluorethene) shows properties of an actuator.[3–5] Another material that is promising for a broader use in biomedicine is PCL (poly(ε-caprolactone)).[6] One of the advantages of PCL is that it's a good material for additive manufacturing, which can be used to 3D print patient specific implants. These implants are supposed to function for a scaffold-guided bone regeneration.[7] PCL is also used as "gold standard" for a more specific printing technology, the melt electrowriting (MEW). This technique is used to print scaffolds that can be used to support wound healing or can function as a placeholder or barriers for guided bone regeneration.[8] Not only PCL scaffolds can be printed via MEW, also the previously mentioned PVDF and P(VDF-TrFE) can be used to print MEW-scaffolds.[9,10]

To modify the interactions of these materials with the in vivo environment, coatings can be utilized. Already in 1960 Wichterle and Lim found, that hydrogels could be of a greater use for biomedical applications.[11] Following that, PHEMA (poly(2-hydroxyethyl methacrylate)) was used as a base material for contact lenses and proved its viability

as a material for biomedical applications.[12] Having a methacrylate functionality, HEMA can also be used to be grafted to different materials to improve the interaction of a product with cells.[13] Not only HEMA is a viable methacrylate to be utilized to graft onto other materials. Also METAC ([2-(methacryoyloxy)ethyl]trimethylammonium chloride), which is a cationic methacrylate, can be used to do so. If instead an antifouling coating is the goal, the zwitterionic monomer MEDSAH (or DEMAPS; [2-(methacryloyloxy)ethyl]dimethyl-(3-sulfoproply)ammonium hydroxide) and its according polymer PMEDSAH can provide these properties by for example grafting them to other materials via RAFT polymerization (reversible-addition-fragmentation chain-transfer polymerization).[14–16]

However, RAFT polymerization as well as other photochemical polymerization methods need initiators or other reagents for the reaction, which can be harmful to living organisms and have to be removed before being used in biomedical applications. In 2001, Deng, Yang and Rånby discovered the basics for the mechanism of SIPGP (self-initiated photografting and photopolymerization), which does not need any additional reagents than the surface and the monomers.[17] The following work will focus on further developing this surface modification technique.

2 State of Knowledge

The most common types of implants these days are total hip arthroplasties (THR) and total knee arthroplasties (TKA). In 2011 in Germany, cases for hip implants were 284 per 100.000 residents and in the USA 204 cases per 100.000 residents. Knee implant surgeries were 304 in the USA and 206 per 100.000 residents in Germany, while the numbers are going up.[18] The knee society knows 22 different complications or adverse events due to TKA, where the hip society knows 19 of those in 5 different grades of severness.[19,20] While the complication rates for total hip arthroplasties is decreasing since the last decades from 9.9 % in the 1990s to 5.3 % in the 2010s (results until 2019), the rates must still be decreased to lower the patient suffering as well as the need for post-operative care or surgery.

These examples show the need of improved implant techniques as well as improved implants not only for hip or knee implants, but also for every type of implant in the present or future. Surface modifications are one way to improve implants according to complications such as inflammation reactions of the body at the site of the implant.

2.1 Coatings on Inorganic Implant Materials

Already in 1987 Wisbey *et al.* developed a TiN coating for implants. In this time the implants for joint arthroplasties consisted of a Co-Cr-Mo alloy. These implants however, were reported to cause clinical problems due to a release of metal ions contained in these implants. Their solution was to coat these implants with TiN via electron beam evaporation. This lead to an enhanced corrosion resistance of the implant as well as a reduction of release of harmful metal ions.[21] Although implants these days consist of titanium, these TiN coatings are still used and improved. In order to coat titanium implants with an antimicrobial coating, Bergemann *et al.* found that copper can be utilized. To do so they modified the surface of the titanium by using a titanium plasma spray. After that, they coated the sample with a titanium-copper-nitride layer by physical vapour deposition. They found that their coating had a strong antibacterial influence and by simulating *in vivo* dynamics through medium exchange they were also able to reduce cytotoxic effects on osteoblasts.[22] Similar results to minimize bacterial adhesion and promote osteoblast activity can be achieved by using $CaSiO_3$, SiC or TiC coatings.[23–26] These characteristics were also reported for hydroxyapatite coatings by Ducheyne *et al.* in 1985, which were applied by electrophoretic deposition.[27] These coatings are still in the focus of development and can be applied by a variety of different methods such as sol-gel coating, plasma spraying, biomimetic deposition, electrochemical deposition and electrophoretic deposition.[28–34]

Inorganic coatings are not only capable of increasing stability, but can also be designed to intentionally be degraded inside the human body. Mg-Ca alloys were reported to have a similar young modulus and mechanical strength than bone and thus can be used as resorbable implants. Only the degradation was too fast to be used as an implant.[35] Thomann *et al.* then introduced an MgF_2 coating for these implants. These coatings were performed by immersing the substrates in a sodium hydroxide solution to create a magnesium hydroxide surface. Following, the substrates were bathed in hydrofluoric acid. This chemically applied coating was able to reduce degradation rate while keeping cytocompatibility.[36]

Not only inorganic coatings can be used. Also biological or drug loaded coatings are being investigated. Collagen type-I can be used as a coating on titanium alloys by

using absorption. This coating can increase the bone remodelling around these implants.[37] Also bioactive titanium oxide coatings, which increase not only osseointegration but also implant fixation as they are, can be coated with antibiotics such as gentamicin. To do so, the modified substrates must be immersed in a gentamicin solution with evaporation of the solution afterwards. By doing so bacterial growth can be suppressed and bacterial contamination prevented.[38] Growth factors are being used as a drug loaded in coatings, as Schmidmair *et al.* did with different growth factors being loaded into a poly (D,L-lactide) coating. This biodegradable coating can release drug over a time of more than 42 d.[39]

2.2 Coatings on Polymeric Implant Materials

2.2.1 Polymeric Implant Materials

2.2.1.1 Poly(ε-caprolactone)

When it comes to biodegradable polymers for biomedical applications, polyesters are an important group in that field. Among them are poly(lactic acid) (PLA), poly(glycolic acid) (PGA), and poly(ε-caprolactone) (PCL).[40–42] Compared to those, PCL (Figure 1) has a longer degradation time of up to 2-3 years due to its hydrophobicity and semi-crystallinity. This degradation time however, is also dependent on molecular weight, residual monomer content, shape and autocatalysis amongst others. Using these parameters the degradation time can be adjusted according to needs.[43–45]

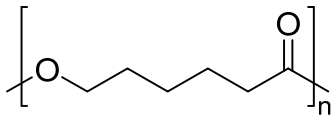

Figure 1: *Chemical structure of poly(ε-caprolactone).*

Due to its biodegradation properties, PCL is capable of being drug-loaded and releasing the drug, such as dexamethasone, vancomycin, praziquantel or ibuprofen, over time.[46–49] To use the advantages of more than one material, composites can be utilized. There are different types of composites that are being developed for PCL. Electrospun PCL-gelatine micro-/nanofiber can be used as membrane for guided tissue regeneration.[50] Also organic/inorganic composites were investigated. For example β-tricalcium phosphate-PCL nanocomposites for bone implants, SiO_2-PCL hybrid materials containing quercetin for antioxidant implants or rBMSC (rat bone marrow-derived mesenchymal stem cell) laden hydroxyapatite-PCL to promote osteogenesis and angiogenesis.[51–54]

As shown, the application range of PCL is a broad one. Including compositions and blends it can be used for example as mesh-, bone-, knee-, hip, or ocular implants.[7,46,51,55–58]

2.2.1.2 PVDF and Derivatives

In 1984 Häusler *et al.* proposed PVDF (Figure 2 left) as an implantable indefinite power supply for implants that require to be powered constantly. The piezoelectric properties of PVDF were supposed to be triggered enough through the movement of ribs while breathing. By implanting their device into a dog they managed to gain a power of 17 µW with the amplitude being constant for 3 h until they terminated the experiment.[59] A variety of approaches to use PVDF and its derivatives as implantable batteries are still actively investigated.[60,61] One of these applications are 3-dimensional microsystems for vibrational energy harvesting.[62] However, not only energy harvesting is a reason to choose PVDF for implants. Also sound detection was reported to be able to use in cochlear implants. With a PVDF-based microphone Park *et al.* proposed a totally implantable cochlear implant in opposition to the partially external ones used so far.[63]

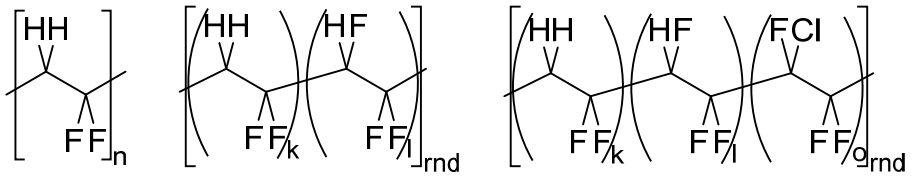

Figure 2: *Chemical structures of PVDF (left), P(VDF-TrFE) (middle) and P(VDF-TrFE-CTFE) (right).*

Due to its cytocompatibility and low tissue responses, PVDF is being used and researched for different types of implants without utilizing the piezoelectric properties. For example as a substitution for poly(propylene) (PP) as a mesh for abdominal hernia repair.[64,65] There PVDF is commonly used since for these surgeries a polymer with high degradation resistance is desired due to a reduction of recurrence.[2,66,67] Also cystocele repair is a field where PVDF meshes are currently investigated.[1]

In recent years, also the copolymer P(VDF-TrFE) (Figure 2 middle) and the terpolymer P(VDF-TrFE-CTFE) (Figure 2 right) have been in the focus of research, because through these co- and terpolymers the piezoelectric properties of PVDF can be adjusted.[5,68] While P(VDF-TrFE) is researched as a membrane for wound healing, neural and bone tissue engineering, P(VDF-TrFE-CTFE) is just recently being discovered as an implant material.[69–72]

2.2.1.3 Melt Electrowriting

Brown, Dalton, and Hutmacher invented melt electrowriting (MEW) in 2011 (called melt electrospinning writing back then).[73] It is an additive manufacturing method derived from melt electrospinning. A big potential difference between the nozzle and the collector can be used to form the polymer melt at the tip of the needle into a Taylor Cone, which allows the printing of fibres in a low micrometer range without using solvents.[74] During the process the printing head is heated for keeping the polymer melted (Figure 3). Another important part of MEW is the moving collector. This allows the "writing" of the fibres and thus the printing of scaffolds having a fibre spacing of up to 20 µm, unlike melt electrospinning, where the pore size is very small associated with the random layering of the fibres.[73]

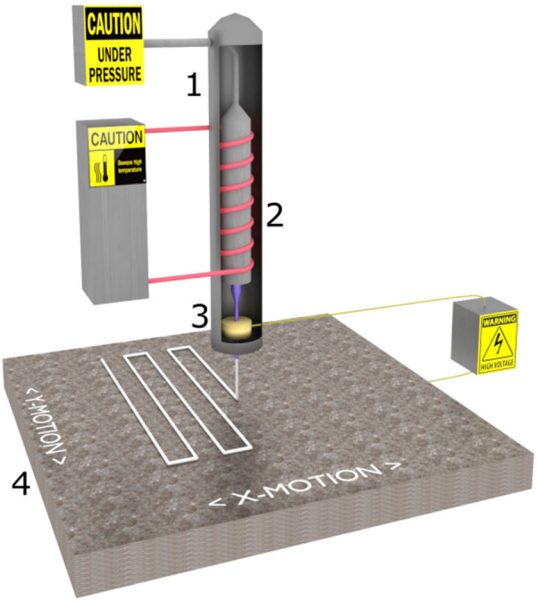

Figure 3: *MEW printer containing a pressure unit (1), polymer melt reservoir with heating unit (2), the nozzle (3) and the moving collector (4).*

PCL is the "gold standard" of MEW and was the first polymer to be printed via MEW.[73] Since then a variety of other polymer was processed with MEW, for example poly(urea-siloxane), poly(2-ethyl-2-oxazoline) or poly(propylene).[75–77] In 2018 Florczak *et al.* managed to print PVDF via MEW, while showing piezoelectric responses after the printing process.[9] Also P(VDF-TrFE) was reported to be printable via MEW in 2021 by Kade *et al.*[10]

2.2.2 Coating materials for polymeric implants

PCL, PVDF and its derivatives are a good choice to be used as polymeric implants. Never the less, surface modifications still can improve or adjust their properties according to need. There is a huge variety of possible coatings for polymeric implants. PVDF for example was coated with star-PEG (polyethylene glycol) via spin coating. A subsequent modification of star-PEG with RGD-sequences then enabled protein repellent and cell adhesive properties of the surface.[78] A similar anti-fouling coating for PVDF was fabricated with amino acid modified PEG, or a polyphenol tannic acid/polyethylenimine/metal ion coating.[79,80] A chitosan coating can also be prepared on PVDF via dip coating, as well as on PCL, and can function for example as a drug release coating.[81,82] Electrospun PCL nanofibers were also coated with polysaccharides for wound dressing applications via ionic layer-by-layer deposition.[83]

2.2.2.1 PHEMA

A material that is outstanding and in the focus of researchers for biomedical applications for more than 50 years now is poly(2-hydroxyethyl methacrylate) (PHEMA), (Figure 4) with its monomer HEMA.[84] Since its discovery PHEMA was heavily investigated, and even approved by the FDA (U.S. Food and Drug Administration) for ocular applications such as contact lenses.[12,85–88]

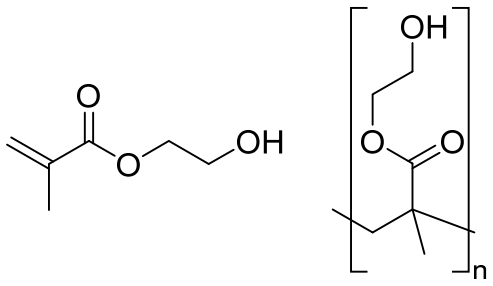

Figure 4: *Chemical structure of HEMA (left) and PHEMA (right).*

PHEMA can also be utilized as a coating material. Being a methacrylate enables HEMA to be polymerized via initiator aided radical polymerization. One way to do so is to use the physical sorption of the initiator AIBN (Azobisisobutyronitrile) to a PVC (polyvinylchloride) film. The so prepared film can now be placed into the HEMA solution and be polymerized via UV-light.[89,90] Another popular initiator is Irgacue 2959 or, if coated to a metallic surface such as titanium, an electrochemical initiator such as ammonium peroxydisulfate ($(NH_4)_2S_2O_8$) can be used to perform the PHEMA coating.[88,91] More methods of grafting PHEMA from surfaces will be described in more detail in chapter 2.2.3. PHEMA surface modifications can be used as anti-fouling coatings for ventricular catheters as Hanak *et al.* showed in their in vitro study.[92] However, it can also be used as a drug releasing coating. It is capable of loading and releasing drugs, such as nerve growth factors, proxyphylline or doxorubicin.[93–95]

HEMA can be co-polymerized with a huge variety of acrylates, methacrylates and acrylamids such as AA (acrylic acid), METAC ([2-(methacryloyloxy)ethyl]trimethylammonium chloride), PEGMA (polyethyleneglycol methacrylate), MMA (methylmethacrylate) or MAA (methacrylamid).[16,96–99]

2.2.2.2 PMEDSAH

The monomer [2-(methacryloyloxy)ethyl]dimethyl-(3-sulfoproply)ammonium hydroxide (MEDSAH or sometimes DMAPS) can be photochemically polymerized to fabricate a zwitterionic polymer (Figure 5).

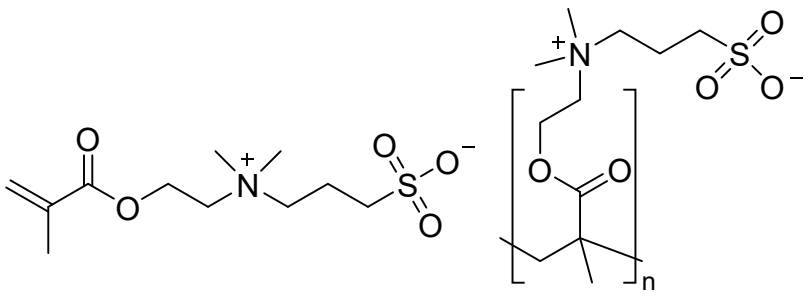

Figure 5: *Chemical structure of MEDSAH (left) and its polymer PMEDSAH (right).*

In 2010 Villa-Diaz *et al.* reported, that PMEDSAH can be used as a coating for long-term growth of human embryonic stem cells (hESCs).[100] Following that, human-induced pluripotent stem cells (iPSCs) were cultured on PMEDSAH coated substrates. As the hESCs, the iPSCs maintained pluripotent and were still able to be differentiated in vivo or in vitro.[101–105] Besides stem cell research, PMEDSAH is known as a material with non-biofouling properties due to its zwitterionic character.[106–109] The non-biofouling behaviour of PMEDSAH is even more effective than that of PHEMA.[106] For that reason, it is a highly interesting polymer in research for biomedical applications. There are two main ways to graft PMEDSAH to surfaces, the SI-ATRP and the RAFT mechanism. Using these mechanisms leads to polymer brushes of PMEDSAH on the surface of the substrates.[108–116] Both will be described in more detail in chapter 2.2.3. Besides photo-induced polymerization PMEDSAH can also be polymerized thermo-induced, to achieve a geometry-independent homogeneous layer thickness of PMEDSAH.[117] In 2018 Lim *et al.* reported, that PMEDSAH can be polymerized on CLPE (cross-linked polyethylene) to achieve a low dynamic friction coefficient. They predict PMEDSAH to be used in artificial joints, since CLPE is currently used as a material for hip-joints. The low dynamic friction coefficient of PMEDSAH can then lead to reduce wearing debris.[118] Following this, Osaheni *et al.* reported in 2020, that PMEDSAH can additionally be used as a reservoir for lubricant and thus can be used for a variety of biomedical applications such as articular cartilage repair, guide wire coatings and soft contact lenses.[119]

2.2.2.3 PMETAC

The methacrylate [2-(methacryloyloxy)ethyl]trimethylammonium chloride (METAC) is a cationic monomer, that forms a high swelling hydrogel as the polymer PMETAC (Figure 6).[120]

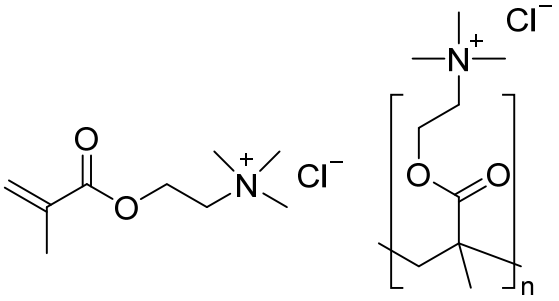

Figure 6: *Chemical structure of METAC (left) and PMETAC (right).*

Osborne *et al.* first synthesized PMETAC as polymer brushes in 2002 as part of triblock polymer electrolyte brushes consisting of a cationic a neutral and an anionic block, with PMETAC being the cationic block. The mechanism they used for polymerization was ATRP, which will be described in chapter 2.2.3.1.[121] One year later METAC and HEMA were co-polymerized in bulk to be tested as hydrogels for biomedical applications. In this contribution, Rosso *et al.* reported, that a copolymer of HEMA and METAC with a molar ratio of HEMA:METAC 10:1 showed no cytotoxicity and good cell adhesion compared to an anionic copolymer of HEMA and AMPS (2-acrylamido-2-methylpropanesulphonic acid).[122] HEMA and METAC were then also polymerized in the presence of alginate to form a semi interpenetrating hydrogel. La Gatta *et al.* reported, that this hydrogel is appropriate for cell adhesion and proliferation and suggests it as a good material for biomedical applications.[16] Different cell types were tested with a copolymer of HEMA and METAC. Endothelial cells for example show good adhesion, with a high ratio of METAC.[123] Neuronal cells in contrast show better adhesion with lower ratios of METAC. This way neuronal cell patterns can be produced by using a HEMA-METAC copolymer with a good adhesion to these cells and the PMETAC homopolymer, which repels neuronal cells.[124,125] HEMA is not the only monomer used for copolymerization with METAC. A copolymer with vinyl alcohol is used for removing chromium (VI) from water.[126] Another example is a copolymer of PEG and METAC. This can be used for

pH-responsive delivery of insulin.[127] PMETAC can be used for antifungal nanocomposites, an antimicrobial brush surface, cell culturing, a flocculent for harvesting microalgae or recently in a ultra-low lubricity hydrogel network.[128–132]

This shows that METAC is a very versatile monomer to be used for biomedical applications.

2.2.3 Coating techniques

To achieve a polymer coating, there are two different approaches. The *grafting from* and the *grafting to* mechanism. While *grafting to* describes two different pre-existing materials, that will be covalently connected, the *grafting from* mechanism describes a continuous growth of one material from the surface of another material. The previously mentioned materials find application in grafting from mechanisms. There are mainly three different *grafting from* mechanisms that are utilized to graft methacrylates: *atom transfer radical polymerization* (ATRP), *reversible addition-fragmentation chain transfer* (RAFT) and *self-initiated photografting and photopolymerization* (SIPGP). Following, these three *grafting from* methods will be described in more detail.

2.2.3.1 Atom Transfer Radical Polymerization

The mechanism of ATRP is relying on an equilibrium between the active species and a metal complex.[133] For the initiation an alkyl halide and a metal complex are needed. In Scheme 1 a Cu^{I} complex and an alkyl chloride are used. As metal centres also Fe^{II} or Ru^{I} can be used.[134,135]

Initiation:

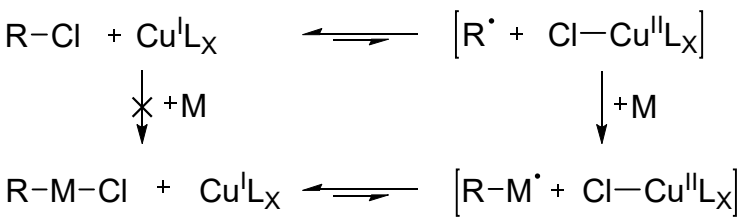

Propagation:

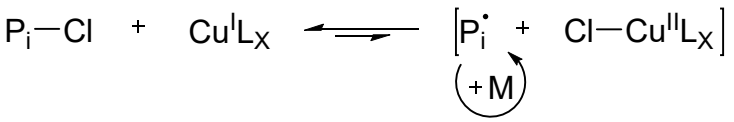

Scheme 1: *Initiation and propagation mechanism of ATRP. R = alkyl group; M = monomer; P_i = propagating species; L = ligand. Adapted with permission from reference.[133] ©2021 American Chemical Society.*

By oxidation of the metal complex an alkyl radical is formed, while being in an equilibrium with the reduction reaction, which is faster than the oxidation. The radical then reacts with one of the monomers. This active species is underlying the same redox equilibrium as the initiating species, which means that with reducing the metal complex, a dormant species is formed. This way the propagation is slowed down, which leads to more defined chain lengths. In addition, disproportionation reactions and termination reactions are suppressed.[133] For these reasons ATRP is a controlled radical polymerization and sometimes even considered to be a “living” polymerization.[129,133,136–138]

Because the ATRP suffered from so called *mini emulsion droplets* (small droplets that form mini-bulk systems and lead to an insufficient distribution of the reactants), different ways of initiating were researched.[137] The simultaneous reverse & normal initiation (SR&NI) process uses conventional radical initiators for initiating the polymerization. This improved the emulsion problem, but pure block polymers could not be fabricated.[137] Another way is the *activator generated by electron transfer* (AGET). In this mechanism a reducing agent is added, that reduces the metal complex without any alkyl halide involved.[137,139–142] If a very active copper catalyst is added, the activators are continuously regenerated. The mechanism is then called *activators continuously*

regenerated by electron transfer (ARGET) ATRP.[139,140,143–145] ATRP can also be combined with click reactions to perform a *grafting to* method. To do so polymer chains are formed via ATRP and then terminated with an appropriate end group for click reactions.[146]

ATRP can also be utilized as a *grafting from* mechanism, by having alkyl halogenides on top of a surface. In 2002 Osbourne *et al.* formed alkyl bromides as self-assembled monolayers (SAMs) on top of an Au-surface. The bromides then induced the polymerization of brushes on top of the Au-surface.[147] Liu *et al.* then grafted polymethylmethacrylate (PMMA) from surface modified carbon fibres by using surface-initiated atom-transfer radical polymerization (SI-ATRP).[148] This way HEMA was *grafted from* surfaces to form anti-fouling coatings as well as a HEMA-METAC copolymer.[16,149] SI-ATRP was since then researched and proposed for a variety of biomedical applications such as pectinase immobilization, osseointegration of titanium surfaces, non-fouling surfaces or bioelectrodes.[149–154]

Although ATRP and SI-ATRP have proven to fabricate well suited surfaces for biomedical applications, the removal of the toxic metal complexes was a problem ever since. Different methods to remove these metal complexes have been discovered, but never the less they mean an additional procedure step and additional costs.[155–158]

2.2.3.2 Reversible Addition-Fragmentation chain transfer

Another mechanism that is considered controlled or “living” is the reversible addition-fragmentation chain transfer (RAFT). As ATRP, the controlling nature of RAFT is relying on an equilibrium between the propagating species and the dormant species (Scheme 2).

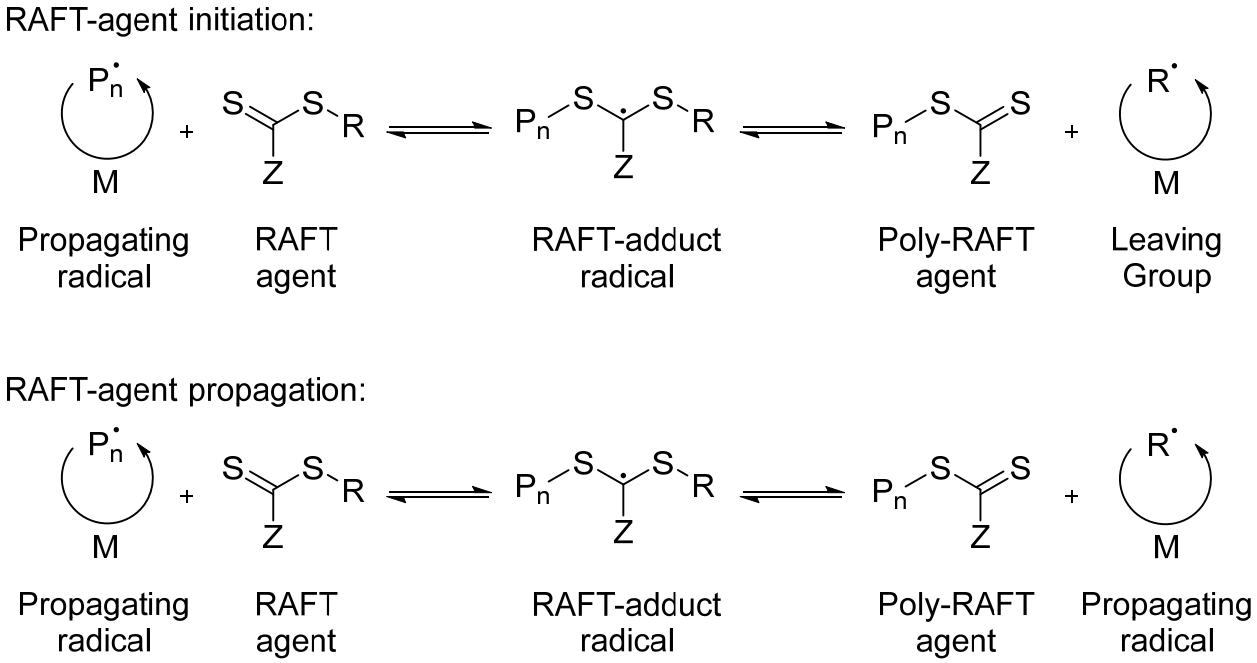

Scheme 2: *Initiation and propagation mechanism of RAFT by the RAFT-agent. Z = substituent for leaving group; R = alkyl group; P_n, P_m = propagating species. Adapted with permission from reference.[159] ©2021 Wiley.*

To achieve that, a RAFT agent is utilized. This RAFT agent often is a dithioester with two groups of variation. One is the activating group Z, which is designed to stabilize the RAFT-adduct radical. A variety of substitutes are used for Z such as phenyl, benzyl, methyl or pyrrole amongst others.[160–163] The leaving group R is even more diverse than Z is. R is a homolytic cleaving group and common groups for R are CH_2Ph, $CH(CH_3)Ph$ or $C(CH_3)_2Ph$.[161,164,165] The initiation of RAFT is carried out by a “standard” radical initiator such as AIBN or benzoyl peroxide.[166] The so formed propagating radical reacts with the RAFT agent and forms the RAFT-adduct radical. This radical now has two leaving groups, the R group and the propagating species. As previously mentioned, R is designed to be the better leaving group and thus initiates a new polymerization chain, while the dormant species, the poly-RAFT agent, is formed. To now achieve control

over the system, it must be ensured, that the concentration of the dormant species is magnitudes greater than the concentration of the active species.[159] As ATRP, this mechanism allows control over the chain length and distribution, however termination through combination of two active species are still occurring, which makes RAFT to be considered “living” debateable.[167]

The mechanism of RAFT was discovered by Moad, Rizzardo, Thang and co-workers in 1998.[166] Following that they used RAFT to form block polymers in 2000.[165] One year later Tsujii *et al.* reported the first *grafting from* mechanism of RAFT. To do so they first used ATRP to graft polystyrene from silicon particles. Following, they introduced a RAFT moiety to the end chain of the graft polymer and thus could initiate a RAFT polymerization as a *grafting from* mechanism.[168] RAFT can not only be utilized as a *grafting from* mechanism, but also as a *grafting to* mechanism as Park and Thomas showed in 2002 or used as a tandem RAFT and Click polymerization in a one-pot reaction as Ranjan and Brittain reported in 2007.[169–171] The surface modification ability of RAFT raises the interest to use it for biomedical applications. First it was reported, that RAFT can be utilized to directly graft brushes from cellulose or chitosan.[163,172,173] Then also bovine serum albumin was grafted via RAFT or proteins were modified to function as a RAFT agent.[174–176] With biomaterials in perspective, RAFT was utilized to graft PMMA on stainless steel to improve its biological properties.[177] Also PHEMA was grafted as brushes from silicon wafers to form a protein resistant surface.[178] In 2014 Shanmugam *et al.* reported the photoinduced electron transfer-reversible addition-fragmentation chain transfer (PET-RAFT), which allowed them to initiate the RAFT polymerization by green light, which reduces the influence of oxygen on the initiation phase of RAFT.[179,180] Using PET, MEDSAH was surface grafted from polyvinylalcohol (PVA) to form an optical biomaterial.[115]

Besides that, RAFT was investigated for a number of different biomedical applications such as drug delivery, stimuli responsive polymers or imaging of cells.[174,175,181–185] However, as with ATRP, the RAFT-agents can cause toxicity problems.[186] After the reaction the RAFT-agent forms the end group of the polymer and is susceptible for hydrolysis especially with increasing temperature or pH.[187] For this reason an additional processing step must be taken to remove the dithioester group, which however can be utilized to introduce a variety of different functional groups as endgroups.[188]

There is a radical polymerization method, which allows the omission of toxic reagents or initiators. This technique will be described in the following chapter.

2.2.3.3 Self-Initiated Photografting and Photopolymerization

To perform photopolymerization, usually an initiator or specific reagents are needed. These reagents are often toxic, due to their reactivity (as discussed in the previous chapters). For that reason there are still efforts being made to reduce toxicity by using different reagents or applying cleaning processes.[189–193] Another interesting approach is to not use any initiators or reagents at all, as self-initiated photografting and photopolymerization (SIPGP) does. In contrast to ATRP and RAFT, SIPGP is not considered to be a controlled or living polymerization. It instead relies on the “classical” reactions of photopolymerization without trying to suppress some of the reaction routes (Scheme 3). The initiation process is carried out by an initiator (here diphenyl(2,4,6-trimethylbenzoyl)phosphine oxide (TPO)) to form a radical. This radical then reacts with a monomer (here HEMA) and forms the propagating species. This way the polymer chains start to grow. This species also can abstract a hydrogen atom from another species (reactive or not). Through that it gets inactive, but the other species becomes active or gets an additional active end (chain transfer). This way three dimensional networks are being formed. The chain reaction can propagate until two radical ends react and form an unreactive species (termination).

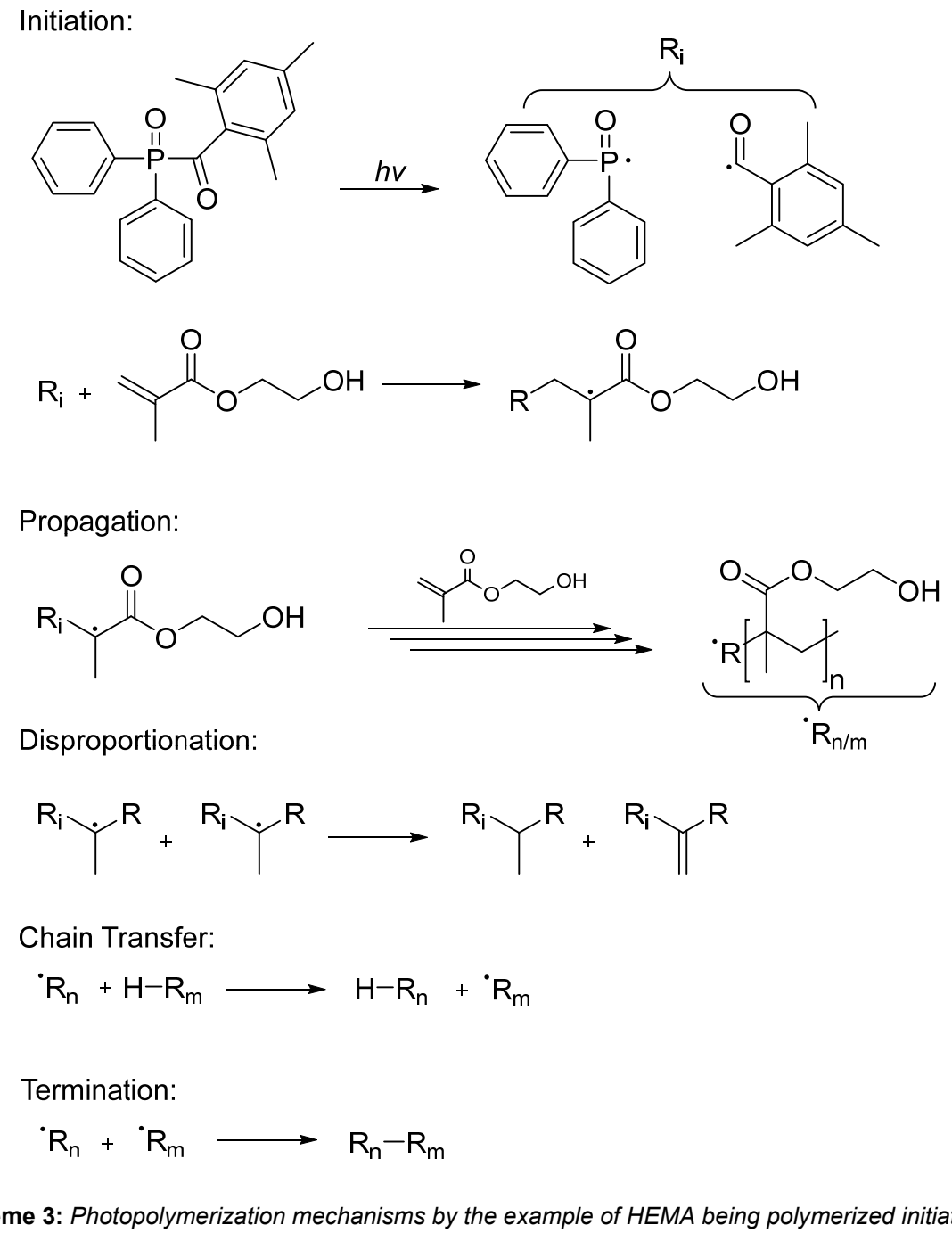

Scheme 3: *Photopolymerization mechanisms by the example of HEMA being polymerized initiated by diphenyl(2,4,6-trimethylbenzoyl)phosphine oxide (TPO).*

SIPGP instead introduces an alternative initiation process. To do so, the surface must contain an abstractable hydrogen and the monomers used must have a sterically accessible C=C double bond (explanation in more detail in the following chapters). If these requirements are fulfilled, induced by UV-light the C=C double bond gets excited and forms a biradical. This biradical then can abstract the hydrogen on the surface and thus generate a radical on top of the surface. The primary as well as the tertiary radical

are able to abstract the hydrogen. However, it is much more likely that the primary radical does so, since it is more exposed and less stabilized than the tertiary one is.

This surface radical then initiates the photografting and the photopolymerization, (Scheme 4).

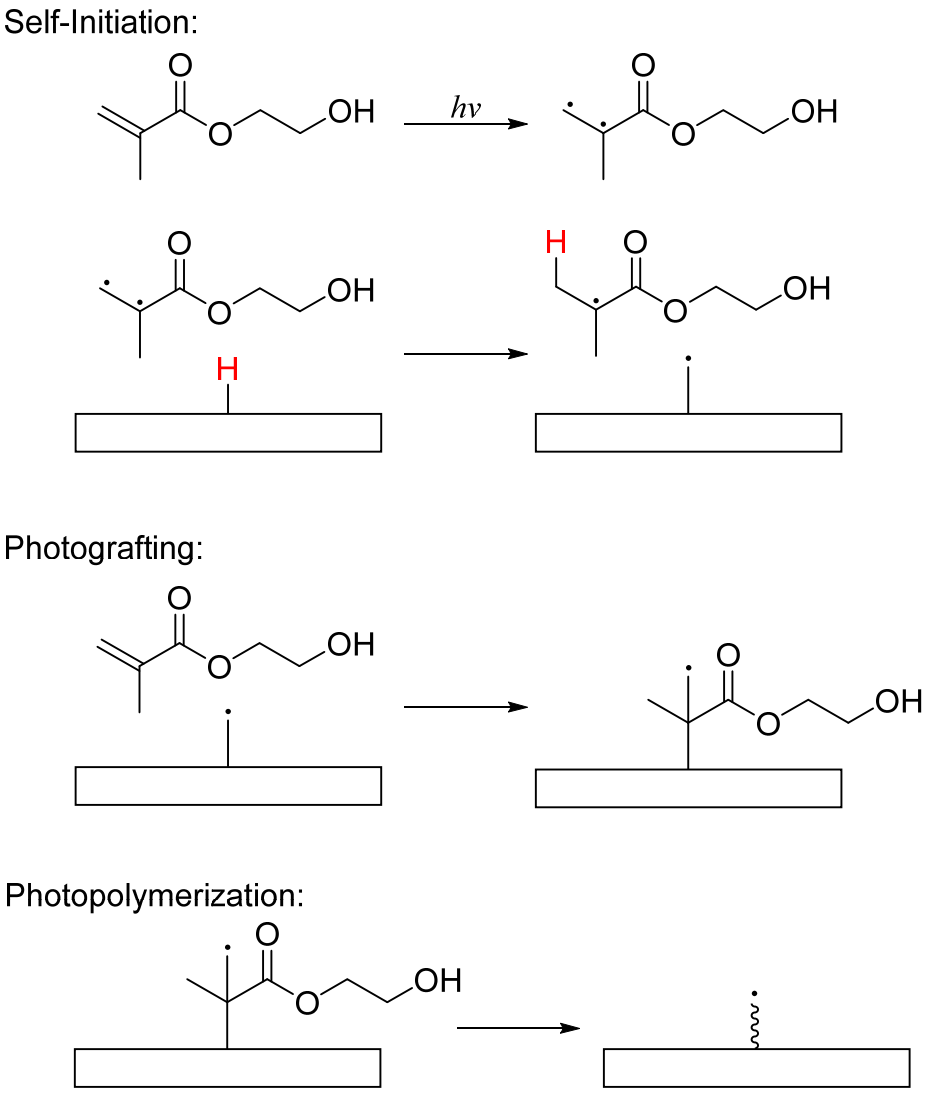

Scheme 4: *Reaction mechanism of self-initiated photografting and photopolymerization (SIPGP) by the example of HEMA with the abstracted hydrogen in red.*

This mechanism leads to a three dimensional network grafted from the surface of the substrate. At the start of the mechanism polymer strands or brushes are being formed. However, through for example chain transfer reactions these brushes get connected amongst each other and form a three dimensional network (Figure 7). Also not only

photografting from the surface, but also bulk polymerization inside the monomer solution can occur, because a hydrogen can not only be abstracted from the surface, but also for example from other monomers.

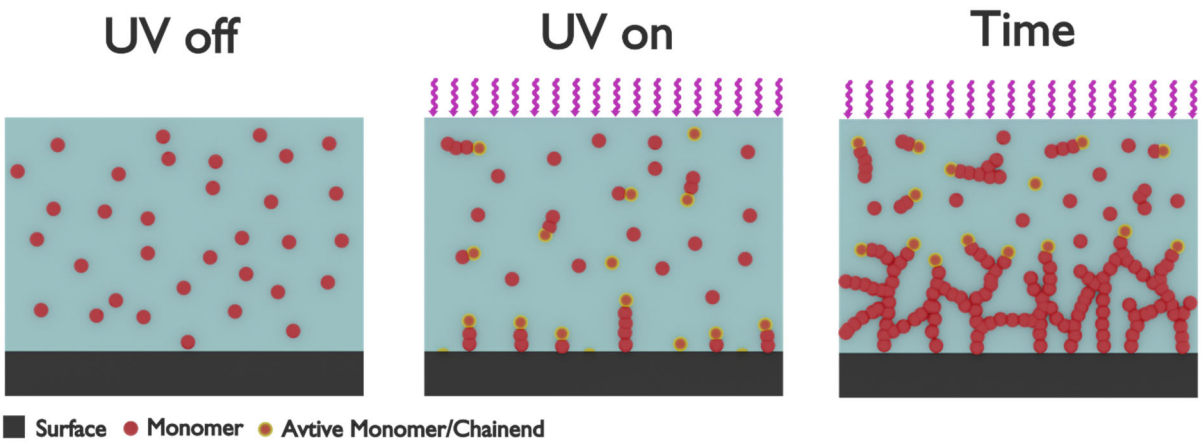

Figure 7: *Stages of SIPGP from start (left) to the initiation/photografting state (middle) to the late state (right). (Image taken from publication[194])*

2.2.3.3.1 Monomers for SIPGP

For the monomers, a sterically accessible double bond is necessary. Through irradiation by UV-light, a π-electron of the double bond gets excited from ground singlet state S_0 to excited singlet state S_1. Through inter system crossing (ISC) the excited electron can change its spin and reach the more stable triplet state T_3, which corresponds to a biradical (Figure 8). This triplet state has a bond energy of 471 kJ/mol for the T_3 state of acrylic acid.[195] The bond energy of acrylates and methacrylates for this state is “similar”, while the aliphatic/organic substituent does not play a role.[17,196] Though acrylates are the more reactive species compared to methacrylates for photopolymerization, methacrylates are more likely to self-initiate. The reason for that is that the methyl group of the methacrylates stabilizes the biradical more than the hydrogen of the acrylates. This way the lifetime of the biradical is longer and thus is more likely to react for example in abstracting a hydrogen from a surface.[196–199]

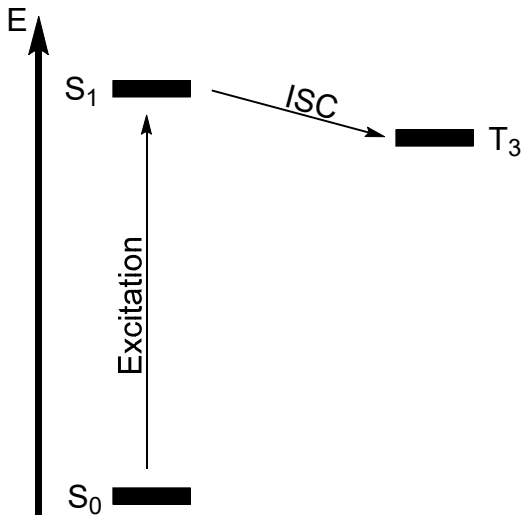

Figure 8: *Jabłonski-diagram for the excitation of methacrylates from the S_0 to the excited S_1 state and via intersystem crossing (ISC) to the biradical T_3 state.*

Most monomers used for SIPGP are acrylates or methacrylates. However, there are also acrylamides, vinyls and 2-isopropenyl-2-oxazoline. Table 1 provides an alphabetical list of all monomers used to this point in an alphabetical order.

Table 1: *Alphabetical list of monomers used in SIPGP.*

Monomer	Abbreviation	Lit.
2-(2-chloropropanoyloxy)ethyl acrylate	CPOEA	[200]
2-aminoethyl methacrylate hydrochloride	AEMA	[201]
2-carboxyethyl acrylate	CEA	[201]
2-hydroxyethyl acrylate	HEA	[197]
2-hydroxyethyl methacrylate	HEMA	[197]
2-isopropenyl-2-oxazoline	IPOx	[202]
2-methacryloyloxyethyl acetoacetate	MAOOEAA	[200]
[2-(methacryloyloxy)ethyl] dimethyl-(3-sulfopropyl) ammonium hydroxide	MEDSAH	[203]
[2-(methacryloyloxy)ethyl]trimethylammonium chloride	METAC	[203]
2-vinylpyridine	2VP	[204]
3-((2,6-dimethylpyridin-4-yl)oxy)propylmethacrylate	DMPPMA	[205]
3-sulfopropyl methacrylate	SPMA	[206]
4-(1H,1H,2H,2H-perfluorohexyl)oxymethylstyrene)	PPHMS	[207]
4-bromostyrene	SBr	[208]
4-vinyl pyridine	4VP	[209]
acrylic acid	AA	[210]
ethylene glycol dimethacrylate	EGDMA	[211]
ethylene glycol methyl ether methacrylate	EGMEMA	[212]
glycidyl acrylate	GA	[197]
methacrylic acid	MAA	[197]
N-(hydroxymethyl) acrylamide	HMAAm	[197]
N-hydroxysuccinimide methacrylate	NHSMA	[213]
N-isopropyl acrylamide	NIPAM	[207]
N,N-dimethylaminoethyl methacrylate	DMAEMA	[214]
N-vinyl imidazole	NVI	[215]
poly(ethylene glycol) methacrylate	PEGMA	[197]
sodium 4-styrenesulfonate	NaSS	[216]
styrene	St	[17]
tert-butyl methacrylate	*t*BMA	[202]

The second important part of SIPGP besides the monomers is the surface, which is to be grafted. The next chapter will describe their requirements in more detail.

2.2.3.3.2 Surfaces for SIPGP

For the initiation process of SIPGP the prior described biradical must abstract a hydrogen from the surface. So the requirement for the surface is a sterically accessible hydrogen with a bond energy below 471 kJ/mol. This includes C-H (416 kJ/mol), N-H (319 kJ/mol), O-H (462 kJ/mol) and Si-H (323 kJ/mol), which are the hydrogen bonds that were used for SIPGP so far.[210,214,217–219] If a surface does not fulfill the requirements for SIPGP, there are methods, which can be used to achieve that. One is a plasma treatment to generate O-H or Si-H groups on surfaces such as silicon wafers. Plasma treatment can also be used to generate C-H groups on surfaces such as graphene or nanocrystalline diamond.[215,220–222] Another way are self-assembled monolayers (SAMs). With this method molecules applicable as a SIPGP surface form non covalently attached monolayers on top of surfaces such as gold or glass.[223–225] Table 2 provides an alphabetical list of all surfaces used in SIPGP so far. When SAMs are used, the SAM-forming monomer is enlisted.

Table 2: *Alphabetical list of surfaces used in SIPGP. SAM = self-assembled monolayer.*

Surface	Abbreviation	Lit.
1,2-dimethyl-3-(3-(trimethoxysilyl)propyl)-1H-imidazol-3-ium iodide	MMSPII	215
1H,1H,2H,2H-perfluorooctyltriethoxysilane SAM	PF-SAM	225
3-aminopropyltrimethoxysilane	APTMS	205
3-(trimethoxysilyl) propylamine SAM	TMSPA	226
(3-aminopropyl)triethoxysilane	APTES	227
4’-amino-1,1’-biphenyl-4-thiol SAM	cABT	228
α, ω -aminopropyltrimethoxysilane SAM		221
ω-functionalized biphenylthiol SAMs		229
Aminophenyl modified Au, ITO and SS surfaces	AP	218
Benzoylphenyl modified Gold (Au), Indium tin oxide (ITO), stainless steel(SS) surfaces	BP	218
Biphenyl thiol SAM	cBT	228
Biphenyl SAM		230
Borosilicate glass (plasma treated)		231
Carbon nanotubes	CNT	232
Cellulose nanocrystals	CNC	213
Chitosan		233
Dodecylphenyl modified Au, ITO and SS surfaces	DDP	218

Glassy carbon	GC	[202]
Graphene oxide	GO	[219]
Graphene (Plasma treatment)		[222]
Green tea polyphenols	TP	[203]
High density polyethylene	HDPE	[197]
Hydrogen terminated Silicon Substrates		[234]
Hydroxylated 6H-SiC SAMs	6H-SiC	[214]
Isotactic polypropylene	iPP	[235]
Low density polyethylene	LDPE	[210]
Mercaptohexadecanoic acid SAM	MHA	[223]
MXene		[236]
Nanocrystalline diamond (plasma modified)	NCD	[220]
Nano indium tin oxide	nanoITO	[237]
PEG-thiol HS(CH2)11CONH(C2H4O)11CH3 SAMs	mPEG	[201]
Plasma polymerized allylamine coatings on Si wafers	SiAlaPP	[200]
Poly(acrylic acid)	PAA	[238]
Polydopamine	PDA	[239]
Poly(ethylene-alt-tetrafluoroethylene)	ETFE	[240]
Polyethylenimine	PEI	[241]
Poly(ethylene terephthalate)	PET	[242]
Poly(styrene)	PS	[212]
Polyurethane	PU	[243]
Poly(vinylidene fluoride)	PVDF	[244]
Polyvinylpyridine-grafted Gallium phosphate$_{(100)}$	GaP	[245]
Pyrenes (Py-CH_2NH_2)		[246]
Single layer hexagonal boron nitride	SL-hBN	[247]
Ultrananocrystalline diamond (plasma modified)	UNCD	[248]

Utilizing these surfaces and monomers, different types of applications are being proposed in literature. The following chapter will describe these applications.

2.2.3.3.3 Applications for SIPGP

In 2001 Deng, Yang and Rånby first described the mechanism of SIPGP. They polymerized styrene by placing a styrene solution between two films of low density polyethylene (LDPE) and were able to graft styrene from the LDPE films this way.[17] Steenackers *et al.* were the first to propose SIPGP to be used for biomedical applications after they were able to graft polystyrene (PS) from oxidized ultrananocrystalline diamond (UNCD).[248] In 2009 Zhang *et al.* described the formation of Bottle-Brush Brushes (BBB). They used SIPGP to graft poly(2-isopropenyl-2-oxazoline (PIPOx) from glassy carbon (GC). In a subsequent step PIPOx was polymerized via living cationic ring-opening polymerization (LCROP). These BBBs were then proposed to function as a "*soft interlayer between a conductive surface and biological systems*".[202] BBBs that were grafted from cellulose nanocrystals (CNC) in 2017 were even proposed to function as carriers for drugs and genes for photothermal cancer therapy.[249]

Also gradients of graft polymer can be fabricated via SIPGP, as Steenackers *et al.* reported in 2009. In order to form the gradient, the polymerization was induced by an electron beam with a decreasing irradiation dose.[229] Gradients could also be fabricated by using a shutter that was slowly removed during the reaction. Ekblad *et al.* used this as a possible way to adjust protein adsorption and proposed this for anti-biofouling or biosensing applications.[201] Also for biosensing, Hess et al. grafted poly(N,N-dimethylaminoethyl methacrylate) (PDMEMA) from graphene transistors. The tertiary amine containing side groups were then linked to enzymes and transducing pH sensitive groups, which enabled them to detect the neurotransmitter acetycholine.[250]

In the same year Rahimpour *et al.* grafted HEMA and AA from a PVDF membrane. This membrane was coated in order to improve its antifouling properties. In addition, the protein rejection of the membrane could be improved.[244] In 2010 Gupta *et al.* grafted poly(2-dimethylamino)ethyl methacrylate) brushes from GC and then immobilized silver nanoparticles into the brush layer. This way they were able to fabricate a sensor platform for the detection of organic molecules by surface enhanced Raman spectroscopy (SERS).[251] Another report to use SIPGP in a biosensing application was done by Gölzhäuser *et al.* They grafted BBBs from nanocrystalline diamond containing hole conducting carbazole moieties and proposed their product to be a possible application for biocompatible sensor systems.[220] Not only BBBs can be fabricated, but also

polymer carpets. Amin *et al.* showed this by polymerizing styrene from a SAM, which is of a thickness of ~1 nm. By grafting brushes, which stabilized the nanosheet, they were able to form the first free standing nanosheet. One year later Amin *et al.* were also able to fabricate patterned polymer carpets by patterning the nanosheets before performing SIPGP.[228] Also on hydrogenated graphene Seifert at al. were able to fabricate polymer carpets via SIPGP.[222]

The first to test SIPGP grafted samples in a biological environment were Faxälv *et al.* They grafted PEGMA, PHEMA and P(PEGMA-co-HEMA) from Polystyrene (PS) surfaces and tested their blood compatibility. Specifically they tested protein adsorption, platelet adhesion and surface-induced coagulation. They found that all of their tested surfaces performed better than the plasma-treated or unmodified PS.[212] Zhang *et al.* then also reported in 2012 that their BBBs can be fabricated to have a non-fouling behaviour and a good cell adhesion. They also were the first to propose SIPGP grafted surfaces to be used as a coating for implants.[221] In the same year, Zhang *et al.* also reported, that hydrogen terminated silicon substrates can be grafted via SIPGP. By doing so they provide a new method of forming a Si-C bond that can help modifying silicon substrates in the future.[234]

In 2013 Krawicz *et al.* used SIPGP as a “link” method between p-type Gallium phosphate and a cobalt containing hydrogen evolution catalyst. This way SIPGP surfaces were used as a part of a visible-light-absorbing semiconductor.[245] This application was then further developed by Wadsworth et al.[237] Hou *et al.* were the first to use SIPGP for the surface modification of CNCs. These composites could then be used as a heterogeneous visible-light photocatalyst.[213]

Gu *et al.* reported in 2014, that SIPGP surfaces can also be utilized for oil/water separation membranes.[232] To do so they first grafted PS from a nanosheet of carbon nanotubes (CNTs), lifted it from its glass substrate, turned it upside down and grafted PDMAEMA from the other side of the CNTs. This way they fabricated a Janus sheet with hydrophobic PS on the one and hydrophilic PDMAEMA on the other side.[252] Besides that a variety of nanosheets were directly or indirectly (by the support of SAMs or modifications) coated using SIPGP, e.g. MXenes, Fe_3O_4, Ti_4AlN_3, MoS_2 or CNTs.[208,236,253–259]

In 2015, Hou *et al.* were the first to utilize SIPGP to endow the possibility of different functionalities in the surface of bio-inspired polydopamine (PDA).[239] Hafner *et al.* then further developed these grafts to also from Janus nanosheets of PDA grafted with PS and PDMAEMA.[206] Zheng *et al.* reported in 2016 the use of PDMAEMA grafted SiO_2 particles as an ingredient for a self-healing hydrogel. To achieve that, these grafted particles were dispersed in an aqueous acrylic acid (AA) solution, which was then bulk polymerized. The electrostatic interactions between the PDMAEMA side chains and the PAA side chains then lead to the self-healing properties of this hydrogel.[260] PDMAEMA was also used by Zhai *et al.* to be grafted from conical micro channels within a PET sheet for a dual responsive ion gate.[242]

In the same year, Styan *et al.* used SIPGP to graft poly(2-(2-chloropropanoyloxy)ethyl acrylate) (PCPOEA) from plasma polymerized allylamine coatings on silicon wafers. The sidechains of PCPOEA were then used as an initiator for an SI-ATRP grafting. This way they managed to use SIPGP to tune the initiator density for SI-ATRP.[200]

In 2017 Xiao *et al.* reported the grafting of patterned PDMAEMA from graphene oxide (GO).[261] They found that the grafting did not diminish the intrinsic chemical properties of the grafted GO.[262] Xing *et al.* then grafted poly(4-vinylpyidine) (P4VP) from GO in order to use the grafts as a reaction chamber for the shape controlled synthesis of Au-polypyrrole composites.[263] In a similar approach Wang *et al.* used poly(2-vinylpyridine) (P2VP) grafted from GO for the fabrication different shaped gold nanoparticles. The particles, as well as the previously mentioned composites can form inside the polymer brushes and then can be extracted.[204,264]

In 2020 Chen at al. fabricated gold nanoparticle attached PDMAEMA grafted Fe_3O_4 nanoparticles. This composite is able to function as a catalyst for the reduction of 4-nitrophenol. In addition, this catalytic effect can be altered due to the thermo responsiveness of PDMAEMA.[265] In the same year Cėpla *et al.* reported that a terpolymer of HEMA, PEGMA and MAA can be directly grafted from a PEG hydrogel. They showed the anti-fouling properties of this polymer graft and proposed this material a bioanalytical device such as cell arrays or tissue-on-a-chip systems.[231]

Although some SIPGP grafted surfaces have shown to be suitable for biomedical applications and a usage as a coating for implants was proposed, no steps were taken

so far to tackle that issue. In order to do so, the following work presents a further development of SIPGP.

3 Motivation

Self-initiated photografting and photopolymerization (SIPGP) is a grafting mechanism, which got only limited attention since its first description in 2001.[17] Despite SIPGP coatings being proposed to be used as implant coatings, no significant steps were specifically made in this direction.[206,221,266,267]

SIPGP, since it is a free radical polymerization, is less controllable than other *grafting from* mechanisms such as ATRP or RAFT. To face that challenge, in this work a new method of performing SIPGP will be developed: The dynamic SIPGP. By applying a constant monomer flow to the reaction the controllability of SIPGP will be increased, and with that the formation of undesirable bulk polymerization decreased. To achieve that, a new reactor will be designed to perform the first experiments of dynamic SIPGP.

The substrates used to develop this dynamic setup will be films of the terpolymer P(VDF-TrFE-CTFE), which is a piezoelectric polymer. These films will then be coated with a P(HEMA-co-MEDSAH) coating to discover the influence of a constant monomer flow on the process of SIPGP with regard to parameters such as bulk polymer formation, heat development, surface contact angle, and homogeneity of the formed coating. The chemical structures of these polymers are shown in Figure 9.

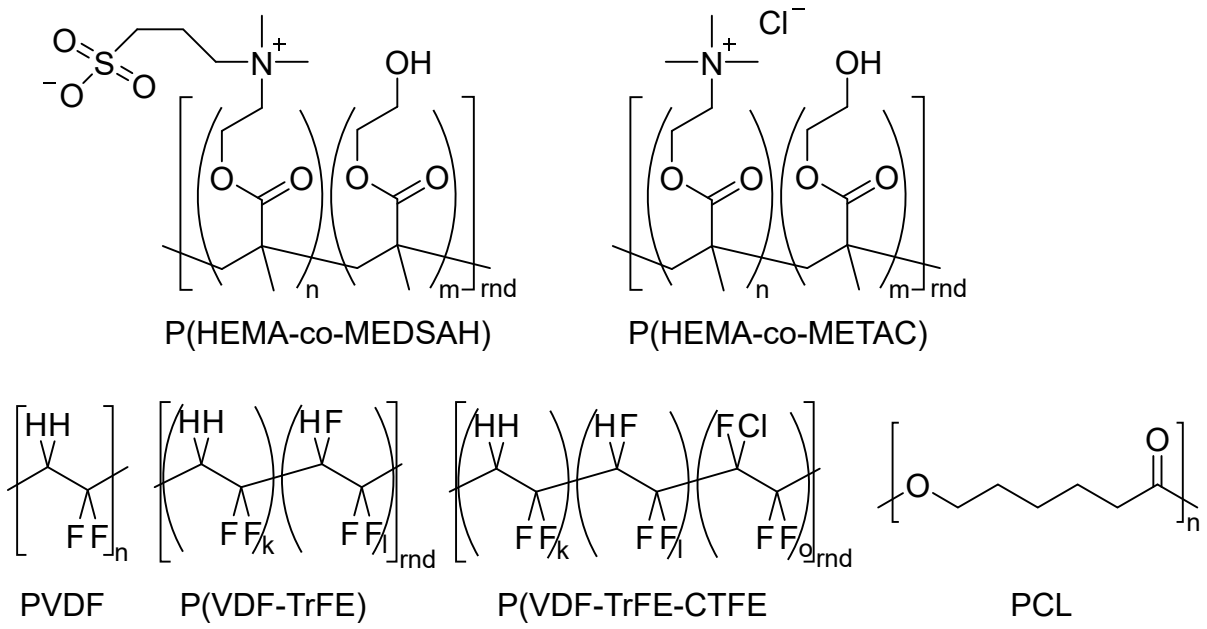

Figure 9: *Chemical structure of polymers used in this work with the coating polymers in the top row and the surface polymers in the bottom row.*

Furthermore, SIPGP will be performed on MEW printed scaffolds of PVDF, P(VDF-TrFE) and PCL. With coating these scaffolds also another coating will be introduced. This P(HEMA-co-METAC) coating will be designed for possible applications as implant coatings. Therefore not only the SIPGP performance on MEW scaffolds will be examined, but also cytotoxicity and cell adhesion will be tested on the two mentioned coatings. To further improve cytocompatibility and cell adhesion, a subsequent SIPGP step will be performed to covalently attach RGD-sequences to the previously formed hydrogels.

4 Results and Discussion

4.1 Development of the reactor

Because SIPGP is a technique that is performed on the surface of a substrate, it requires an uncommon vessel. This vessel must also provide a controlled environment. In this case, also a constant flow of a solution inside the vessel during the reaction must be possible. The following chapters describe the requirements of such a vessel, which will be called a reactor in the following, and how such a reactor can be designed.

4.1.1 First designs and rapid prototyping

The initial design was done using the 3D graphics software *blender* (Figure 10). The reactor was designed for the coating of samples with a surface between 100 mm² and 200 mm². Therefore, the inner flow chamber had an area of 10 mm x 40 mm. the sample was supposed to not lie directly on the floor, so the platform for the sample to be put on was elevated 1 mm (dimensions in more detail in chapter 7.3.1).

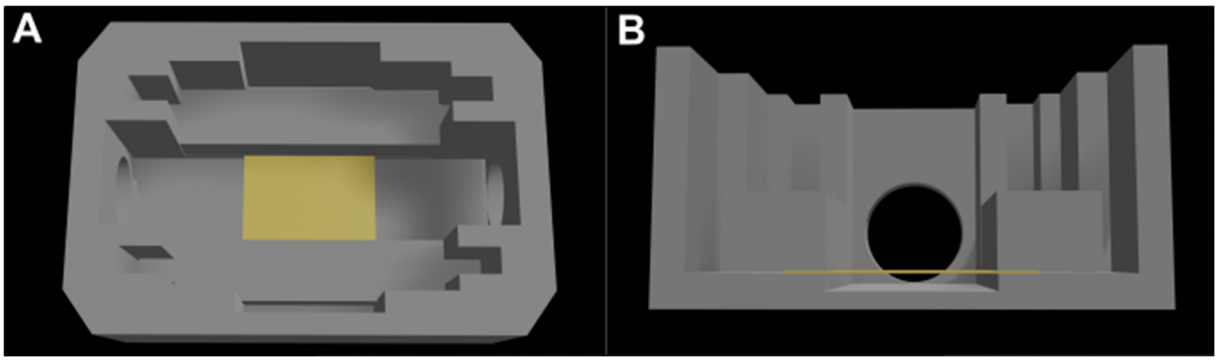

Figure 10: *Design of a 3D printed reactor including walls for fixation of the (in this image yellow) sample, which was used on a regular basis in top view (A) and a cross section (B).*

The reactor has two opposing connection points for tubes in order to apply a constant flow of monomer solution to the reactor (the reason for that will be explained in greater detail in chapter 4.3). The diameter of these holes is about 6 mm and must be adjusted to the used tubes. When a flow is applied, the sample must be kept in place to prevent

a movement of the sample during the reaction. The same is true for a static use of the reactor but to a lesser extent. For this reason, the two removable walls were introduced. They are placed on top of the sample and must be fixed inside the reactor. Therefore protrusions at the right and left end of the walls are needed that fit exactly into the indentations in the reactor. The additional notch in the reactor located at the “outside” of the walls has no relevance for the reaction but is very useful for an easier removal of walls using a tweezer. After the sample and the walls are placed, a silica glass can be put on the top of the reactor. Now there is a closed system inside the reactor, so the atmosphere can be controlled. For this purpose, there are two small holes with a diameter of 1 mm at the top of two opposing corners. The wholes are big enough for a needle to fit in. One of the holes can be used as an argon inlet, while the other one is the outlet in order to prevent overpressure inside the reactor.

After the first designing steps rapid prototyping was used to improve the design of the reactor and to develop different reactors for different purposes. The DLP printer *Autodesk Ember* was used to do so. The two resins used were *clear* and *black* (Figure ***11*** A). More details about the printing and the resins can be found in chapter 7.3.1. This type of reactors will henceforth be referred to as “3D printed reactors”. The difference in colour of the walls and the reactor printed with *clear* resin (Figure 11 A) already show a disadvantage of the printed reactors. The colour change results from the irradiation during coating procedure, which means, that there are aging processes occurring (Figure 11 C). However, not only a colour change could be observed, the reactor also got more and more brittle with a higher number of reaction procedures. For this reason, the reactors could only be used for a maximum of about 20 coating procedures. When used too often the reactors even cracked during the coating process. However, the major advantage of the printed reactors is a fast production of new designs. If a reactor is not printed with the two holes as an in- and outlet for dynamic SIPGP (Figure 11 A), but without them (Figure 11 B), the reactor can be used for static SIPGP. This type of reactor was used to examine different reactor heights (Figure 11 D). It sets the minimum distance possible between the sample and the light source. But if the reactors height is too low, the solution inside will interact with the glass due to a minimization of the surface tension.

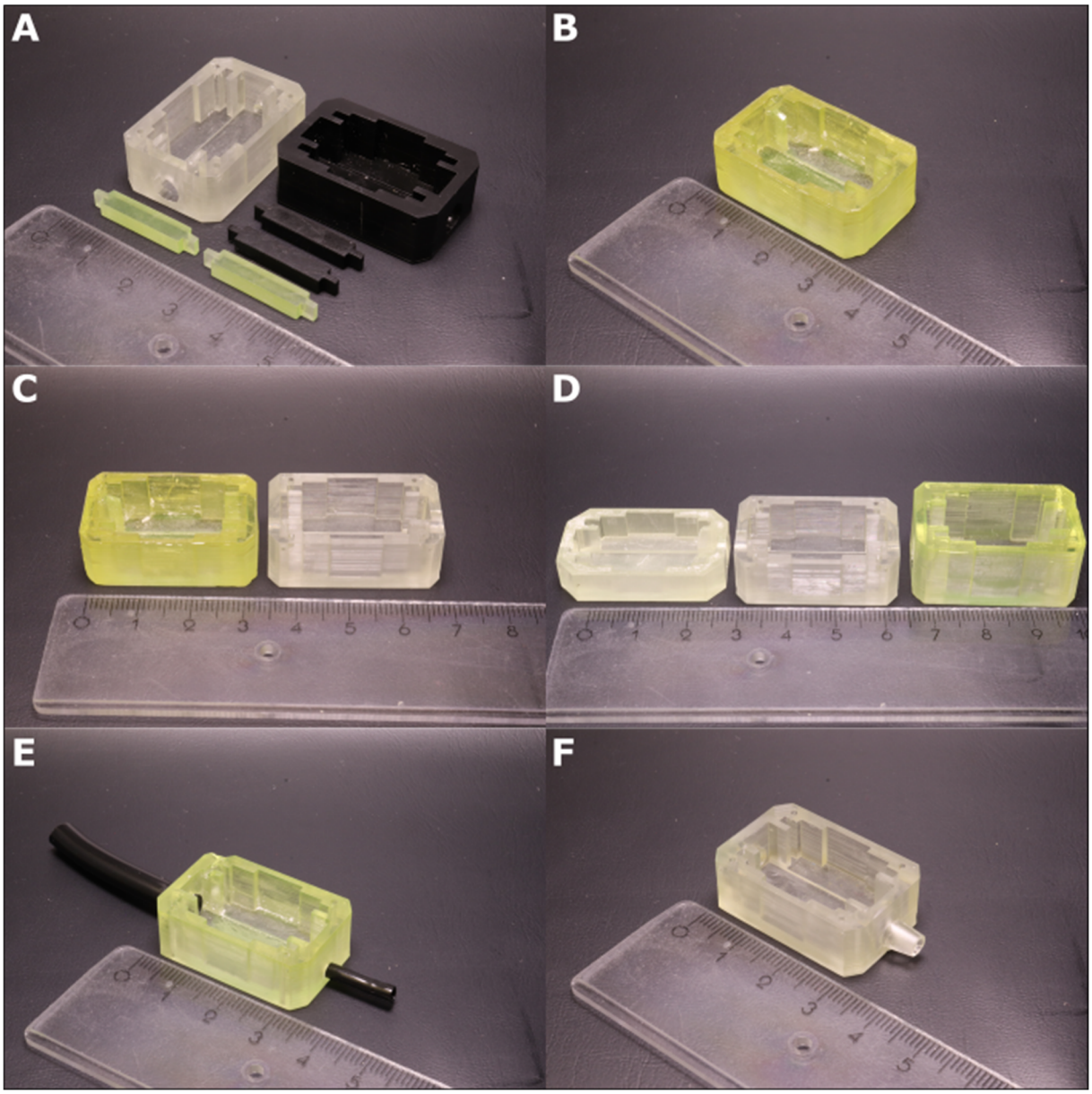

Figure 11: *Most used version of the 3D printed reactor for dynamic SIPGP out of clear and black resin (A). Reactor without an in- and outlet so it can be used for static SIPGP (B). Unused and regularly used reactor (C). Comparison of three different reactor heights (D). Example of a reactor that is connected to one small and one big tube (E). Version of the reactor where the tube is not inserted in the reactor, but vice versa (F).*

The adjustment of the tubes to the reactor (or more vice versa) is the most difficult part when it comes to designing the reactor. The reason for that is the discrepancy between the designed model on the computer and the printed reactor. It might be small, but the smallest discrepancies make a huge difference when it comes to a sealed system. So a flexible tube is needed and a hole that is a little smaller than the diameter of the tube. The tubes used here were polyurethane tubes with a diameter of 6 mm (big one) or 3 mm (small one) (Figure 11 E). In this case a smaller inlet tube was chosen to reduce

the amount of solution that is needed to initially fill the reactor. Another way of connecting the tube to the reactor is to print protrusions over which the tube can be pulled, (Figure 11 F). However, this has two major disadvantages. One is that this is more difficult to print, because you need supportive structures that can cause some irregularities on the surface after the removal. The other one is that the tubes can slip off during the reaction.

One big disadvantage of the 3D printed reactors, that was not mentioned yet, is the fact that they consist of an organic polymer. As the mechanism of SIPGP in chapter 2.2.3.3 shows, the printed reactors themselves will react with the monomers according to the SIPGP mechanism. This is the second reason why these reactors are not suitable for a long term use when it comes to SIPGP. However, they are perfect to find the right design for a reactor and to try many different designs practically. So the data and experience gained from these reactors were used to get the final reactor design that is described in the following chapter.

4.1.2 Advanced design

The main difference between the now described reactor and the 3D printed ones is the material. This one was milled from stainless steel by Harald Hümpfer at the *Department for Functional Materials in Medicine and Dentistry* in Würzburg, Germany. This reactor will henceforth be referred to as “metal reactor”. This reactor consists of a reactor body, two walls with screws, two tube connections and two rubber plugs (Figure 12 A). Having a reactor made out of metal solves the two main problems that the 3D printed reactors had: The interaction of the reactor with the monomers, because SIPGP does not occur on metal surfaces. And the interaction of the reactor with the UV-light, because stainless steel is not affected by UV-light.

The reaction chamber of the metal reactor has an area of 10 mm x 40 mm. The corners however, are not pointy, but radiused, to provide a more homogeneous flow of the monomer solution inside the reactor without creating irregularities such as eddies. The height of the reaction chamber is 15 mm. The height of the walls is 10 mm, resulting in a 4 mm gap between the walls and the top of the reactor (dimensions in more detail in

chapter 7.3.1). This gap is important, because with higher walls there is a higher margin of the monomer solution level that can be used. However, the thickness of the sample has to be taken into account and the walls must never exceed the height of the reactor. If they do, the reactor cannot be sealed with the glass slide. The reactor can be properly sealed by this slide with the help an O-ring. In contrast to the 3D printed reactors, the walls also have two additional features. One are the screws on top of the walls. They are just for an easier removal of the walls, because even with a tweezer they are sometimes hard to remove. However, the screws can be put in and help to easily remove them, which improves the handling of the reactor significantly. The other new feature are the indentations at the bottom of the walls. To understand why they exist, the following is important to know: There is some space behind the walls, (as can be seen in the top view of the reactor in Figure 12 D) and if very thin samples and aqueous solutions are used (as in this work) the space behind the walls is not filled with solution, due to the surface tension of water. However, many times during the reaction (especially when the solutions gets warmer), the solution slips through and the space behind the walls gets filled. The problem about that is that the level of the solution rapidly drops. This changes the conditions of the reaction and sometimes even exposes the sample from the solution. Due to the indentations at the bottom of the walls however, the space behind the walls is filled with solution from the start, so this effect does not cause problems.

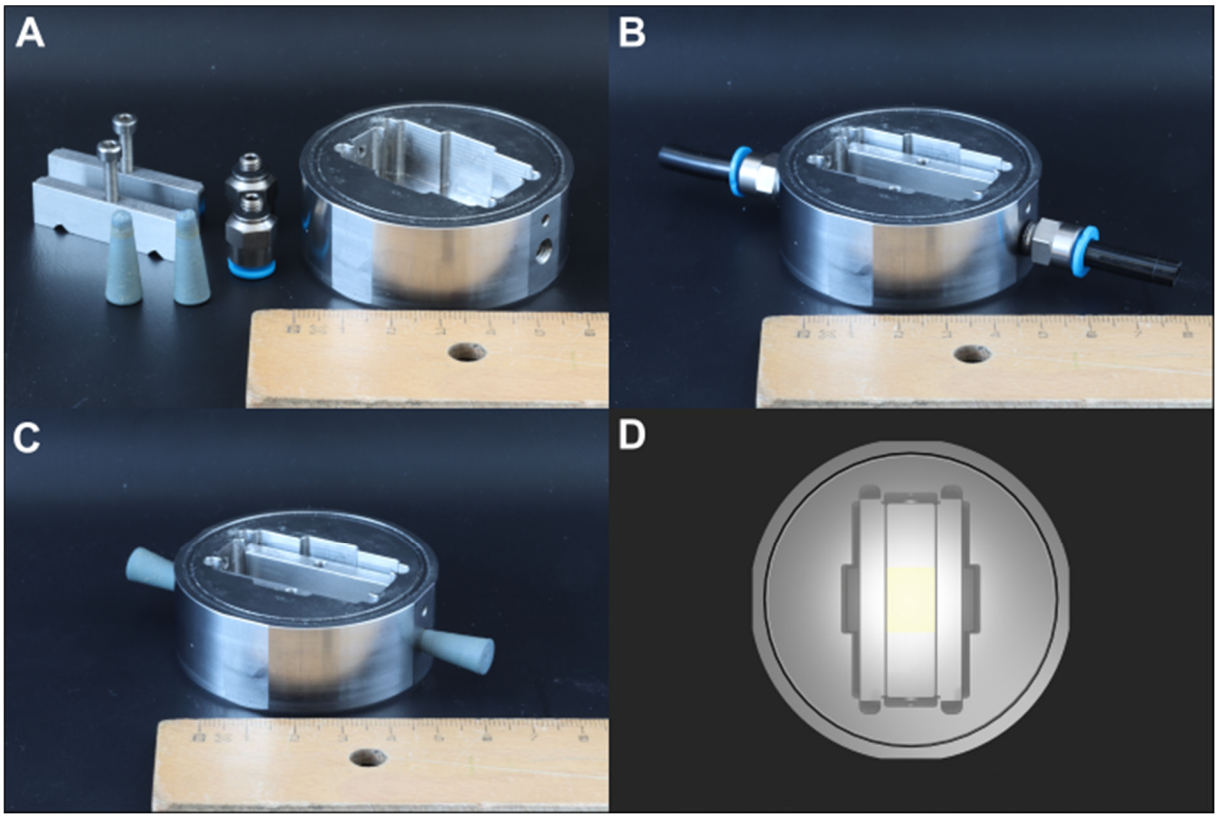

Figure 12: *Disassembled metal reactor including the following parts from left to right: walls with screws, rubber plugs, tube connections and the reactor body (A). Assembled metal reactor for the use of dynamic SIPGP (B). Assembled reactor for the use of static SIPGP (C). Top view of a 3D modelled version of the reactor including a sample (yellow) (D).*

The next important thing to have is a sealed tube connection for the dynamic SIPGP. For this reason, the reactor body has an inside thread at the inlet and outlet. This way a union connector could be screwed in the reactor body to get a sealed connection to the tubes (Figure 12 B). Another advantage of the inside thread is the fact that also the rubber plugs could be screwed into the in- and outlet and seal the reactor to use it for static SIPGP, too (Figure 12 C). The two holes for the argon are above the in- and outlet of the monomer solution and have a diameter of 2 mm. The spots for these were chosen, because the distance between inlet and outlet needed to be as long as possible to provide an argon atmosphere.

This reactor was designed to perform static and dynamic SIPGP. In order to characterize the capability of the reactor to perform dynamic SIPGP, the flow of the monomer solution was calculated.

4.1.3 COMSOL calculations

The flow calculations for the reactor were performed with the program *COMSOL multiphysics*®. The model used for these calculations was done with the 3D-modeling software *blender* (Figure 13). The model represents the inner part of the reactor with the walls as borders at the sides. A film as a substrate was also implemented to be able to have a look at the flow velocity on top of the sample during the reaction.

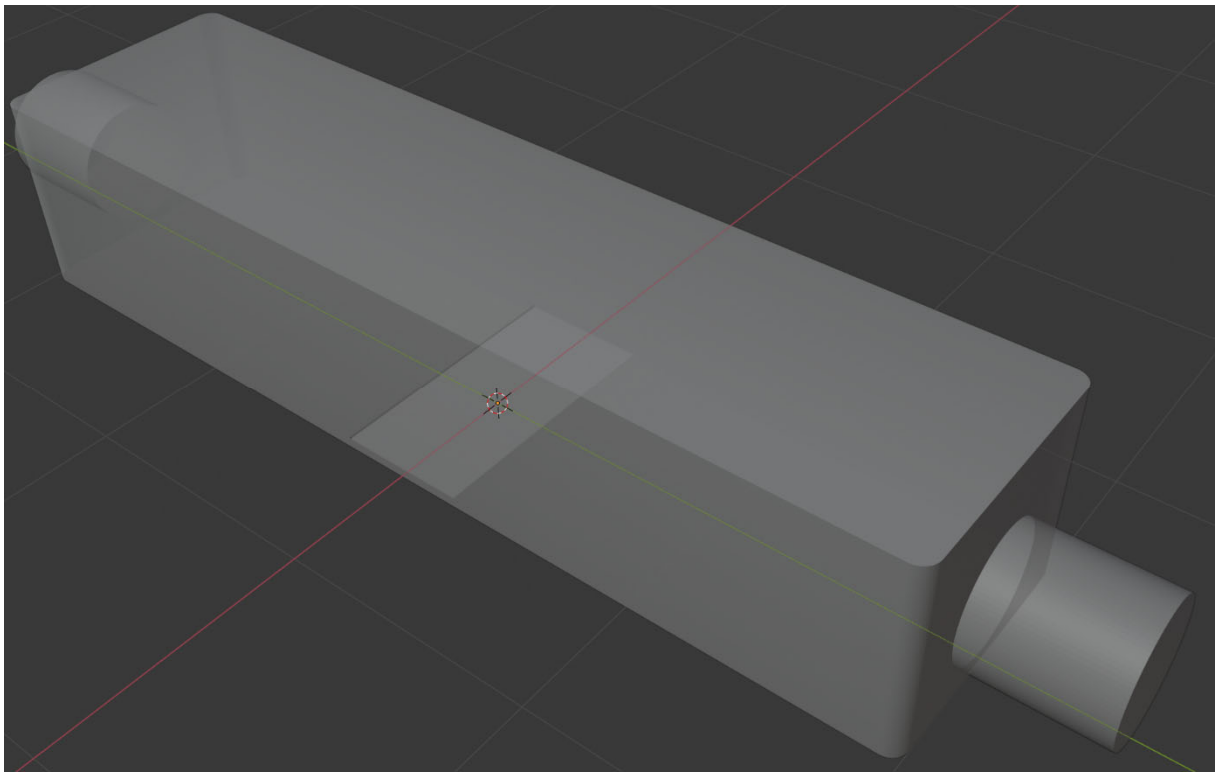

Figure 13: *Model in blender used for the COMSOL calculations. It consists of inner part of the reactor that is important for the flow of the monomer solution and of the sample inside the reactor. For the sample, the most used size of 10 mm x 5 mm was used.*

The monomer solution that was used for dynamic SIPGP was the aqueous HEMA/MEDSAH solution described in chapter 7.3.3. To properly calculate the flow of the used solution it needed to be characterized in terms of density and viscosity (Figure ***14***). The range of the measurement between 20 °C and 50 °C was chosen, because the temperature during the reaction lies within these values (More about the temperature during the reaction in chapter 4.3.3).

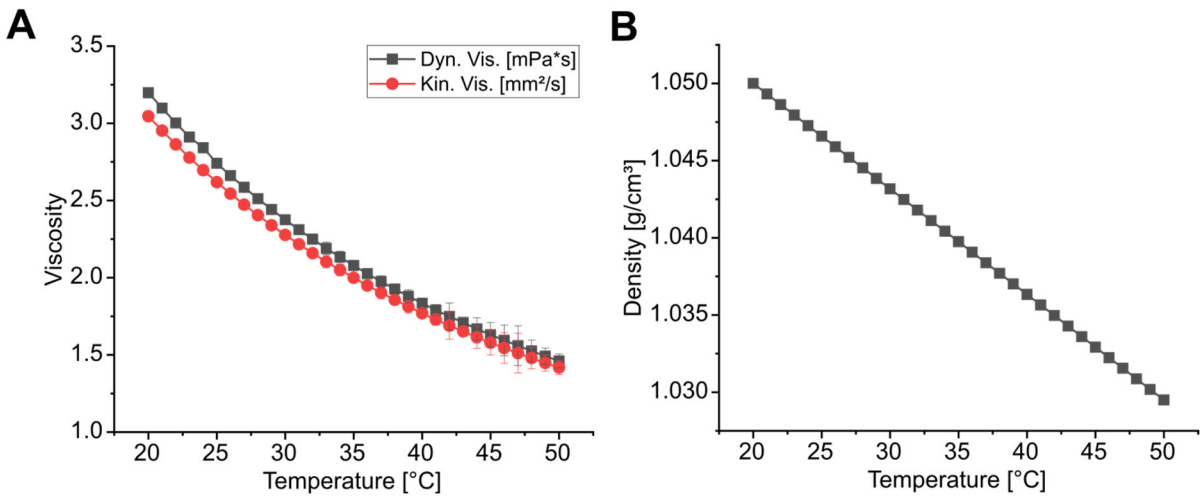

Figure 14: *Density (A) and Viscosity (B) of the HEMA/MEDSAH solution between 20 °C and 50 °C.*

For the calculations the module *lamellar flow* was used. The range of the flow to look at was chosen from 1 ml/min to 5 ml/min (Figure 15 A-E). The plane that shows the flow velocity by colour was chosen slightly above the sample, because this is the important region for the reaction. The flow velocity right above the sample is lower than that of the solution before and after the sample on the same plane. That is because the sample itself is slowing the monomer solution down and the program is considering the flow on every border as zero. The most important finding of the calculations however, is that there are no eddies forming inside the reactor that can disturb the homogeneous flow of the solution.

Another important factor is the width. To elucidate this, a cross section of all five calculated flow rates at the red line in Figure 15 A-E was calculated (Figure 15 F). This shows that the difference in flow velocity between the inner part of the sample and the outer parts of the sample increases with higher flow rates. Having a wider reaction chamber would reduce this problem, however, as the greater length does, would also lead to a higher amount of monomer solution needed per reaction. Using a lower flowrate is also a way to reduce the relevance of this problem. A comparison between the calculations and measurements on coated samples can be found in chapter 4.3.2.

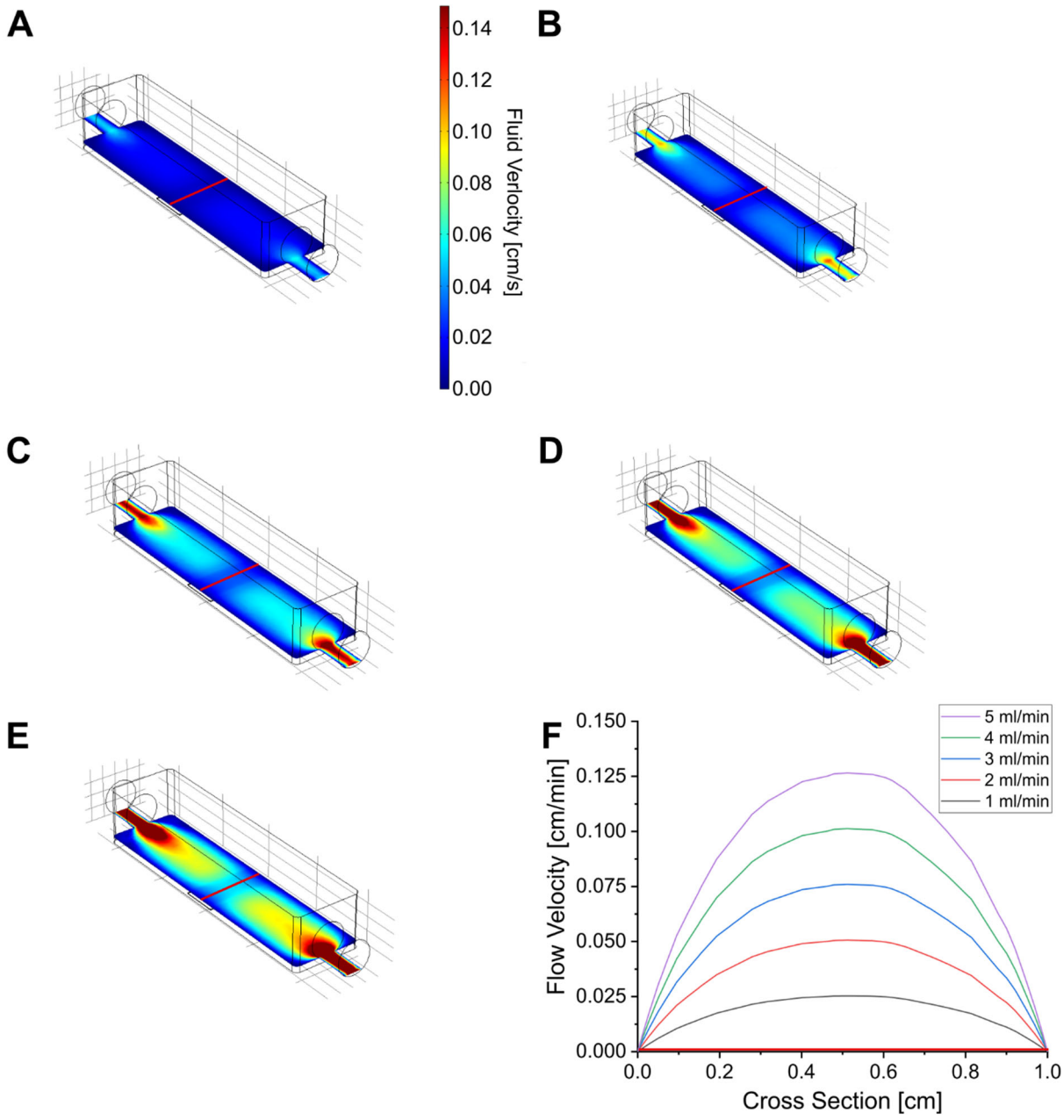

Figure 15: *Calculations of the laminar flow done with the multiphysics program COMSOL from 1 ml/min - 5 ml/min (A-E). The model represents the inner part of the reactor, where the flow of the solution is actually happening including a sample. The red line in all of the models represents the location of the cross section (F).*

The actual coatings inside these reactors were mainly performed on films of P(VDF-TrFE-CTFE). The following chapters describe the performance of static and dynamic SIPGP beginning with the finding of suitable settings of a variety of different parameters for static SIPGP referred to the described reactors.

4.1.4 Conclusion

A new custom designed reactor was developed, that is capable of performing static, as well as dynamic SIPGP. Inside the reactor an inert gas atmosphere can be applied for a better reproducibility of the experiments. To find the best design for such a reactor, rapid prototyping was utilized.

To have a better insight of the solution flow inside the reactor during the reaction, also theoretical calculations of those were performed.

4.2 Static SIPGP on Films of P(VDF-TrFE-CTFE)

4.2.1 P(HEMA-co-MEDSAH)

As described previously in chapter 2.2.2.1, HEMA is a good choice to function as a base monomer for materials that are supposed to be used in biomedical applications. As a comonomer [2-(methacryloyloxy)ethyl]dimethyl-(3-sulfoproply)ammonium hydroxide, (MEDSAH), is used. This is a zwitterionic methacrylate that is non cytotoxic and can function as an anti-fouling material.[110,111,152] These two monomers, as being methacrylates, can be utilized to form P(HEMA-co-MEDSAH) through SIPGP. The reactive group of both monomers is the same, a methacrylate. This means, that the reactivity of the monomers, as well as the sterical properties are similar. For this ratio of monomers inside the reaction mixture and in the polymer is likely to be similar, too. This copolymerization behaviour is for example reported for the copolymerization of HEMA and oligoethylene glycol methacrylates (OEGMA), for HEMA and methylmethacrylate (MMA) and HEMA and 2-ethoxyethyl methacrylate (EEMA).[268–270]

To find an appropriate monomer solution to perform the SIPGP experiments the data of two bachelor theses were used. Miriam Komma examined the optimal ratio of water and methacrylate for an aqueous HEMA solution to be used for SIPGP in her bachelor thesis.[194,271] It was found that the ratio leading to the fastest reaction was HEMA:water 45:55 (wt%).[271] This ratio is used for every monomer solution in this work. In this work always comonomer solutions are used, but the ratio mentioned between the two monomers is always concerning the 45 wt% in water. Simon Ziegler was then examining the comonomer solution of HEMA and MEDSAH. He found that a ratio of HEMA:MEDSAH 88:12 wt% led to the fastest reaction.[272] The exact composition of this solution is described in chapter 7.3.3.

The HEMA/MEDSAH monomer solutions form a hydrogel when polymerized in bulk without using an initiator, but only using UV light (Figure 16). The swelling degree of different ratios of the P(HEMA-co-MEDSAH) bulk polymer was examined, while the swelling degree (S_D) was calculated from the weight of the dried polymer (W_d) and the weight of the swollen polymer (W_s) as follows:

$$S_D = \frac{W_s - W_d}{W_d} * 100$$

To form these bulk polymers, they were put into a silicone form and were irradiated with a 25 W UV-lamp for 48 h with a distance of 1 cm between the lamp and the monomer solution (d_{ls}). The ratios with MEDSAH higher than 50 wt% were produced too, but after 98 h in water they lost their shape to an extend that made it impossible to measure the swelling degree. Details of producing these samples can be found in chapter 7.3.4.

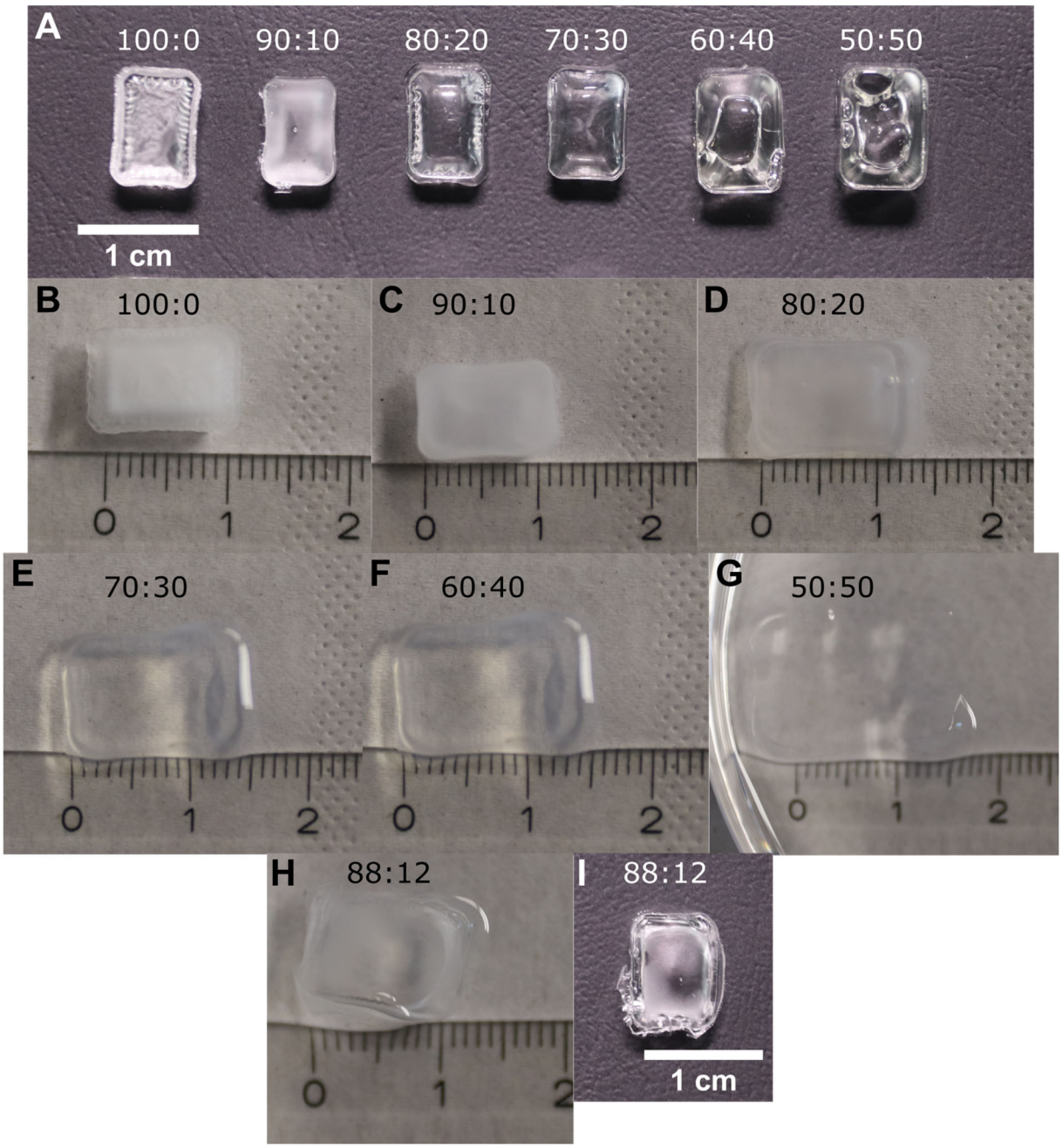

Figure 16: *Bulk polymers of P(HEMA-co-MEDSAH) with different monomer Ratios (the ratios in shown in the images are the wt% ratios of HEMA:MEDSAH. Images of the dried bulk polymers (A, I) and bulk polymers after 98 h immersed in water (B-H).*

The measurements show an exponentially rising swelling degree with higher ratios of MEDSAH (Figure 17). PHEMA here has a swelling degree of 195 %. Rising to 1140 % at a ratio of 50 wt% MEDSAH.

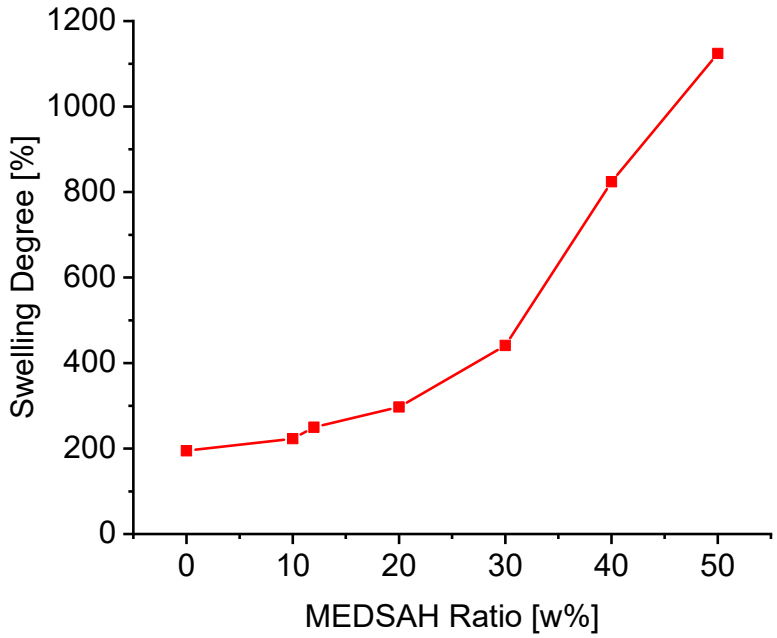

Figure 17: *Swelling degree of P(HEMA-co-MEDSAH) in different ratios in bulk.*

Since the ratio of HEMA:MEDSAH 88:12 wt% was found to provide the fastest reaction for SIPGP as described earlier, this ratio is used for this work. Including water, the wt% ratio is HEMA:MEDSAH:water 39.6:5.4:55 (see chapter 7.3.3). This ratio is henceforth called HEMA/MEDSAH-solution and the resulting polymer P(HEMA-co-MEDSAH).

4.2.2 Single Coating

To investigate SIPGP on PVDF derivatives, several measurement methods were examined. The following chapters describe advantages and disadvantages of these methods when it comes to investigating surface modifications performed with static SIPGP. Also the used parameters, irradiation time (t_i) and distance between the sample and the light source (d_{ls}), are examined and described.

There is no special contact angle that is in general suitable for biomedical applications. There is huge variety of cells, which are important for biomedical applications and for example proteins play a big role, too. For this the contact angle of a certain device

must be tailored for every specific product.[273,274] A contact angle of around 55° as a goal is used to compare the different methods and parameters in this work, because it is considered a moderate contact angle which provides a good cell adhesion for fibroblasts.[275,276]

4.2.2.1 Contact Angle and parameter examination

The contact angle is an obvious choice to examine these experiments, because the substrates used here are P(VDF-TrFE-CTFE) films if not mentioned otherwise. They are hydrophobic (contact angle of about 87°) and the pursued surface modification is a hydrophilic hydrogel. This is the reason why it is suitable to show the finding of the right parameters to perform SIPGP, as presented in this chapter. The data points of the contact angle measurements are the median of 10 measurements on different spots on the same sample, derived from that are the error bars.

First a 25 W *EXO Terra* lamp and a 3D printed reactor were used to examine the difference between a deoxygenated and a non-treated solution, since SIPGP is a free radical polymerization, where oxygen plays a big role as an inhibitor. The distance between the lamp and the sample (d_{ls}) was 1.5 cm. The preparation of these samples is described in chapter 7.3.5. When the non-treated solution is used, a contact angle of 55° is attained after 20 min (Figure 18). In contrast, the coating performed with the deoxygenated solution reaches this contact angle already after 6-8 min. The delay of the reaction time occurs due to the inhibition by the oxygen during the initiation phase. The reaction ratio of a polymerization between the two monomers is magnitudes slower than between a monomer and oxygen. At the same time, the formed peroxide radical reacts very slow, resulting in an induction period.[277–279] However, not only the reaction time is an advantage of the deoxygenated solution. In addition, the reproducibility plays a huge role here since the diluted amount of oxygen in influenced by different parameters such as temperature or preassure.[279–281]

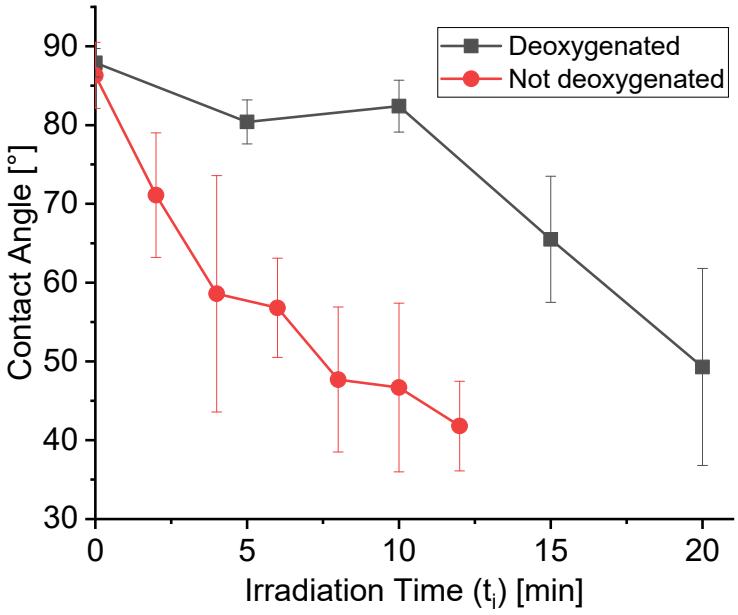

Figure 18: *Comparison between the usage of a degassed (red) and a not degassed (grey) HEMA/MEDSAH solution with a 25 W lamp as UV source.*

In addition to the irradiation time, the type of the lamp also plays a big role, so the 25 W *EXO Terra* lamp (d_{ls} = 1.5 cm) was compared to the 400 W *Dymax 5000 Flood* UV-chamber (d_{ls} = 5.0 cm) (Figure 19). The goal of 55° in contact angle can be measured after 60 s by using the 400 W UV-chamber, though d_{ls} was higher. This indicates, that by using the 400 W UV-chamber the irradiation time can be drastically reduced. Also the homogeneity of the coating seems to be better, because the standard deviation of the contact angle measurements (calculated from 10 measurements on every sample) is decreasing. The preparation of these samples is described in chapter 7.3.5.

However, there is a major drawback of the UV-chamber. It is not only irradiating UV-light, but also produces a lot of heat. Despite being cooled the heat introduction of this lamp to the system must be considered. Note that the heat development during the reaction is a bigger problem while using the 3D-printed reactor, because this reactor itself heats up to around 60 °C in 60 s of irradiation due to absorbing the irradiation of the lamp. The metal reactor in comparison is reflecting a lot of the irradiation and only heats up mildly to around 30 °C (this issue will be discussed in more detail in chapter 4.3.3).

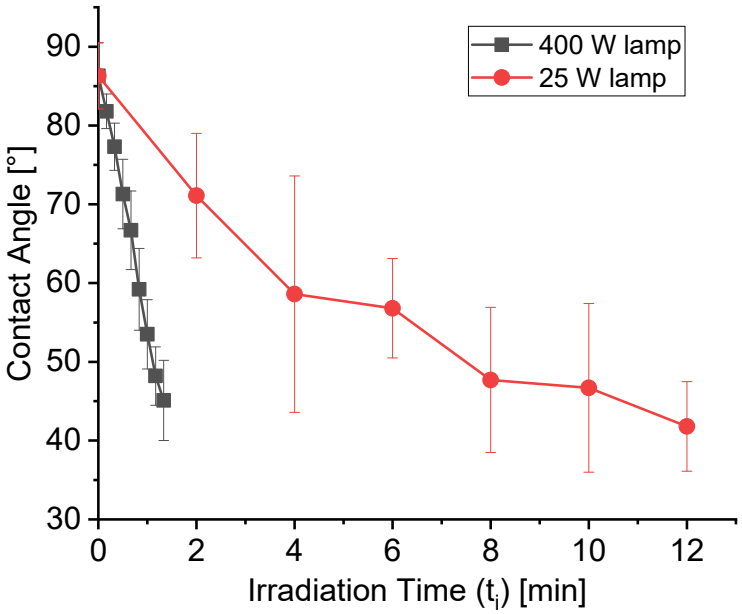

Figure 19: *Comparison of contact angles between using the 400 W lamp (grey) and the 25 W lamp (red) while coating a P(VDF-TrFE-CTFE) film with P(HEMA-co-MEDSAH).*

While using the 400 W UV-chamber the difference in irradiation time to reach a contact angle of 55 °C is much lower, as previously mentioned. There is a linear dependency of the dose of UV-A light at the sample to the irradiation time (Figure 20). As also can be seen, with the dose rising linearly, the contact angle drops linearly, which indicates a direct link between the dose of UV-A light and the contact angle. With this, the irradiation time can be used to adjust the contact angle of the surface while performing static SIPGP. The preparation of these samples is described in chapter 7.3.5.

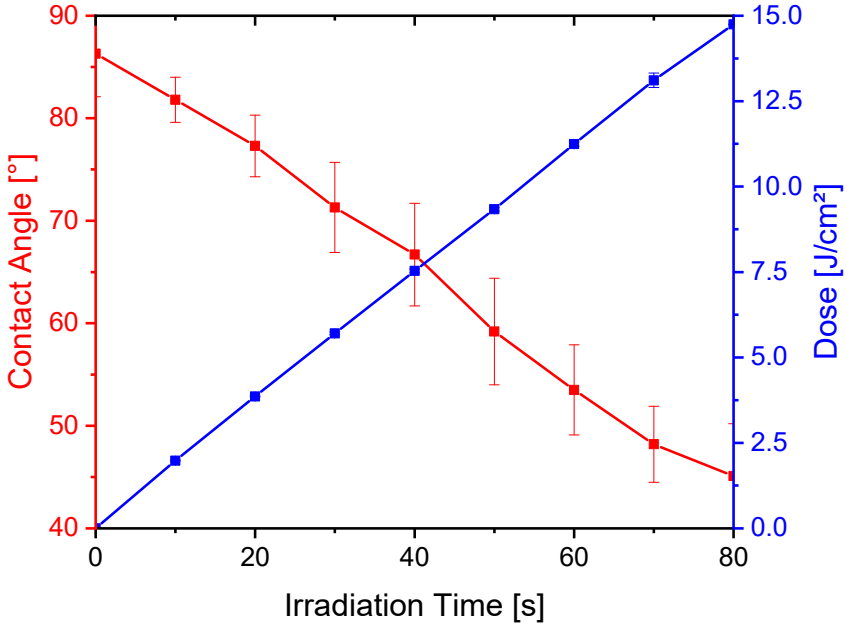

Figure 20: *Contact angle of P(VDF-TrFE-CTFE) films coated with P(HEMA-co-MEDSAH) under a series of irradiation times using a deoxygenated HEMA/MEDSAH solution (red) under radiation of a 400 W lamp with and the corresponding dose of UV-A light at the sample (blue).*

The distance between the light source and the sample (d_{ls}) also is an important parameter. Together with the irradiation time, it sets the dose of irradiation the sample is exposed to during the reaction. While the relation between the irradiation time and the dose is linear, the dose is quadratic dependent on d_{ls}, if the light source is considered to be a point source. Because the same amount of irradiation per time is distributed onto the surface of a sphere with the radius being the distance between the point source and the sample.

$$A = 4\pi r^2$$

This equation shows, that the surface of the sphere A is quadratic dependent on the radius r. So the impact of this while using the 400 W UV chamber with t_i = 60 s and d_{ls} = 2.4 cm - 15.4 cm is examined (Figure 21). The distance steps for the measurement are 1.3 cm, because the used UV chamber contains pre-set steps of this distance. The dose shows a slight quadratic dependence to the distance, while the contact angle drops very low with a d_{ls} = 2.4 cm and d_{ls} = 3.7 cm. We do not find a perfect quadratic dependence here, because the mercury lamp in the UV-chamber is not a point source, but as a light bulb can be considered to have a point source character.

Here not only the irradiation dose might play a role, but also the heat introduced by the lamp, this too increases whit the sample getting closer to the lamp. After the coating procedure with d_{ls} = of 2.4 cm and d_{ls} = 3.7 cm with t_i = 60 s, the silica glass is even too hot to remove it with bare hands from the setup.

However, this shows, that not only t_i can be used to adjust the contact angle, but also d_{ls} can be utilized if a specific irradiation time is needed. The preparation of these samples is shown in chapter 7.3.5.

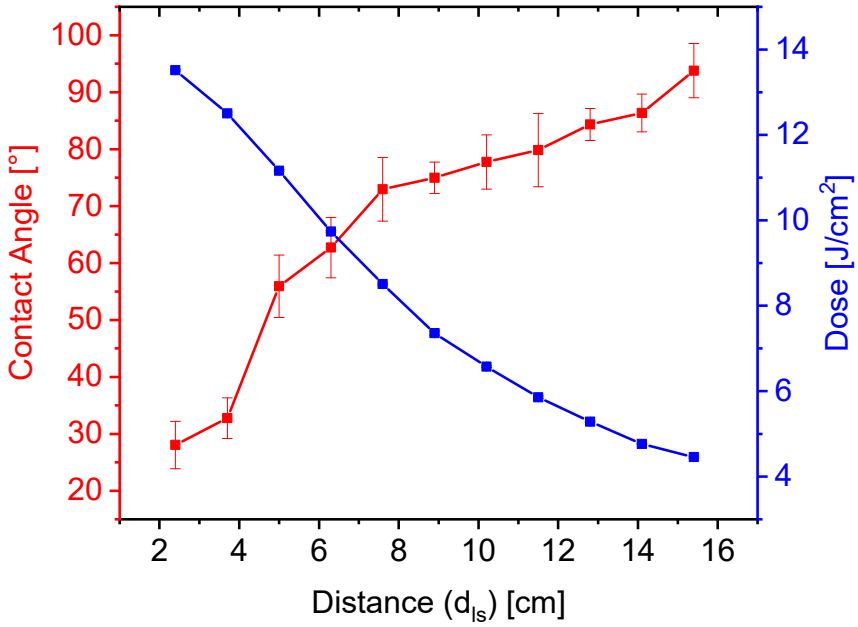

Figure 21: *Contact angle of P(VDF-TrFE-CTFE) films coated with P(HEMA-co-MEDSAH) under a series of distances between sample and light source (red) with the corresponding dose of UV-A light a the sample (blue)*

When it comes to finding the best SIPGP parameters to carry out the following experiments, different considerations have to be taken into account. One is that a lower t_i saves time, especially if a high throughput of samples is required. Also in respect to dynamic SIPGP a lower t_i means a lower amount of monomer solution needed to perform the reaction (for more on that look at chapter 4.3). So d_{ls} should be chosen as low as possible. However, as previously described, the d_{ls} = 2.4 cm and d_{ls} = 3.7 cm are not very suitable, because of the higher heat input into the setup. An additional factor is, that the workspace inside this UV-chamber gets narrower, when closer distances are used and d_{ls} = 2.4 cm and d_{ls} = 3.7 cm make it harder for the workflow. For these

reasons d_{ls} = 5 cm was chosen. The contact angle measurements in Figure 20 were performed with d_{ls} = 5 cm. The goals of 55° in contact angle is here reached after t_i = 60 s, so this is the irradiation time that is used for further experiments.

Note that these parameters can only be used with this specific setup. A different reactor or different lamp / UV-chamber will change the outcome of the results. With changing the setup, the parameters have to be adjusted to the new setup.

To proof the covalent nature of the coating, a soxhlet extraction with methanol of a P(VDF-TrFE-CTFE) film coated with P(HEMA-co-MEDSAH) was performed (more detail in chapter 7.3.5). The contact angle before (49.1±5.3°) and after (51.6±2.1°) the extraction stayed the same taking the deviation into account.

So far only the terpolymer P(VDF-TrFE-CTFE) was coated, but due to the mechanism of SIPGP, the same experiments are supposed to work with the homopolymer PVDF and the copolymer (PVDF-TrFE) (Figure 22). This graph shows contact angle measurements of uncoated homo-, co- and terpolymer films and coated ones with the parameters used as previously described. This shows that the procedure can be performed on all three derivatives of PVDF.

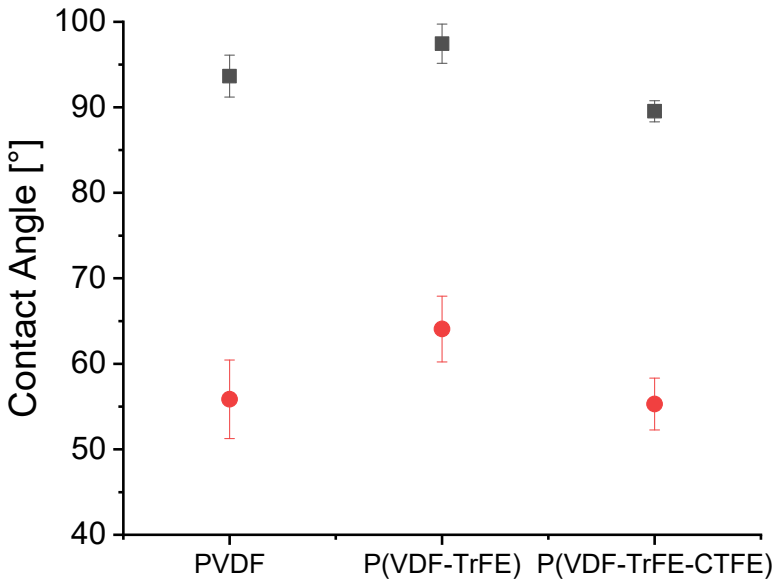

Figure 22: *Contact angle of P(HEMA-co-MEDSAH) coated PVDF, P(VDF-TrFE) and P(VDF-TrFE-CTFE) films after irradiation time of 60 s (grey) and pristine films (red).*

It has been demonstrated, that the contact angle is a measurement method that is capable of depicting the procedure of SIPGP on films quite well and can also function as a control of the reaction parameters or a way to find new ones for different purposes. However, the measurement of the contact angle has its weaknesses, too. Not only the coating itself plays a role when it comes to the contact angle, also the topology of the surface plays a big role and must be taken into consideration, especially if the material or type of substrate is changed. There also will always be an error in the contact angle measurements, which requires at least 5 measurements on every sample (or as in this work 10). So this method is too time extensive for fast reaction controls. However, for this reason for example IR spectroscopy can be utilized.

4.2.2.2 Fourier-Transform Infrared Spectroscopy

Measuring an IR spectrum is the fastest way to measure the P(HEMA-co-MEDSAH) coating on films of PVDF derivatives. All of the following FT-IR spectra are normalized to 1 at the peak at ~ 1400 cm^{-1}. This peak is assigned to C-H bonds, which can be found in all the substrates and the coating, which makes it a good choice to normalize to. By doing this, the measured spectra get more comparable.

The most important peak here is the carbonyl vibration at ~ 1723 cm^{-1}. The methacrylate moiety that HEMA and MEDSAH possess, contains the C=O double bond while none of the three used PVDF derivatives do. Figure 23 shows the spectra of a pristine P(VDF-TrFE-CTFE) film and one that was coated with P(HEMA-co-MEDSAH). The spectrum of the coated polymer film shows a peak at 1727 cm^{-1}. Also at 3411 cm^{-1} the signal of the hydroxyl group of HEMA can be seen but is very weak and in this case too weak to proof a successful coating, unlike the carbonyl peak.

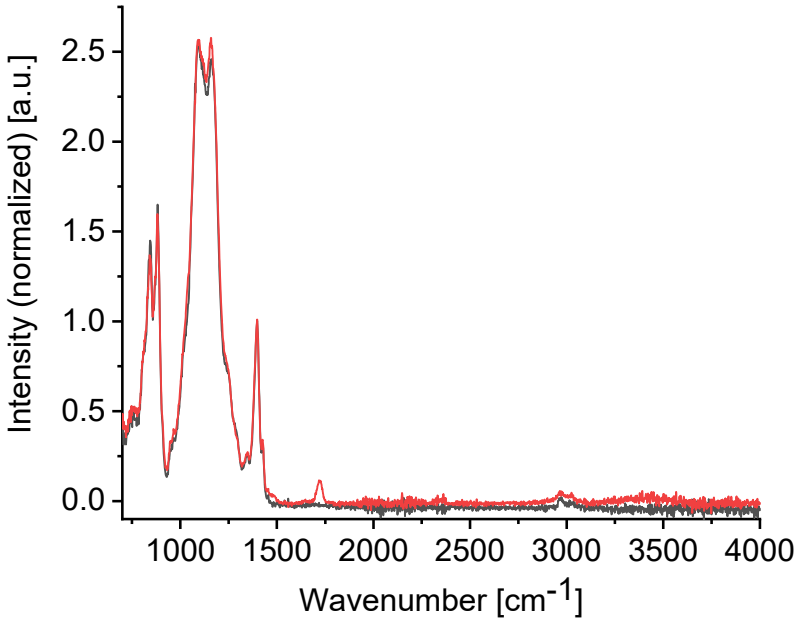

Figure 23: *IR spectra of a pristine P(VDF-TrFE-CTFE) film (black) and a P(HEMA-co-MEDSAH) coated one (red).*

Table 3 lists more important peaks of these two spectra and shows that there are four different peaks that could help differentiate between the coating and the substrate. However, missing peaks at 844 cm^{-1} and 1159 cm^{-1} cannot be used to determine the presence of a coating, because there are uncoated areas distributed over the sample as well, which cause the appearance of C-F bond vibrations on coated films, too (for according SEM images see the following chapter).

Table 3: *IR vibration bands of P(VDF-TrFE-CTFE) coated with P(HEMA-co-MEDSAH). With the peaks marked with a "–" and red when the polymer does not show the peak and a "+" and green when it does.*

Wave number [cm^{-1}]	Vibration	P(VDF-TrFE-CTFE)	P(HEMA-co-MEDSAH)
844	$v_a(CF_2)$	+	-
882	$v_s(CH_2)$	+	+
1094	$v_a(CC)$	+	+
1159	$v_s(CF_2)$	+	-
1398	$\sigma(CH_2)$	+	+
1723	$v(CO)$	-	+
2973	$v(CH)$	+	+
3392	$v(OH)$	-	+

The peak assigned to the hydroxyl group is a little stronger in the spectrum of the P(HEMA-co-MEDSAH) coated P(VDF-TrFE) (Figure 24), but still too weak to be considered as a proof. The carbonyl peak at 1727 cm^{-1} on the other hand can provide exactly that.

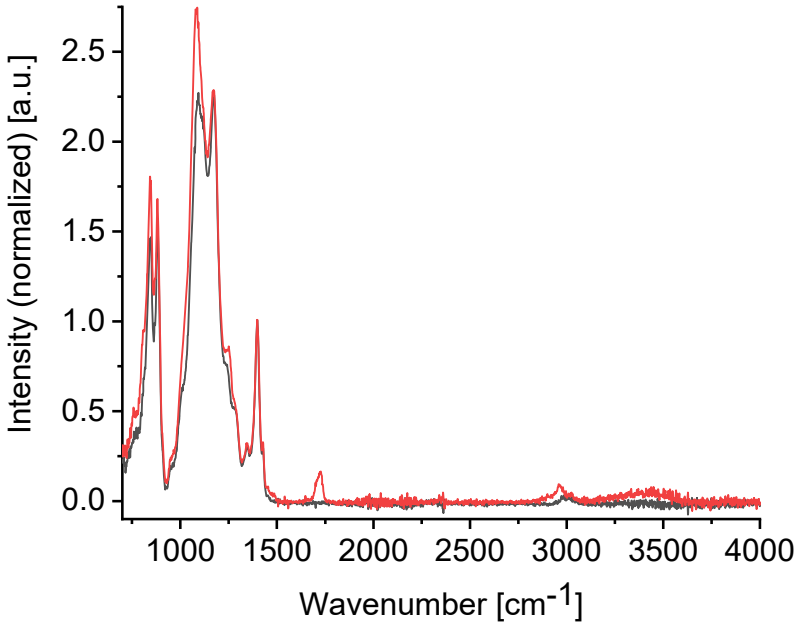

Figure 24: *IR spectra of a pristine P(VDF-TrFE) film (black) and a P(HEMA-co-MEDSAH) coated one (red).*

The peaks of pristine and coated films of P(VDF-TrFE-CTFE) and P(VDF-TrFE), as expected, look very similar, since the only difference is the Cl-C bond that P(VDF-TrFE-CTFE) has and P(VDF-TrFE) does not. This peak can be expected at ~ 730 cm^{-1}, where a small shoulder can be seen (Figure 23), however only to a very small extent. Table 4 shows the major peaks of the coated and uncoated P(VDF-TrFE) film.

Table 4: *IR Vibration bands of P(VDF-TrFE) coated with P(HEMA-co-MEDSAH). With the peaks marked with a "–" and red when the polymer does not show the peak and a "+" and green when it does.*

Wave number [cm^{-1}]	Vibration	P(VDF-TrFE)	P(HEMA-co-MEDSAH)
844	$\nu_a(CF_2)$	+	-
882	$\nu_s(CH_2)$	+	+
1080	$\nu_a(CC)$	+	+
1172	$\nu_s(CF_2)$	+	-
1398	$\sigma(CH_2)$	+	+
1727	$\nu(CO)$	-	+
2960	$\nu(CH)$	+	+
3411	$\nu(OH)$	-	+

Also for the pristine PVDF the spectra of pristine and P(HEMA-co-MEDSAH) coated films are compared (Figure 25). Here not only the carbonyl peak at 1724 cm^{-1} can be seen clearly, but also the hydroxyl peak at 3410 cm^{-1} clearly appears here.

The spectra of PVDF compared to the ones of its previously mentioned co- and terpolymers look quite different. The reason for that is, that PVDF can be arranged in different phases. The co- and terpolymer have a higher ratio of the β-phase than the homopolymer, which has a higher ratio of the α-phase. These phases lead to different appearances in the FT-IR spectra. This aspect is even used to determine the ratio between the phases in PVDF derivatives.[5]

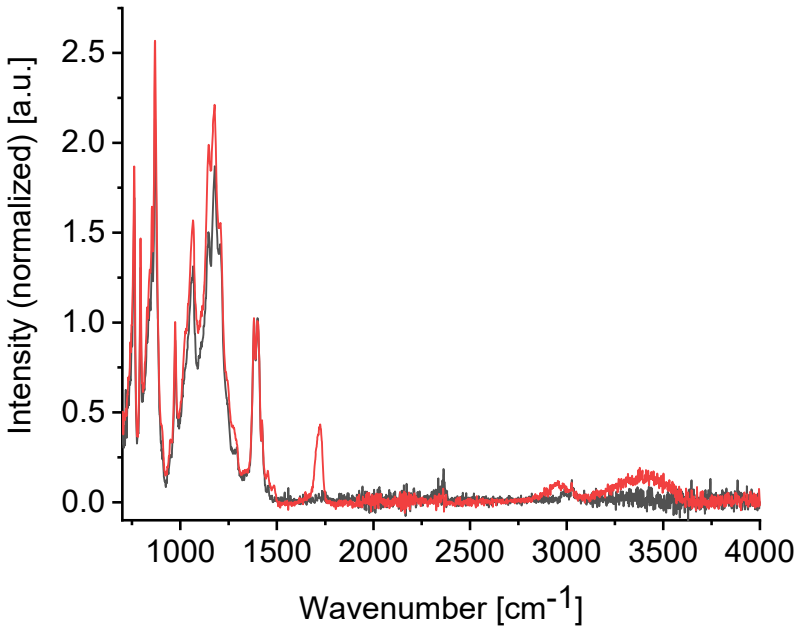

Figure 25: *IR spectra of a pristine PVDF film (black) and a P(HEMA-co-MEDSAH) coated one (red).*

The major peaks of the spectra showing pristine and coated PVDF are shown in Table 5.

Table 5: *IR Vibration bands of PVDF coated with P(HEMA-co-MEDSAH). With the peaks marked with a "–" and red when the polymer does not show the peak and a "+" and green when it does.*

Wave number [cm^{-1}]	Vibration	PVDF	P(HEMA-co-MEDSAH)
869	$v_s(CH_2)$	+	+
1066	$v_a(CC)$	+	+
1177	$v_s(CF_2)$	+	-
1400	$\sigma(CH_2)$	+	+
1724	$v(CO)$	-	+
2954	$v(CH)$	+	+
3410	$v(OH)$	-	+

Note that the intensity of the important peaks for this coating is varying, when measuring at different spots on the sample. Since this coating is a hydrogel there are differences between dry samples and wet/swollen samples. Measuring wet samples can be a method to make the coating more detectable, if there is only a very thin coating on the films. By doing so the intensity of the hydroxyl group is rising, because the water content in the coating is rising. However this is only a way to measure the coating indirectly by measuring the contained water, which would not occur on pristine PVDF derivative films.

For a closer look at the surface of the coating however, imaging methods must be utilized, for example the scanning electron microscope.

4.2.2.3 Scanning Electron Microscopy

Surface modifications require an analysis of surfaces to provide more insight in the topology of the coating and the process during the coating. The *scanning electron microscope* (SEM) is a good way to analyse the surface of the coated samples.

The observed surface structure of pristine P(VDF-TrFE-CTFE) films (Figure 26 A) looks similar to small worms and is characteristic for these films. In the following it will be called worm-like structure. The P(HEMA-co-MEDSAH) coated samples (Figure

26 B-D) were coated with d_{ls} = 5.0 cm with the light source being the 400 W UV-lamp. At an irradiation time of t_i = 40 s (Figure 26 B), the worm-like structure can still be seen. However, now there is a net structure that is forming on top of the sample. In the bottom right hand corner of the image there are spots, where the coating is beginning to be closed and form a smooth surface (Figure 26 B red arrow). When t_i = 80 s (Figure 26 C), there are no worm structures of the pristine film anymore, but instead there is a smooth surface that is the P(HEMA-co-MEDSAH) coating. Despite this indicating a complete and homogeneous coating, other spots on the same sample (Figure 26 D) show that there are also defects in the coating and that the coating is not homogeneous over the whole sample. There, in the top right-hand corner (Figure 26 green arrow), the homogeneous coating can be observed, but the rest of the sample is only poorly coated.

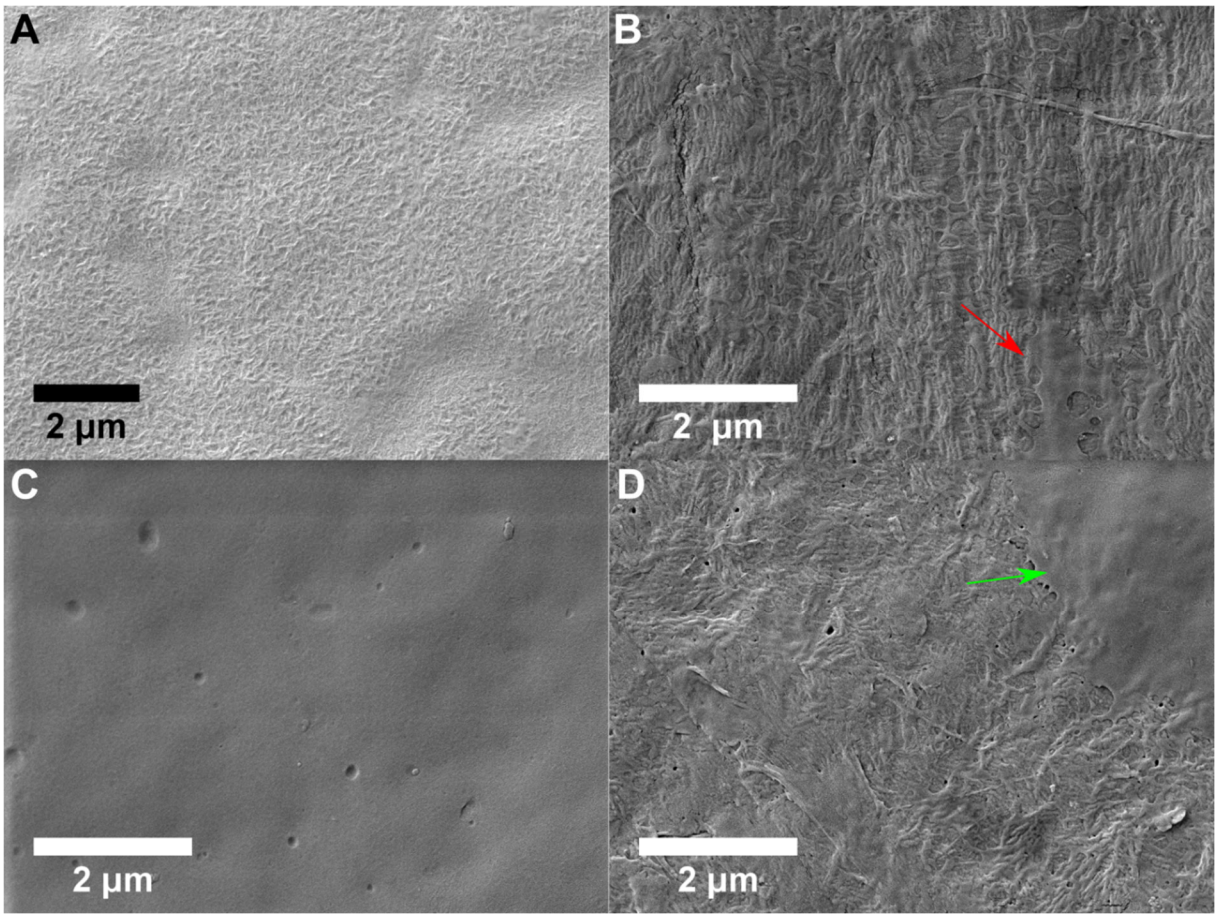

Figure 26: *SEM images of a pristine P(VDF-TrFE-CTFE) film (A), of a P(HEMA-co-MEDSAH) coated P(VDF-TrFE-CTFE) film that was irradiated for 40 s (B) and of a sample that was irradiated for 80 s (C, D). The red and green arrows mark the coating.*

These images can help to understand why during the coating the contact angle does not drop immediately, as it would, if the coating starts off as a thin monolayer. Instead the contact angle drops linearly with the rise of the irradiation time as previously shown in Figure 20. What can be observed in Figure 26 B however, indicates that the coating process begins at different spots on the sample and then fills the gaps with longer irradiation time. This leads to a continuous drop of the contact angle, because during the process the ratio between coated and uncoated spots on the surface shifts towards the coated spots with higher t_i. In addition, the topology of the sample is much more rough and unsteady at t_i = 40 s and gets more smooth and homogenous with t_i = 40 s, only with some defects (Figure 26 D).

This shows that SEM is a good method to provide information about the topology of the coating and the process of the coating. This method also proofed to be a good reaction control, because it is easily possible to distinguish between the topology of the sample and the coating.

4.2.2.4Fluorescence microscopy

Another way to proof a successful coating can be provided by fluorescence spectroscopy. To achieve that, a methacrylate functionalized fluorescent dye can be added to the monomer solution before polymerizing. Here fluorescein-O-methacrylate was used. After washing, the sample was embedded in silicone and then cut with a scalpel to be able to measure the cross section of the sample (more detailed information in chapter 7.3.6).

The measurements were performed by Sebastian Hasselmann at *Fraunhofer ISC* in Würzburg, Germany. The fluorescence image of this cross section of the sample (Figure 27) shows a black area in between two green areas. The black one matches with the thickness of the P(VDF-TrFE-CTFE) films stated by the manufacturer of 10±1 µm. So the green areas are the coatings on the upper and lower side of the film. This method can be utilized to make the coating visible. By that it can be used to examine homogeneity of the coating as done in chapter 4.4. However, by adding a monomer to the monomer solution, it is a slightly different system, which makes is less

comparable to other measurements. To avoid that, the fluorescein can also be added after the polymerization. This was done in chapter 4.4, where scaffolds are coated, because this method is more suitable for measuring coated scaffolds then coated films.

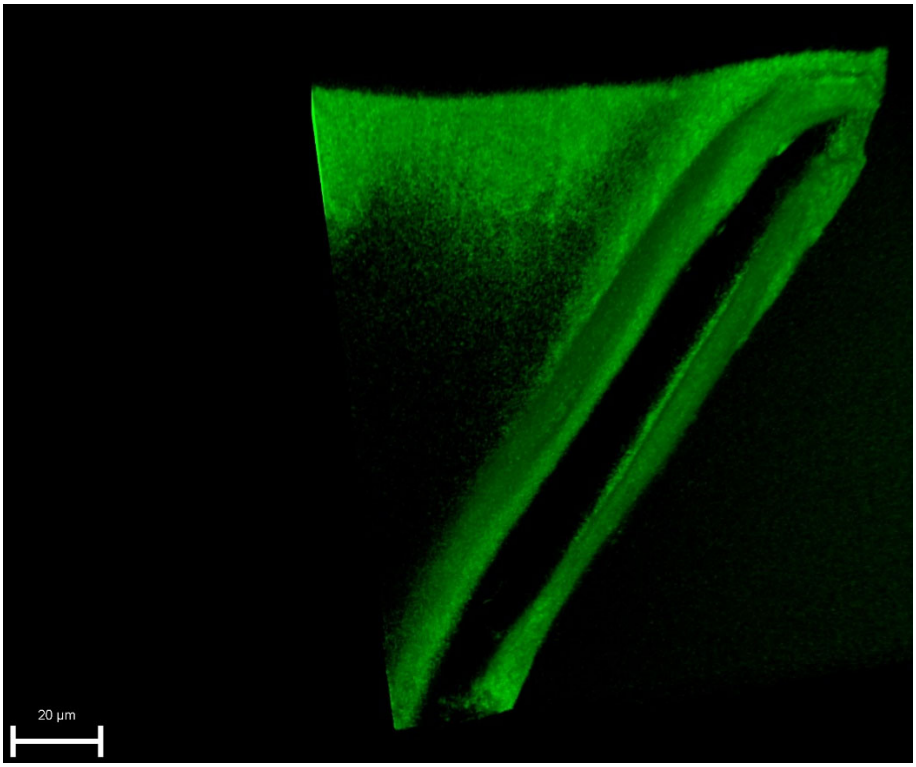

Figure 27: *Fluorescence image of the cross section of a P(VDF-TrFE-CTFE) film that was coated with P(HEMA-co-MEDSAH) containing fluorescein-O-methacrylate.*

4.2.2.5 Macroscopic movement of the coated films

The presence of a hydrogel coating can not only be observed with microscopic methods or other measurements, it also adds a macroscopically visible effect to the films. As could be seen in the previous chapter, the coating is present at both sides of the film. However, because parts of the UV light is absorbed by the film, the coating on the down side of the film is slower than on the upper side of the film, as Julian Glock could show in his bachelor thesis.[282]

This phenomenon can be observed at P(VDF-TrFE-CTFE) films coated with P(HEMA-co-MEDSAH) (Figure 28). The coating of these films was performed with t_i = 60 s and d_{ls} = 5 cm. When drying the films after coating, they start to curl. When the film is put into a petri dish containing some water, the air humidity is relatively low, when the dish is open (Figure 28 A). When the lid is being put on top of the dish (Figure ***28*** B), the humidity inside the dish starts to rise immediately and the film starts to uncurl within 20 s. This macroscopic movement is reversible and was repeated 10 times.

The curling and uncurling of the film with alternating humidity shows several things. First, the coating of the film is a hydrogel. It is responsive to humidity and shrinks or expands with it. During the reaction, the films polymerize in an aqueous environment and thus polymerize in a “swollen state” and while drying the coating is shrinking and moving the film with it. This shows secondly, that the coating is strongly attached to the film, because otherwise the coating would rip off the film instead of moving the film with it. And third, this shows that the coating does not consist of one dimensional strands, but consist of a three dimensional cross-linked network.

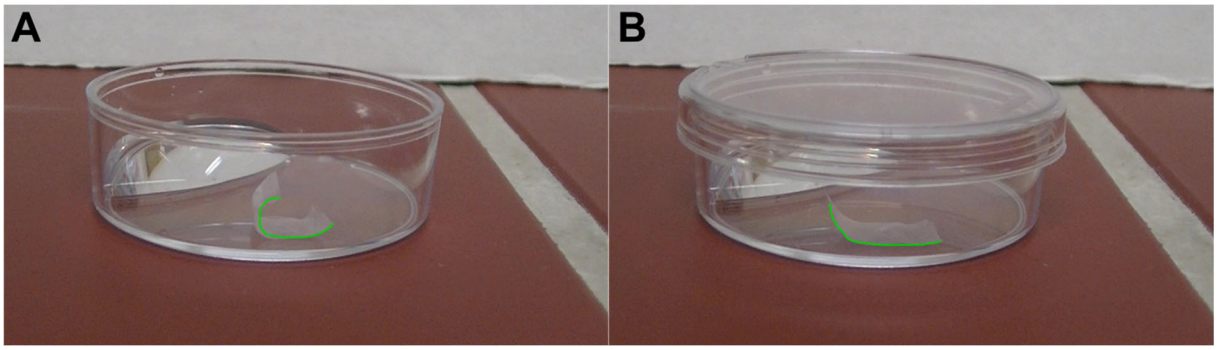

Figure 28: *P(HEMA-co-MEDSAH) coated P(VDF-TrFE-CTFE) film in a petri dish containing a drop of water without the lid (A) and with its lid (B). The green line represents the edge of the coated film.*

In order to find out the water uptake of these coatings, dynamic vapour sorption measurements were performed.

4.2.2.6 Dynamic vapour sorption

The following data was already published in the bachelor thesis of Julian Glock, but are presented here with permission to complement the picture on the SIPGP-hydrogels.[282]

First the water uptake of the bulk polymers from different ratios in the monomer solution between HEMA and MEDSAH were tested via dynamic vapour sorption (DVS). The bulk polymers were fabricated as described in chapter 7.3.4. The measurements were performed by Stephan Braxmeier at the *Zentrum für angewandte Energietechnik* (ZAE) in Würzburg, Germany. With this method the temperature inside the device was kept at 25 °C and the air humidity was increased from 0 % to 90 % and then decreased to 0 % with steps of 10 %. Figure 29 shows the results of these measurements, while only presenting the swelling degree measured at 90 % air humidity (for the data of the other air humidity steps see chapter 7.3.7). This shows, that the swelling degree rises with higher MEDSAH ratios in the used HEMA/MEDSAH monomer solution. This finding was already presented in chapter 4.2.1. However in contrast to these previously shown measurements the rise of the swelling degree does not increase with every ratio step of MEDSAH, but instead does stagnate. The reason for this is the difference between a swelling degree measurement with samples immersed in water, where the water uptake will reach its maximum, and a measurement in 90 % air humidity, where the concentration of water in the air and the concentration of water in the air reaches an equilibrium and cannot be surpassed.

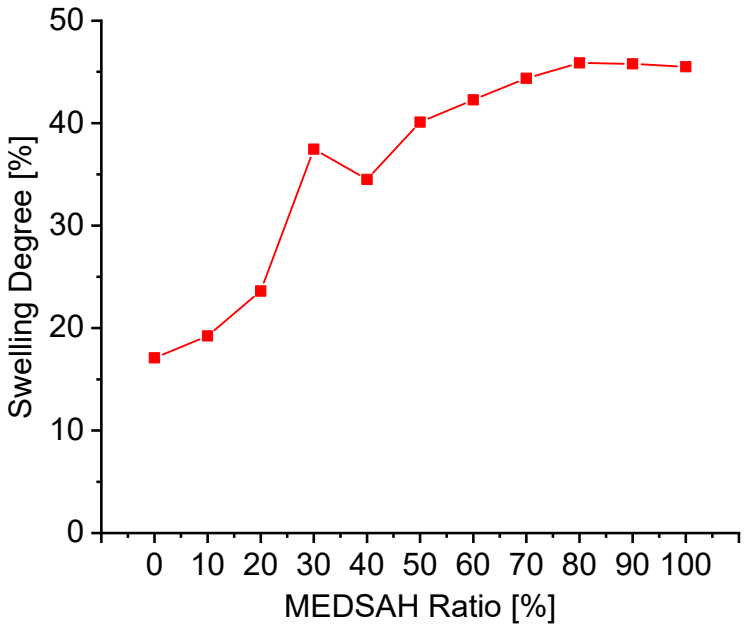

Figure 29: *Swelling degree of different bulk P(HEMA-co-MEDSAH) with varying MEDSAH ratios in respect to HEMA at 25 °C and 90 % air humidity measured by dynamic vapour sorption.*

The same measurements were then executed with P(VDF-TrFE-CTFE) films, that were coated with the 400 W lamp,t_i = 60 s and d_{ls} = 5 cm. Figure 30 shows the results of these measurements while only presenting the swelling degree measured at 90 % air humidity (for the data of the other air humidity steps see chapter 7.3.7). There no swelling can be seen in the data up to a MEDSAH ratio of 90 % and with a strong increase of the coating of pure PMEDSAH. The reason for that is probably the accuracy of the measurement device. The balance in the used device has an accuracy of ±10 µg. Though 5 samples each were used at the same time the combined weight of the 5 samples for each ratio was between 10 mg and 20 mg. Since only a small portion of this weight is the coating, the water, that was upatken, could not be measured by the balance in the device.

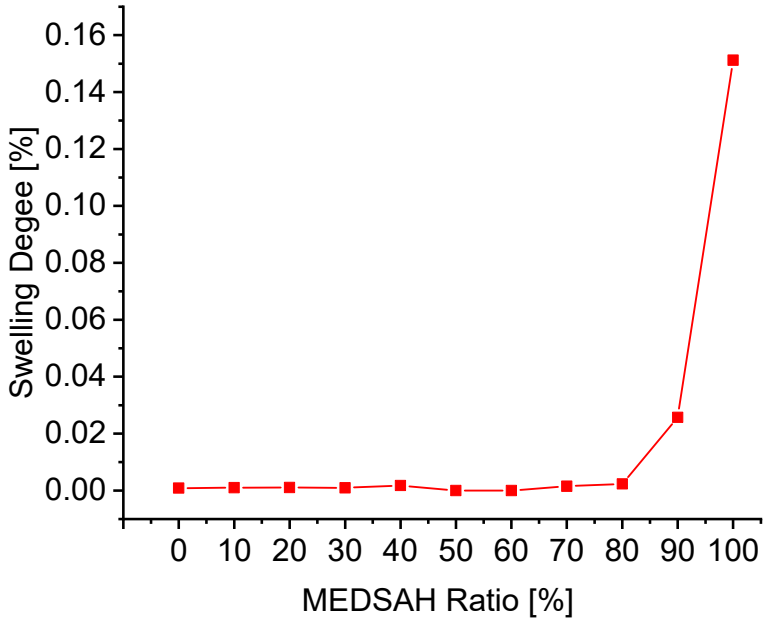

Figure 30: *Swelling degree of different P(VDF-TrFE-CTFE) films coated with P(HEMA-co-MEDSAH) with varying MEDSAH ratios in respect to HEMA at 25 °C and 90 % air humidity measured by dynamic vapour sorption. The samples were irradiated for 60 s with a distance to the light source of 5 cm.*

However, these measurements showed, that a pure PMEDSAH coating has the greatest water uptake abilities amongst these ratios. For this reason these samples were also measured with an environmental SEM.

4.2.2.7 Environmental SEM

The following measurements were performed by Andreas Frank at the *University of Bayreuth* in Bayreuth, Germany.

The samples used for this measurement were the PMEDSAH coated P(VDF-TrFE-CTFE) samples used in the previous chapter. The samples were frozen with liquid nitrogen and were then broken in the middle of the sample in order to be able to look at the cross section of the coated films (Figure 31 A, B). The images show the coating (green) on both sides of the film (images without colouring in chapter 7.3.8). Here one advantage of an environmental SEM comes into play. If these results are

being compared to the “normal” SEM results presented in chapter 4.2.2.3, the difference in contrast between the substrate and the coating is striking. This contrast appears due to the water content inside coating, which is another proof of the coating being a hydrogel. On one side of the film the coating is partly ripped off the surface. The reason for this could be the strong tensions between coating and surface during the drying and wetting due to the water uptake of pure PMEDSAH. This shows that for PMEDSAH the covalent bonds between the coating and the surface are less in number and thus overall weaker that inside the coating itself. This leads to cracks in the coating, which can also be observed with the environmental SEM (Figure 31 C, D).

When air humidity inside the device is 99.5 % with a temperature of 2 °C (Figure 31 C), the marked gap is 16.56 µm. The same gap under 42.4 % air humidity and otherwise same conditions (Figure 31 D), is 30.34 µm. This can be observed, because for these measurements no sputtering of the samples was necessary. These movements again show the hydrogel nature of the coating and the extent of swelling of the PMEDSAH coating.

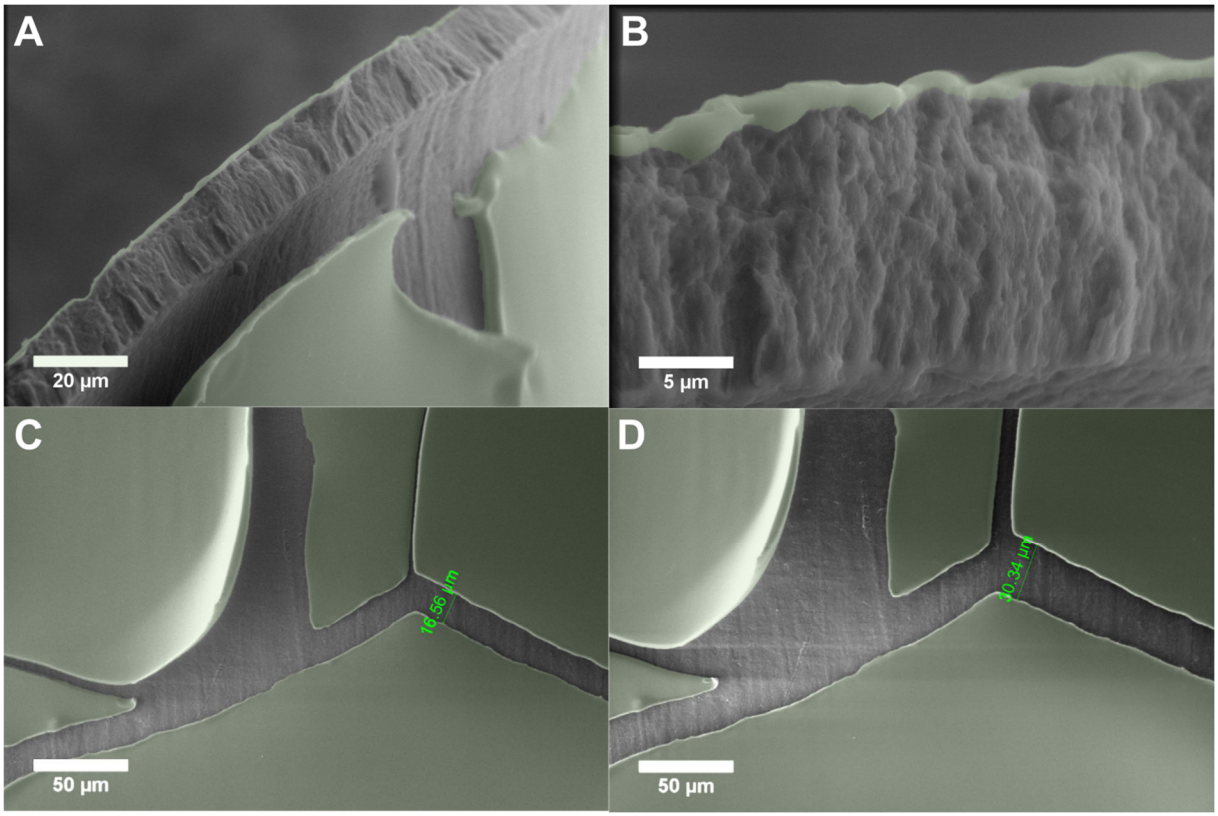

Figure 31: *Environmental SEM images of P(VDF-TrFE-CTFE) films coated with PMEDSAH (coating material is coloured in green, non-coloured version in Figure 64). View at a broken edge of the film (A) with inset (B). Distance of a crack measured on the film with an air humidity of 99.5 % and 2 °C (C) and an air humidity of 42.4 % and 2 °C (D).*

4.2.3 Conclusion

In the previous chapters the parameters for static SIPGP for the custom designed reactor were examined by utilizing for example measurements of contact angle, IR spectroscopy and scanning electron microscopy. Suitable parameters found were to deoxygenate the solutions while performing the reaction inside the 400 W UV lamp at t_i = 60 s and d_{ls} = 5 cm. These parameters are now used to compare static SIPGP to dynamic SIPGP in the following chapters.

4.3 Dynamic SIPGP on Films of P(VDF-TrFE-CTFE)

As previously shown, the performance of static SIPGP is fast and easy to perform. However, it has some major disadvantages.

Because of the monomer solution absorbing some of the UV light, the intensity of the light is highest at the top of the solution and is attenuated while passing through the solution. Because of this a lot of bulk polymer is forming inside the monomer solution. This bulk polymer is sometimes attached to the coating, which makes the coating quite inhomogeneous. In addition to that, there are defects in the coating, where there is no coating at all on the sample.

A possible way to prevent this is to apply a constant flow of monomer solution to the reaction chamber. This will not prevent the formation of bulk polymer but could flush out a huge amount of the bulk in order to not get attached to the sample.

Following, the newly developed process of dynamic SIPGP is described and evaluated.

Note that for all the studies of dynamic SIPGP the parameters were d_{ls} = 5.0 cm and t_i = 60 s, while using P(VDF-TrFE-CTFE) films as a substrate. The equipment used were the 400 W UV chamber and the metal reactor to perform the dynamic SIPGP in.

4.3.1 Structure of the dynamic SIPGP-setup

For the performance of dynamic SIPGP a constant flow of monomer solution must be applied to the system during the coating procedure. This is possible with both previously described reactors (chapter 4.1).

A syringe pump (Figure 32 A) and a drain (Figure 32 H) are attached to the reactor body to provide a constant monomer flow through the reaction chamber during the coating procedure. Two walls (Figure 32 D) are inserted to fix the sample (Figure 32 F) during the process. A silica glass (Figure 32 C) is placed at the top of the reactor to enable an inert gas atmosphere, which is provided over an argon inlet (Figure 32 B).

This setup can provide a constant monomer flow under an inert gas atmosphere. By turning on the UV source (Figure 32 G) the reaction can be started.

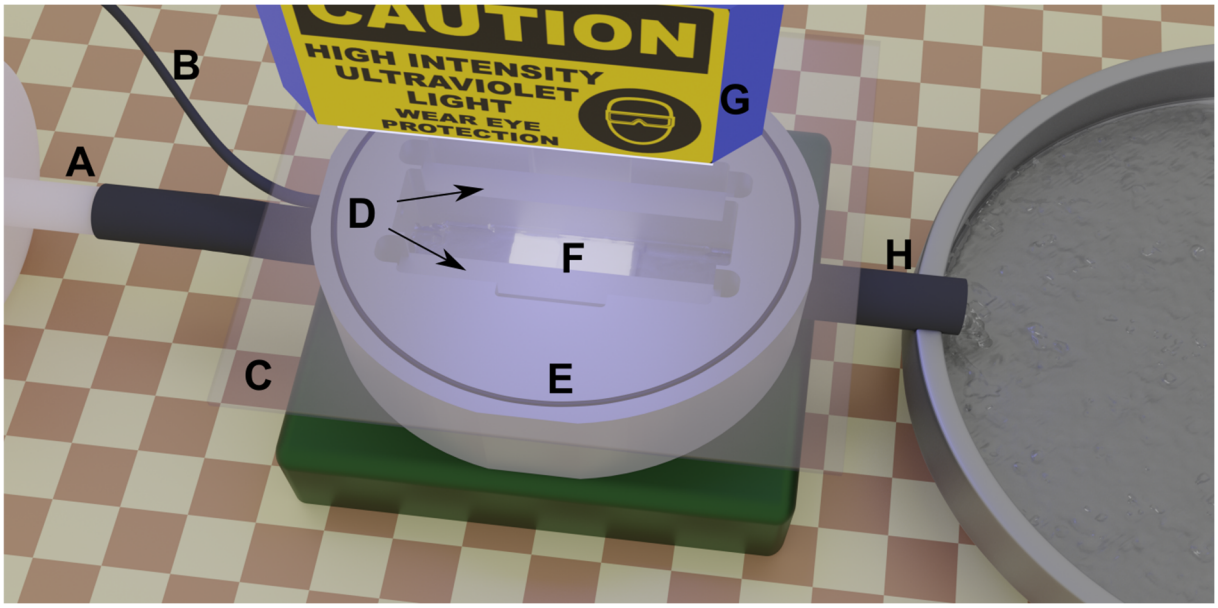

Figure 32: *Image of the setup for dynamic SIPGP including: A syringe pump and inlet (A), argon inlet (B), cover silica glass (C), two walls (D), reactor body (E), sample (F), UV lamp (G) and the outlet and drain (H).*

4.3.2 Contact Angle

As for the static SIPGP, the contact angle is a good way to find out about the performance of dynamic SIPGP and to learn something about the differences between those two processes.

Flow rates (r_{fl}) between1 ml/min and 10 ml/min in 1 ml/min steps were performed to explore the correlation between different flow rates and the corresponding contact angle (Figure 33, the results in tabular form can be found in chapter 7.3.9). The contact angle is rising from 49° at 1 ml/min to 83° at 6 ml/min in a linear fashion. From r_{fl} = 6 ml/min to r_{fl} = 10 ml/min the corresponding contact angle is not rising anymore but reaches a plateau. This plateau corresponds to the contact angle of the pristine P(VDF-TrFE-CTFE) which is 87°. This indicates, that at r_{fl} = 6 ml/min or more, there is no coating formed under the chosen parameters. The linear rise of the contact angel

between r_{fl} = 1 ml/min and r_{fl} = 5 ml/min indicates, that the coating procedure is slowed down with applying higher flow rates. Without a flow applied, the monomers can easily align to the surface in the right position for the reaction. With a flow applied however, the alignment is disturbed, which leads to a slower reaction. This effect is increased with higher flow rates.

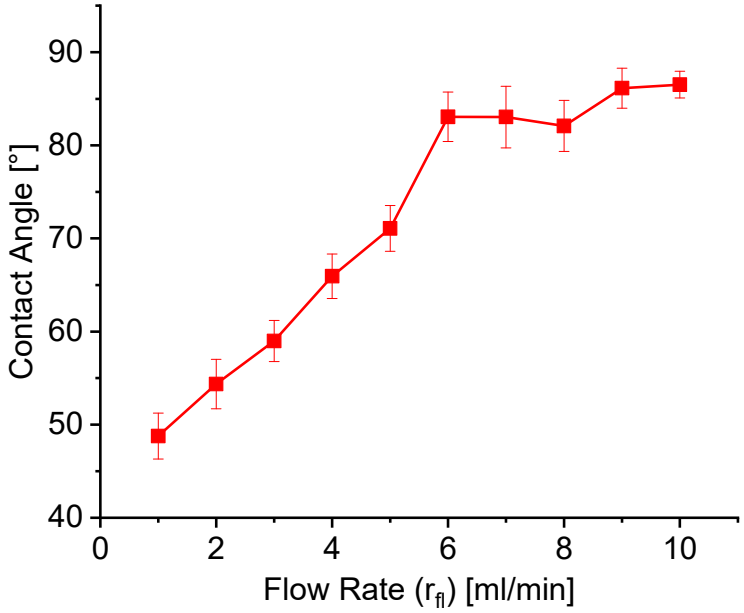

Figure 33: *Contact angle measurement of P(VDF-TrFE-CTFE) films coated with P(HEMA-co-MED-SAH) under dynamic SIPGP with flow rates between 1 ml/min and 10 ml/min.*

This indicates that the new parameter of flow rate, which is introduced with dynamic SIPGP, can be used as an additional tool to adjust the performance of this mechanism. However, the amount of “wasted” monomer solution has to be taken into account when using dynamic SIPGP, especially with high flow rates.

Another thing to consider are the calculations that were described earlier (chapter 4.1.3 Figure 15 F). These calculations imply the fact that during a constant flow inside the reactor there is a difference in solution velocity between the walls of the reactor and centre of the flow channel (in theory the solution velocity on top of a solid is 0 cm/min). This difference increases, when higher flow rates are applied. This too must be considered when choosing the right flow rate for a system. In order to find out how the

actual results fit the calculations, a series of r_{fl} = 1 ml/min to r_{fl} = 5 ml/min was performed (Figure 35) and the contact angle was measured on the right side, the left side and the middle of the sample that are at the 0.0 cm, 0.5 cm and 1.0 cm marks at the cross section of the sample (Figure 34).

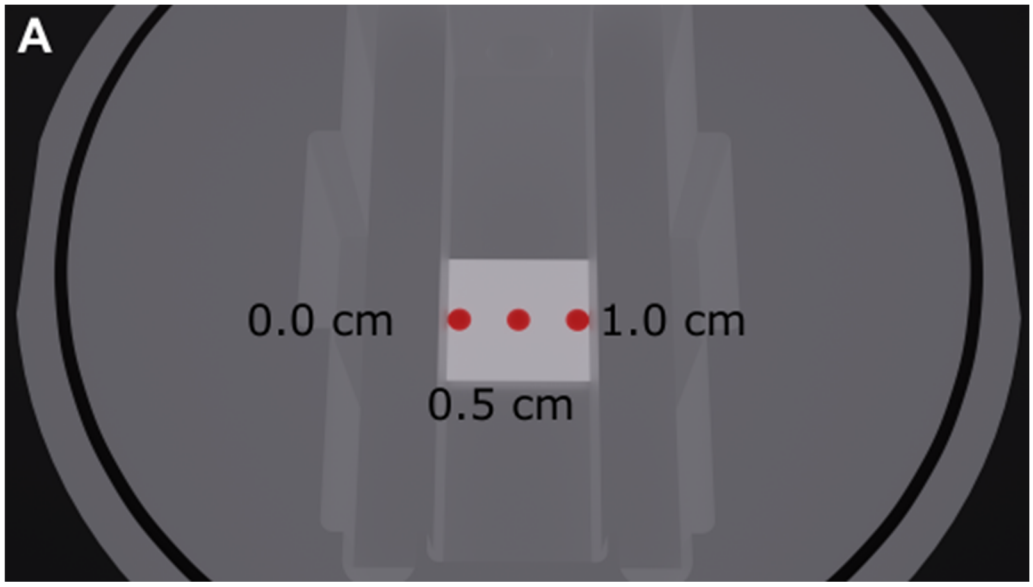

Figure 34: *CG-Image of the reactor with the sample (white) inside. The three dots at the sample are the locations on which the contact angle is measured.*

An increase of the contact angle with higher flow rates can be seen, as previously explained. At r_{fl} = 4 ml/min and r_{fl} = 5 ml/min the contact angle at the centre of the sample rises in a linear fashion according to the findings about the dynamic SIPGP. In contrast, the contact angle at positions at 0.0 cm and 1.0 cm is not increasing between r_{fl} = 3 ml/min and r_{fl} = 5 ml/min. This means that the effect that was described previously by using the COMSOL calculations starts to show its effect starting at r_{fl} = 4 ml/min. Note that the sample area of the coated samples is 1 cm² and the drops of the contact angle device have a certain area, too. This means that the described effect could have an effect with lower flowrates, too but on a scale that cannot be measured in this setup.

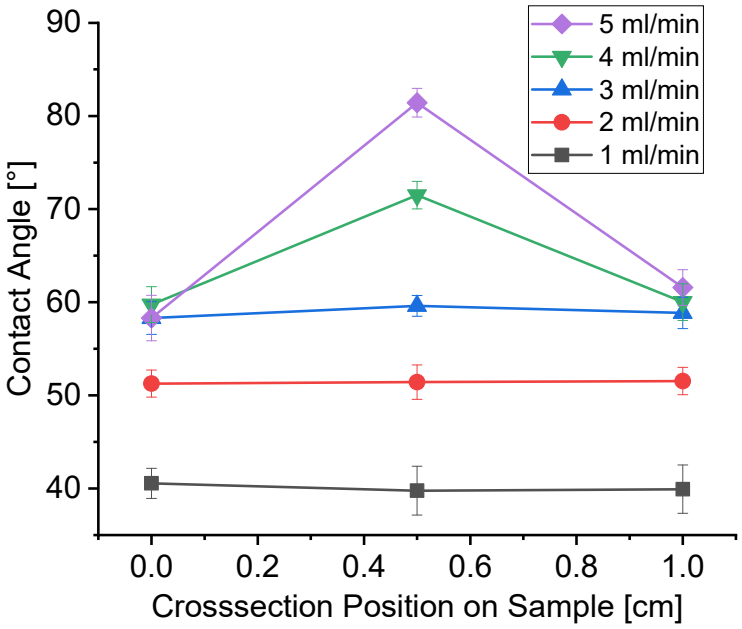

Figure 35: *Contact Angle measured on the left side, the right side and the middle of the P(HEMA-co-MEDSAH) coated P(VDF-TrFE-CTFE) film. Measurement at a flow rate of 1 ml/min to 5 ml/min.*

These experiments show that a higher flow rate can lead to a more inhomogeneous coating. A way to lower this effect could be to use a reactor with a wider flow channel or to use a flow as low as possible.

To further examine the changes a constant flow adds to the reaction, the temperature inside the reactor was measured.

4.3.3 Influence of Temperature

To measure the temperature inside the reactor during the reaction, the inlet and outlet for the argon supply was used to insert the temperature probe (red and yellow wires) (Figure 36 B). To keep the probe in place during the measurement it is first placed behind the wall and is then threaded through one of the gaps in the bottom of the wall. This way the temperature probe is fixated right behind the sample. The whole setup

then included the syringe pump (Figure 36 A1), the temperature measurement device (Figure 36 A2) and the prepared reactor (Figure 36 A3).

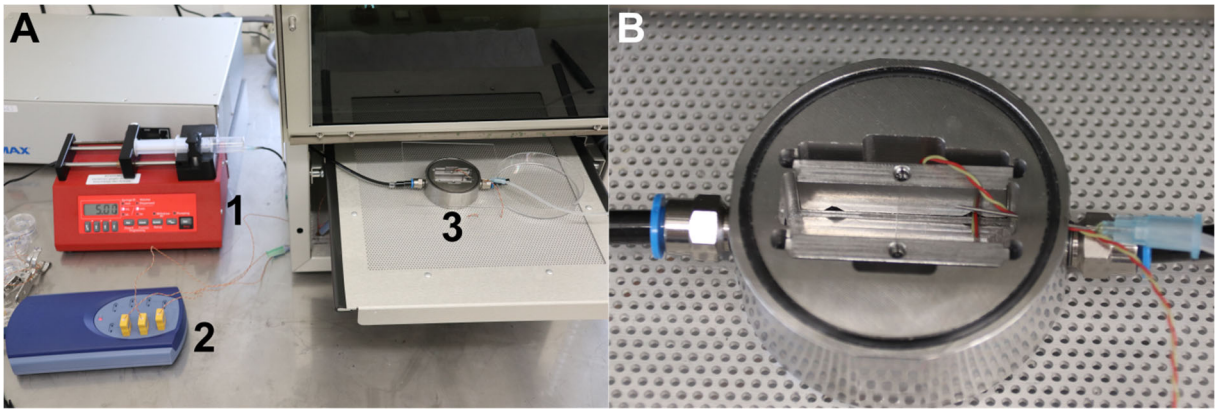

Figure 36: *Full setup of dynamic SIPGP including temperature measurements (A) with the syringe pump (1), the temperature measurement device (2) and the prepared reactor (3) and a close-up of the prepared reactor (B).*

Three measurements were performed with r_{fl} = 0-5 ml/min (Figure 37). The temperature at t_i = 0 s (T_0) was 24 °C in all the measurements with only small fluctuations. The starting temperature is not only dependant on the room temperature, but also on the average temperature of the UV-chamber with a heat producing lamp. The temperature after t_i = 60 s (T_t) was found to be 37 °C with r_{fl} = 0 ml/min, which is equivalent to static SIPGP. With applying a constant flow of monomer solution to the system T_t is decreasing to around 32 °C. The UV lamp is not the only possible reason for the heat development of the solution. The radical polymerization here is an exothermal reaction, which can produce heat to an amount that is measured here, as Dušička *et al.* showed for acrylic acid in propionic acid.[283]

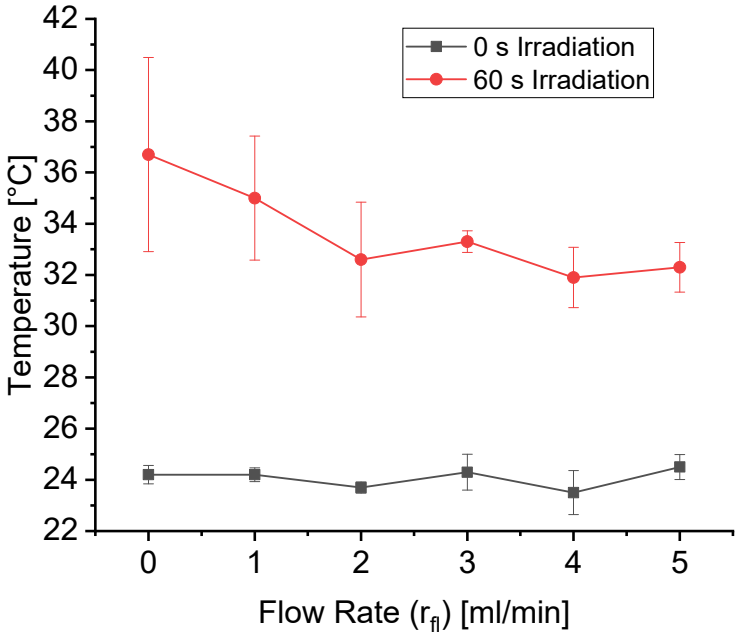

Figure 37: *Temperature measurement during the reaction right behind the sample. Every data point is the average of three measurements at the start (grey, t_i = 0 s, T_0) and end (red, t_i = 60 s, T_t) temperatures of every reaction.*

For an easier comparison Figure 38 shows the warming (T_t-T_0) of the monomer solution during the reaction being the temperature difference between t_i = 0 s and t_i = 60 s. A fast decrease of the warming can be observed between r_{fl} = 0 ml/min and r_{fl} = 2 ml/min. Between r_{fl} = 2 ml/min and r_{fl} = 5 ml/min the decrease of the warming is still present, but weaker than before. This matches the expectations, because the flow provides a constant supply of non-heated monomer solution, while the "old" heated solution gets flushed out. By applying higher flow rates the T_t is supposed to approach T_0 asymptotically. This leads to an in theory quadratically decreasing warming with higher flow rates. The decreasing temperature is a factor that slows down the speed of the reaction. One additional factor for the reaction speed is the decreasing viscosity. The viscosity of the HEMA/MEDSAH monomer solution at 37 °C is 1.80 mPas, while being 2.25 mPas at 32 °C. These changes in temperature and viscosity are one factor that lowers the contact angles with higher flow rates (as previously shown in Figure ***33***).

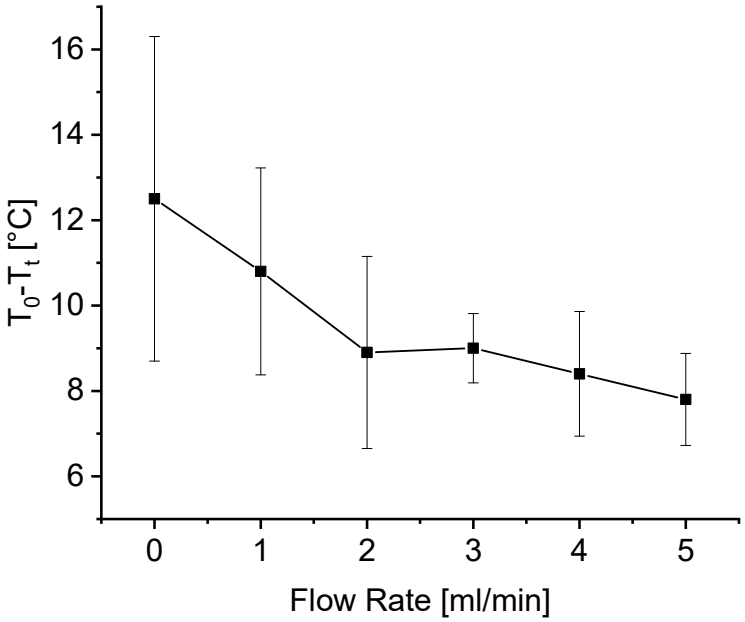

Figure 38: *Warming during the reaction being the difference between start and end temperatures from Figure 37.*

A change in temperature can also change the copolymerization behaviour of the monomers. This was reported for HEMA with comonomers such as MMA or MA within temperatures between 50 °C and 90 °C. The reactivity ratio of HEMA can double (MMA) or even triple (MA) within this temperature range depending on the monomer. The temperature dependence of radical copolymerization was reported for a variety of monomers within the temperature range of 40 °C and 130 °C.[284–286] This shows that a reduction of the temperature change during the polymerization is desirable for a better control over the reaction.

Besides changing the reaction speed of SIPGP, the dynamic performance of this mechanism provides another advantage, which is even more important if a homogeneous coating is the goal to achieve: The reduction of the formation of bulk polymer during the reaction. The following chapter provides more insight to that topic.

4.3.4 Reduction of bulk polymer

During static SIPGP, as explained earlier, not only the coating grafted from the surface is being polymerized, but also polymer inside the monomer solution. This formed polymer can attach to the surface through for example termination reactions between the grafted coating and bulk polymer in the solution. Also not chemically cross-linked polymer can adhere the surface and can then be linked through photochemical reactions to the coating. Both of these phenomena lead to an inhomogeneous coating by the formation of “clumps” of polymer on the surface.

Dynamic SIPGP can prevent the formation of these “clumps” by flushing out the formed bulk with the monomer solution. The difference between dynamic and static SIPGP, while the other parameters remain constant (400 W lamp, t_i = 60 s, d_{ls} = 5 cm), were examined using SEM (Figure 39) (more details in chapter 7.3.9). The pristine P(VDF-TrFE-CTFE) film (Figure 39 A, B) shows small “worms” on the surface of the film as a predominant topology (Figure 39 A). The P(VDF-TrFE-CTFE) film coated with P(HEMA-co-MEDSAH) under static conditions (r_{fl} = 0 ml/min) (Figure 39 C, D) shows, that the previously mentioned “clumps” are not just a single phenomenon, but they can be found in many locations at the surface and create an inhomogeneous coating. The P(VDF-TrFE-CTFE) film coated with P(HEMA-co-MEDSAH) under dynamic conditions (r_{fl} = 2 ml/min) (Figure 39 E, F) in contrast, does not show “clumps” of bulk polymer on the sample, but instead shows a smooth surface with only small irregularities. The coating shows some spots, which are not coated so far (where the structure of the pristine film can be observed), but as described previously in chapter 4.3.2, the coating procedure is slower under dynamic conditions than under static conditions. These images show, that a formation of the bulk polymer on top of the surface can be prevented by applying a constant monomer flow to the system.

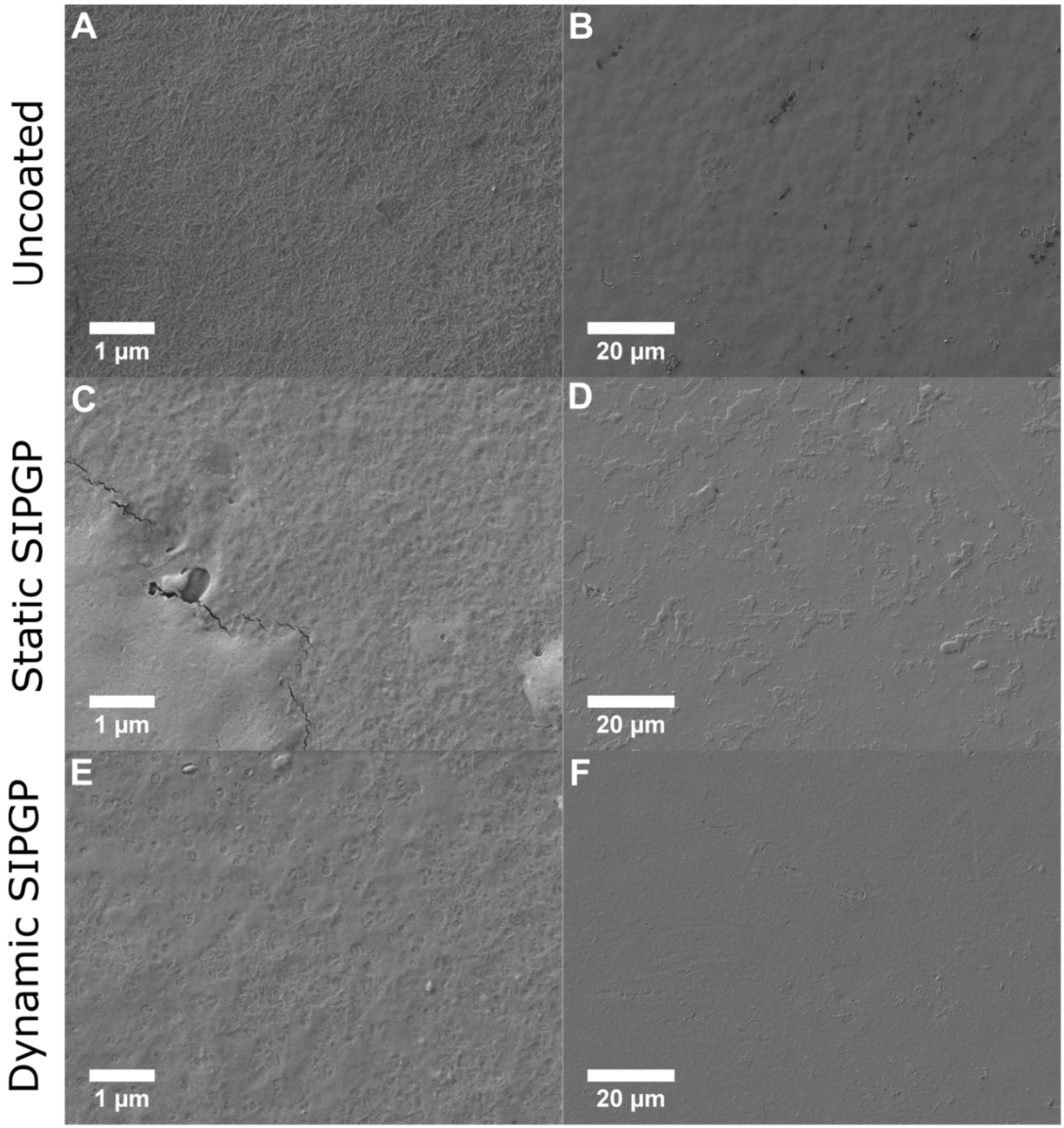

Figure 39: *SEM images of P(VDF-TrFE-CTFE) films coated with P(HEMA-co-MEDSAH). Images of an uncoated film (A, B), of a film coated under static conditions (0 ml/min) (C, D) and of a film coated under dynamic conditions (2 ml/min) (E, F).*

The bulk polymer, which formed inside the solution, could even be observed with the naked eye. To show this, a series of r_{fl} = 1-5 ml/min was performed. After the reaction the silica glass, the walls and the samples were removed. Than 5 ml of distilled water were added to the solution (Figure 40 A-E). At r_{fl} = 1 ml/min (Figure 40 A) white circular bulk polymer inside the solution can be observed because the bulk polymer becomes

opaque when water is added. It is circular, because it is accumulating around the water jet.

However, the bulk polymer can only be seen with the naked eye at r_{fl} = 1 ml/min. Already by using r_{fl} = 2 ml/min (Figure 40 B) this bulk polymer cannot be observed in this way. Same is true for r_{fl} = 3-5 ml/min (Figure 40 C-E). This shows, that the formation of bulk polymer that can be observed with the naked eye can be reduced drastically by applying a constant flow with r_{fl} = 2 ml/min or higher.

To confirm this visual observation, the solutions of a series of r_{fl} = 0-5 ml/min were taken and filtered with a 50 µm pore size filter. Water was used to flush out all the solution inside the reactor into the filter. Figure 40 F shows the amount of bulk polymer that stayed inside the filter after they were dried at 50 °C until the mass was constant. By using static SIPGP (r_{fl} = 0 ml/min) 195 mg of bulk polymer stayed inside the filter. The mass of bulk polymer inside the filter was drastically reduced to 33 mg at r_{fl} = 2 ml/min and stayed at around this number with higher flow rates. This confirms, the finding that r_{fl} = 2 ml/min can be used to decrease the amount of bulk polymer drastically. However, the pore size of the filter was 50 µm and these results only represents the bulk polymer that stayed in this filter.

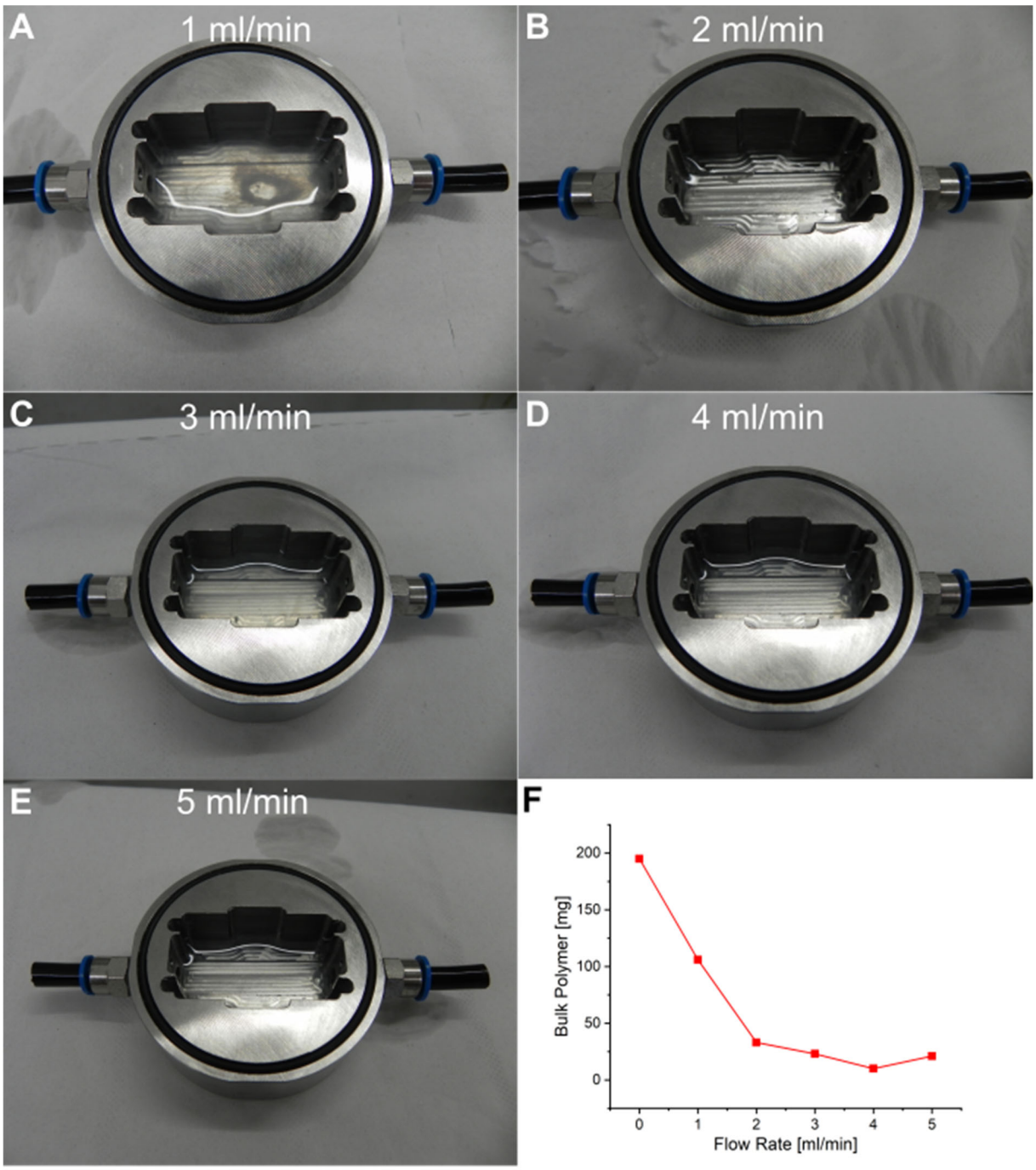

Figure 40: *HEMA/MEDSAH solution after the coating with the flow rates from 1 ml/min to 5 ml/min (A-E). Weight of the P(HEMA-co-MEDSAH) bulk polymer that was left after the solution was filtered with a 50 µm pore size filter (F).*

4.3.5 Conclusion

In the previous chapters dynamic SIPGP was performed and examined. The influence of an applied flow of monomer solution on the contact angle, the heat development, and the bulk polymerization were discovered. Also the theoretical calculations of the flow inside the reactor were verified by an experiment.

It could be stated, that the applied monomer flow can be used to slow down the coating procedure, to decrease heat development inside the monomer solution and to reduce the formation of bulk polymer “clumps” on the surface. This shows, that dynamic SIPGP can add additional control over the procedure compared to static SIPGP. However, the workload per sample is much higher than for static SIPGP and the amount of “wasted” monomer solution is higher.

4.4 SIPGP on Scaffolds

Planar films are predestined to evaluate new procedures with new capabilities of SIPGP. However, for biomedical applications it is more likely to use non-planar substrates. Since these applications are the goal at which this work is aiming, more complex geometries have to be coated and measured as well. MEW printed scaffolds are a good choice here, because they represent a complex geometry and can be produced in medical grade. This chapter investigates the P(HEMA-co-MEDSAH) coating procedure on these scaffolds and the influence of dynamic SIPGP on coating scaffolds.

4.4.1 SIPGP on Scaffolds of PVDF

The PVDF samples used in this chapter were printed via MEW by Juliane Kade at the *Department for Functional Materials and Dentistry* (FMZ) in Würzburg, Germany. The coating procedure was performed as described in chapter 7.3.10. To evaluate the coating, three types of measurement were chosen, stereomicroscopy, confocal fluorescence microscopy and scanning electron microscopy (SEM). In order to see the difference between static and dynamic SIPGP, pristine samples, coated sample with r_{fl} = 0 ml/min and with r_{fl} = 2 ml/min were produced under otherwise same conditions (t_i = 60 s, d_{ls} = 5 cm, 400 W UV lamp)

4.4.1.1 Stereomicroscopy

With stereomicroscopy the macroscopic changes made to the surface during the coating can be observed. If the overview images are compared, the pristine scaffold (Figure ***41*** A) and the dynamically coated scaffold (Figure 41 C) do not show differences, whereas the scaffold coated statically shows formation of bulk polymer in between the fibres (Figure 41 B red arrows). A closer look at the images reveals

something else. It can be observed, that on top of the fibres of the statically and dynamically coated samples, lengthwise cracks appear (Figure 41 E, F black arrows), which cannot be found on top of the pristine sample (Figure 41 D) in addition the statically coated sample (Figure 41 E) shows a polymer strand between two fibres as well as a “webbing” called bulk polymer in the top right corner of the fibre crossing in the middle of the image.

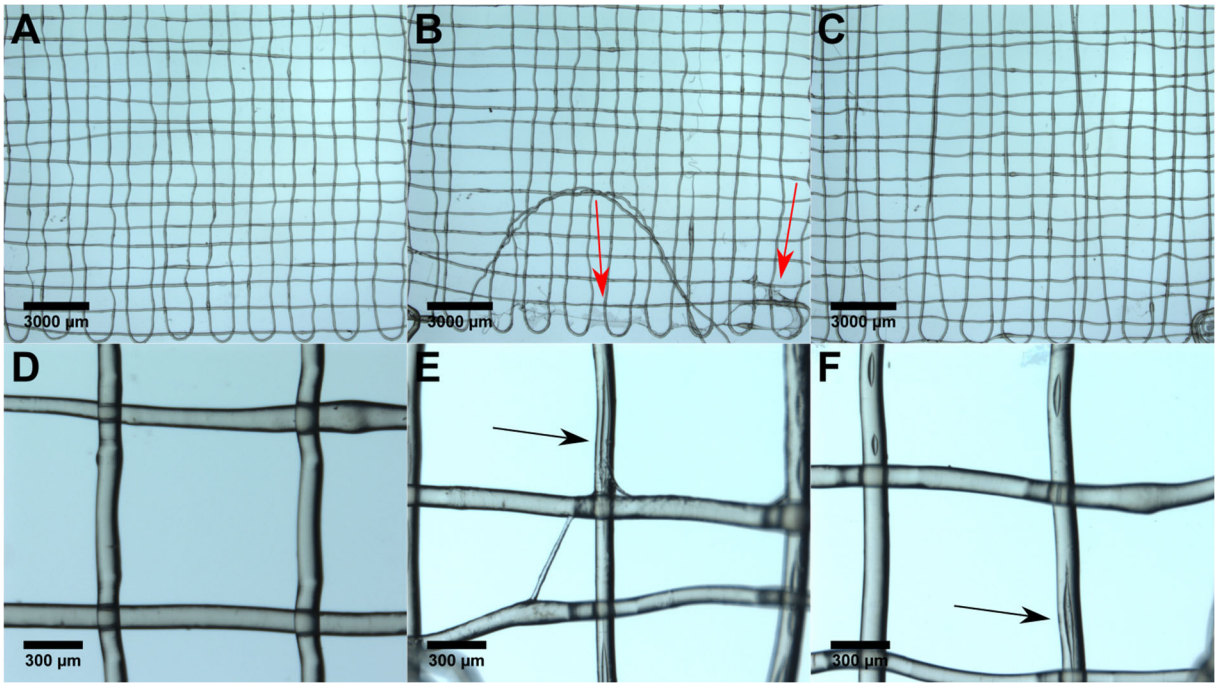

Figure 41: *Stereo microscope images of P(HEMA-co-MEDSAH) coated MEW printed PVDF scaffolds. Pristine PVDF scaffold (A, D), scaffold coated via static SIPGP (flow rate: 0 ml/min) with the red arrows marking the “webbing” (B, E) and scaffold coated via dynamic SIPGP (flow rate: 2 ml/min) (C, F).*

The cracks that were observed on the coated fibres are cracks in the coating. Since the coating is a hydrogel and gets formed in swollen state in an aqueous environment, it starts shrinking when dried. This shrinking of a coating that surrounds the fibre then causes cracks. This also indicates, that applying a constant monomer flow to the system leads to a coating, as it does without, but can prevent bulk polymer from forming in between the fibres. To support these findings, fluorescence microscopy was utilized.

4.4.1.2Fluorescence Microscopy

Sodium fluorescein was chosen as a dye for confocal fluorescence microscopy, because it is soluble in water and is non-hazardous. The samples were immersed in a $3x10^{-4}$ M aqueous fluorescein sodium solution. Since the P(HEMA-co-MEDSAH) coating is a hydrogel, is does not only absorb water from the environment, but also the fluorescence dye with it (for details on the dying procedure see chapter 7.3.6). The samples were then washed with water in order to remove dye adhered to the surface of the samples.

A pristine sample (Figure 42 A), a dynamically coated (r_{fl} = 2 ml/min) sample (Figure ***42*** B), and a statically (r_{fl} = 0 ml/min) coated sample (Figure 42 C, D) were measured. All samples were measured with the exact same settings of the device. The uncoated scaffold (Figure 42 A) does show a weak fluorescence, while the dynamically coated sample (Figure 42 B) shows strong fluorescence, which is homogenously distributed along the fibres. The statically coated sample (Figure 42 C) in contrast shows bulk polymer in the form of strong webbing inside of a hatch of the scaffold (this hatch can be found in the bottom right corner of Figure 41(B). Additionally, there are black spots on top of the fibres. A different spot in the statically coated sample (Figure ***42*** D) shows something that could already be observed in stereomicroscope images. There are cracks along the fibres, which occur caused by the shrinking of the hydrogel coating.

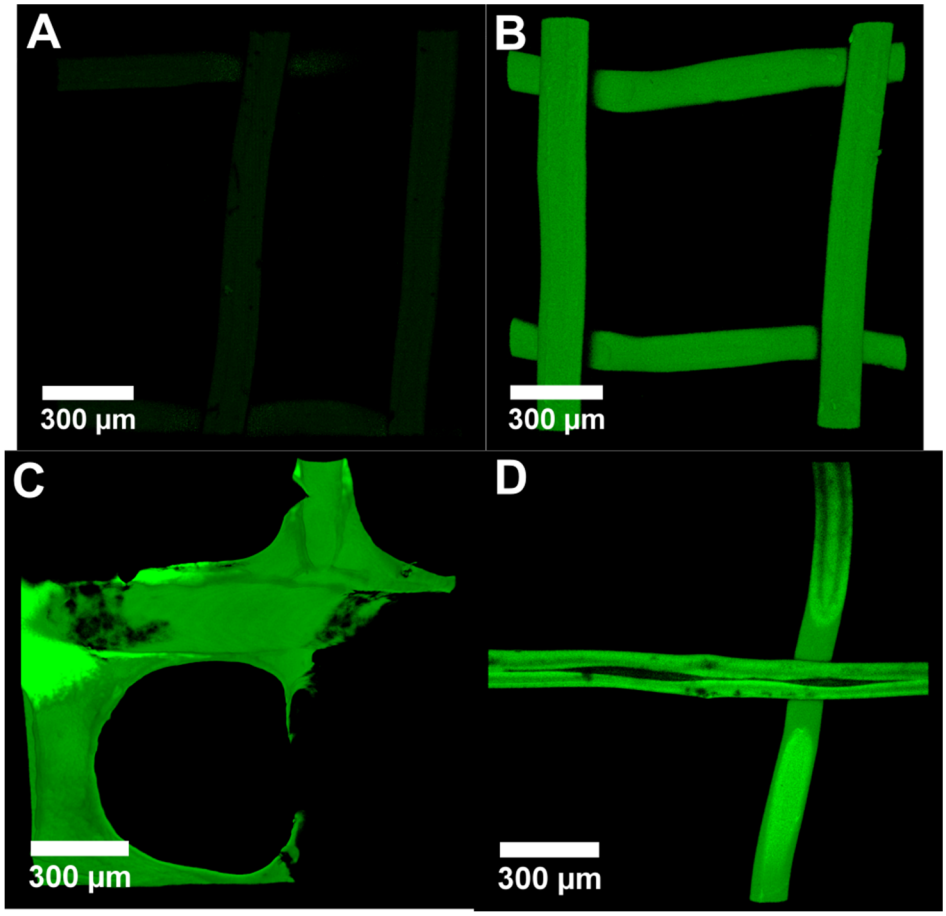

Figure 42: *Fluorescence images using the fluorescence dye fluorescein sodium. Image of a pristine MEW printed PVDF sample (A), of a sample coated with P(HEMA-co-MEDSAH) via dynamic SIPGP (flow rate: 2 ml/min) (B) and of a statically coated sample (flow rate 0 ml/min) (C, D).*

The confocal fluorescence microscope images validate the findings, which could be made with the stereomicroscope images. The pristine scaffold (Figure 42 A) only shows very weak fluorescence. This fluorescence could be adhered dye on the surface, which could not be removed by immersing the samples in water. The dynamically coated sample (Figure 42 B) shows much stronger fluorescence, than the pristine sample does, which verifies the presence of a hydrogel coating. The statically coated sample (Figure 42 C) shows the phenomenon of “webbing” pretty clearly, which does not occur with the dynamically coated sample and shows the necessity of dynamic SIPGP, if this bulk polymer formation is undesired. Also the black spots that can be observed indicate an inhomogeneous coating via static SIPGP and a more homogenous coating with dynamic SIPGP (Figure 42 B) indicates by showing a homogenous fluorescence on the fibres. However, to investigate the topology, scanning electron microscopy must be utilized, as done in the following chapter.

4.4.1.3 Scanning Electron Microscopy

The information, which the previous measurement methods cannot provide is the topology of the coating, which can be done by scanning electron microscopy.

To provide this, images of a pristine MEW printed PVDF scaffold (Figure 43 A, D, G), a statically (r_{fl} = 0 ml/min) coated scaffold (Figure 43 B, E, H) and a dynamically (r_{fl} = 2 ml/min) coated scaffold (Figure 43 C, F, I) were taken. The overview images (Figure 43 A-C) do not show a difference between the uncoated (Figure 43 A) and the dynamically coated (Figure 43 C) sample, while the statically coated sample (Figure ***43*** B) shows “webbing”. A closer look at the fibres (Figure 43 D-F), where the statically coated sample (Figure 43 E) shows “webbing”, the dynamically coated sample (Figure 43 F) now shows in contrast to the pristine scaffold (Figure 43 D) some irregularities on the surface and also a small strand of polymer between the two shown fibres (Figure 43 F red arrow), while the pristine scaffold (Figure 43 D) does not. To further investigate this, a closer look on the topology of the fibres (Figure 43 G-I) is needed. It can be observed, that the surface structure of the pristine scaffold (Figure ***43*** G), is not smooth, but has some furrows. The statically coated sample (Figure 43 H) as well as the dynamically coated sample (Figure 43 I) both show the same structure on the surface, which does not show these furrows, but a smooth surface.

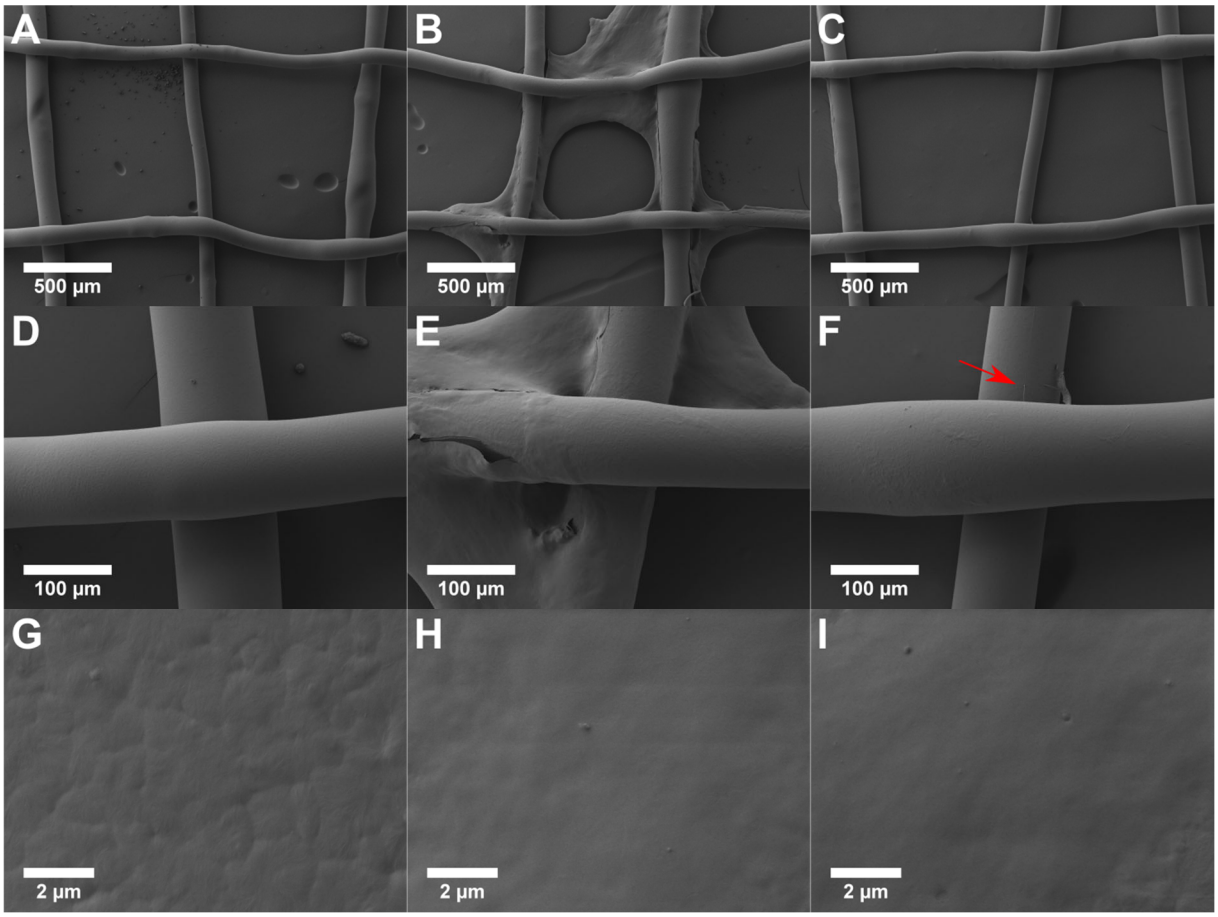

Figure 43: *SEM images of MEW printed PVDF scaffolds: pristine scaffolds (A, D, G), statically (flow rate: 0 ml/min) P(HEMA-co-MEDSAH) coated scaffolds (B,E,H) and a dynamically (flow rate: 2 ml/min) P(HEMA-co-MEDSAH) coated scaffolds (C,F,I).*

These images again show, that a coating via SIPGP can be achieved by utilizing static and dynamic conditions, as the altered structure of the fibre surface shows. One image of the dynamically coated sample (Figure 43 F) shows that the formation of bulk polymer strands cannot be prevented for 100 % by applying a monomer flow with r_{fl} = 2 ml/min. Nevertheless the formation of bulk polymer attached to the surface can be drastically reduced by utilizing dynamic SIPGP.

4.4.2 SIPGP on Scaffolds of P(VDF-TrFE)

The P(VDF-TrFE) samples used in this chapter were printed via MEW by Juliane Kade at the *Department for Functional Materials and Dentistry* (FMZ) in Würzburg, Germany. The coating procedure was performed as described in chapter 7.3.10. Stereo microscopy, confocal fluorescence microscopy and scanning electron microscopy will be utilized to show differences in the coating of P(VDF-TrFE) scaffolds between static SIPGP (r_{fl} = 0 ml/min) and dynamic SIPGP (r_{fl} = 2 ml/min) in the following chapters.

4.4.2.1 Stereomicroscopy

As previously described with the PVDF samples, stereo microscopy provides a first view of the macroscopic changes after the coating. Overview images (Figure 44 A-C) and close ups (Figure 44 D-F) of a pristine scaffold, a statically coated scaffold and a dynamically coated scaffold were examined.

The first thing that is striking is, that the statically coated scaffold (Figure 44 B) kept its shape, while the dynamically coated scaffold (Figure 44 C) did not and the pristine scaffold (Figure 44 A) is even damaged during the handling of the measurements. The close ups then show, that there is no visible difference between the dynamically coated scaffold (Figure 44 F) and the pristine scaffold (Figure 44 D). However the statically coated scaffold (Figure 44 E) shows bulk polymer, which has formed between the fibres.

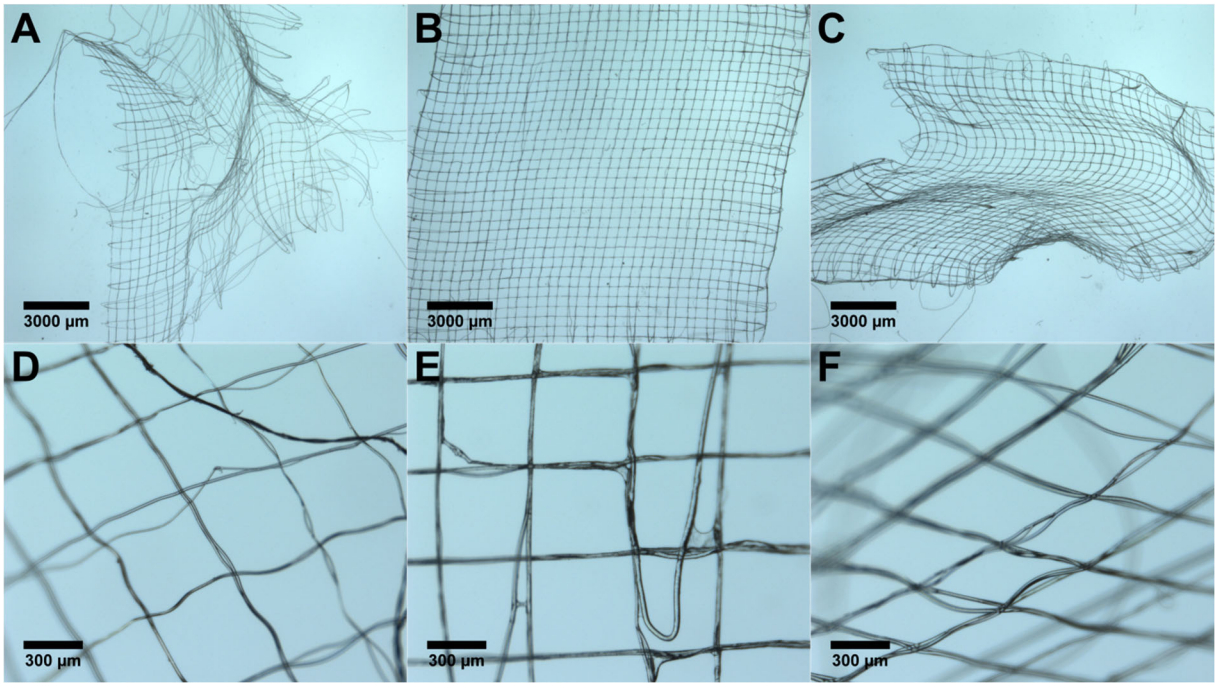

Figure 44: *Stereo microscope images of P(HEMA-co-MEDSAH) coated MEW printed P(VDF-TrFE) scaffolds. Pristine P(VDF-TrFE) scaffold (A, D), scaffold coated via static SIPGP (flow rate: 0 ml/min) (B, E) and scaffold coated via dynamic SIPGP (flow rate: 2 ml/min) (C, F).*

The handling of these samples is very difficult, because the fibres are very thin and they are only attached to each other very weakly, so it's easy to damage them as soon as they are removed from the glass plate they were printed on. After coating however, the samples were much easier to handle without damaging them. The reason for that is the formed connection between the fibres through the coating. The overview images (Figure 44 A-C) represent that perfectly, because statically coated samples are easy to handle, because they do not only provide connections between the fibres on a microscopic level, but also, macroscopic links through the bulk polymer (Figure 44 E). The dynamically coated samples are easier to handle then the pristine samples, because they provide more stability through the coating, but they do not have the macroscopic bulk polymer to strengthen the links between the fibres, as the statically coated samples do.

4.4.2.2 Confocal Fluorescence Microscopy

Sodium fluorescein was chosen as a dye for confocal fluorescence microscopy, and treated as described in chapter 4.4.1.2 (for details on the dying procedure see chapter 7.3.6).

The pristine scaffold (Figure 45 A) shows weak fluorescence (the images were all done with the same settings), while the coated samples show much stronger fluorescence. The dynamically coated sample (Figure 45 B) shows a fluorescence, which is distributed homogenously over the scaffold, while the statically coated sample (Figure ***45*** C, D) shows many dark spots on the fibres. In Figure 45 C they can best be spotted in the top left corner, while in Figure 45 D there are big uncoated spots distributed over the fibres.

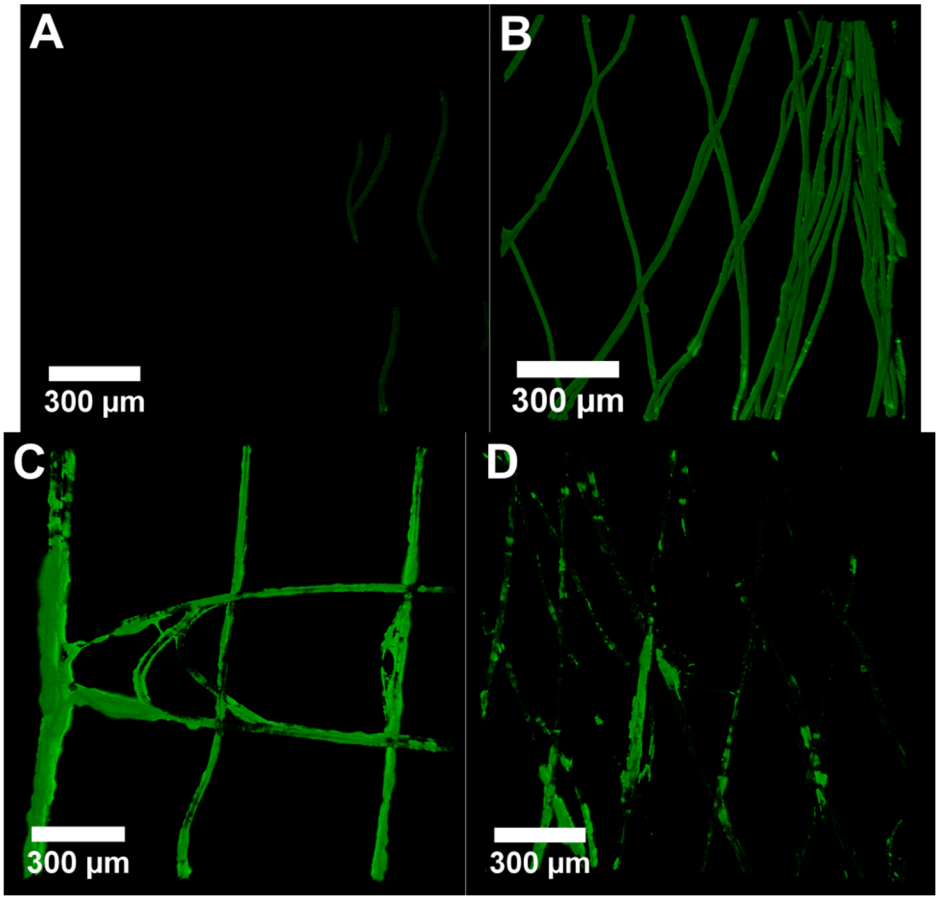

Figure 45: *Fluorescence images using the fluorescence dye fluorescein sodium. Image of a pristine MEW printed P(VDF-TrFE) scaffold (A), a scaffold coated with P(HEMA-co-MEDSAH) via dynamic SIPGP (flow rate: 2 ml/min) (B) and of a statically coated scaffold (flow rate 0 ml/min) (C, D).*

The fluorescence that the pristine scaffold (Figure 45 A) shows, probably results from fluorescein sodium that is adhered to the surface of the fibres and was not removed by immersing the sample in water. The dynamically coated sample (Figure 45 B) indicates, that the coating homogeneity of dynamic SIPGP is much higher, then the homogeneity of static SIPGP (Figure 45 C, D). The dark, and therefore uncoated, spots can be found all over the statically coated sample, while they cannot be found on the dynamically coated sample.

4.4.2.3 Scanning Electron Microscopy

SEM can provide an even closer look on the sample by depicting the topology of the samples. The overviews of the sample (Figure 46 A-C) do not show a big difference amongst each other, while the close ups (Figure 46 D-F) show, that the statically coated sample (Figure 46 E) shows bulk polymer that links two of the fibres, while there are also spots of uncoated fibre, that has the same surface structure as the pristine fibre (Figure 46 E, red arrows). The statically coated fibre (Figure 46 F) shows a difference to the pristine fibre (Figure 46 D), but the topology of the pristine fibre can be recognized in weakened form. On the surface of the pristine fibre fibrils can be observed (Figure 46 G), that result from crystallization and solidification processes after the printing.[10] The statically coated fibre (Figure 46 H) instead shows a smoothened surface, which can be observed on the dynamically coated fibre (Figure 46 I) as well.

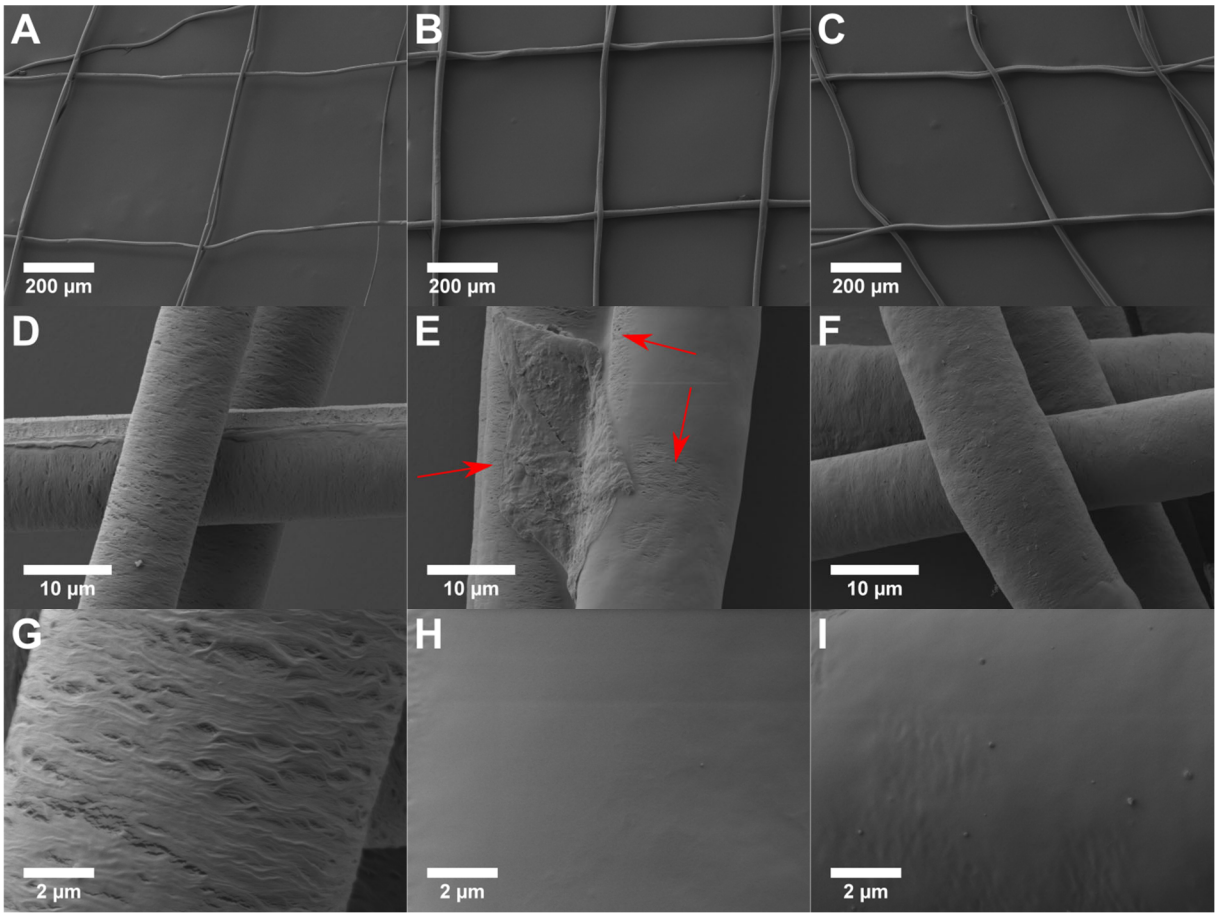

Figure 46: *SEM images of a pristine MEW printed P(VDF-TrFE) sample (A, D, G), a P(HEMA-co-MEDSAH) statically (flow rate: 0 ml/min) coated sample with red arrows marking uncoated spots (B,E,H) and a dynamically coated sample (C,F,I).*

The overview image of the statically coated fibre (Figure 46 B) was chosen here, because it shows, that the bulk polymer is not present all over the sample, but occurs in various locations (as previously shown in Figure 44 E). Figure 46 E clearly shows the disadvantages static SIPGP has. There is bulk polymer, which is attached to the fibres and next to it a spot, which is not coated at all. These two disadvantages can be dealt with by applying a constant monomer flow (Figure 46 F). The topology of the pristine scaffold (Figure 46 G), which exhibits a lot of cracks and irregularities can be covered by coating via SIPGP (Figure 46 H, I).

4.4.3 SIPGP on Scaffolds of PCL

The scaffolds used in this chapter were printed by Ezgi Bakirci at the *Department for Functional Materials and Dentistry* (FMZ) in Würzburg, Germany as described in chapter 7.3.10. PCL is the material, which is up to this point the “gold standard” for MEW printing and can be produced as medical grade scaffolds. Not only can MEW scaffolds be printed faster than PVDF or P(VDF-TrFE), PCL can be printed with much thinner fibres, smaller hatch spacing and more layers. The following chapters evaluate the static and dynamic SIPGP on these PCL scaffolds.

4.4.3.1 Stereomicroscopy

The samples presented here are a pristine scaffold, one that was coated via static SIPGP (r_{fl} = 0 ml/min) and one that was coated via dynamic SIPGP (r_{fl} = 2 ml/min).

When the pristine scaffold (Figure 47 A) is compared to the dynamically coated scaffold (Figure 47 C) in the overview, no difference can be spotted, other that the darker corners of the statically coated sample (Figure 47 C), which result from a slightly damaged scaffold through pressure. The statically coated scaffold (Figure 47 B) however, shows strong “webbing” of bulk polymer all over the sample (darker hatches in the image). This can also be observed with higher magnification. There the pristine scaffold (Figure ***47*** D) and the dynamically coated scaffold (Figure 47 C) do not show much difference, but on the statically coated sample (Figure 47 E) the bulk polymer inside the hatches can be observed.

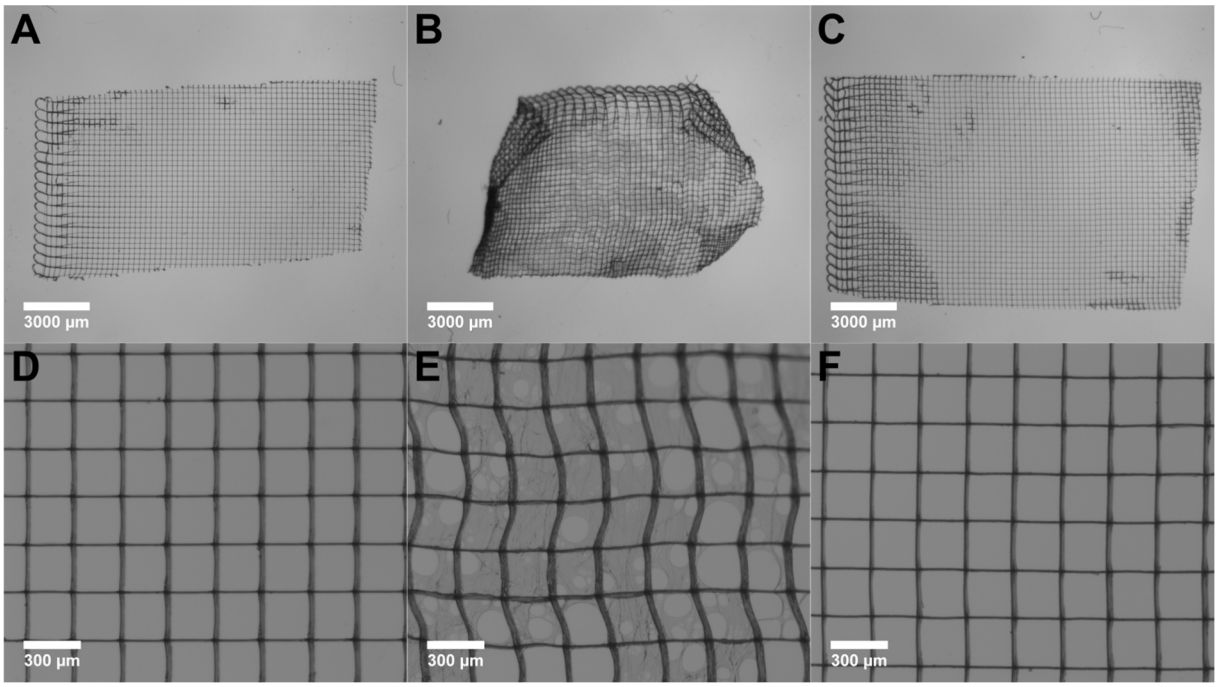

Figure 47: *Stereo microscope images of P(HEMA-co-MEDSAH) coated MEW printed PCL scaffolds. Pristine PCL scaffold (A, D), scaffold coated via static SIPGP (flow rate: 0 ml/min) (B, E) and a scaffold coated via dynamic SIPGP (flow rate: 2 ml/min) (C, F).*

Compared to the statically coated scaffolds of PVDF and P(VDF-TrFE) in the previous chapters, there is much more bulk polymer forming inside the hatches of the PCL scaffolds. The biggest difference between those scaffolds is the hatch spacing. While the PCL scaffolds were produced with a hatch spacing of 250 µm, the hatch spacing of PVDF was 1000 µm and of P(VDF-TrFE) 500 µm. This indicates, that smaller hatch spacing leads to an increased formation of bulk polymer inside the hatches when using static SIPGP. The bulk polymer, that has formed inside the monomer solution can easier attach to a smaller hatch spacing, because with a smaller hatch spacing there is more surface to attach and react with than with bigger hatch spacing. However, the “webbing” inside of the hatches is not homogeneous. Some hatches are completely “filled” with bulk polymer, others do not show webbing and most hatches show something in between. This instance makes it more interesting though, that by applying a constant monomer flow this webbing can be prevented. However, for a better insight of the coating, fluorescence microscopy must be utilized.

4.4.3.2 Fluorescence Microscopy

Sodium fluorescein was chosen as a dye for confocal fluorescence microscopy, and treated as described in chapter 4.4.1.2 (for details on the dying procedure see chapter 7.3.6).

The pristine scaffold (Figure 48 A) does not show any fluorescence at all, while the dynamically coated scaffold (Figure 48 C) shows fluorescence at the fibres. The statically coated sample (Figure 48 B) shows not only fluorescence on the fibres, but also inside the hatches.

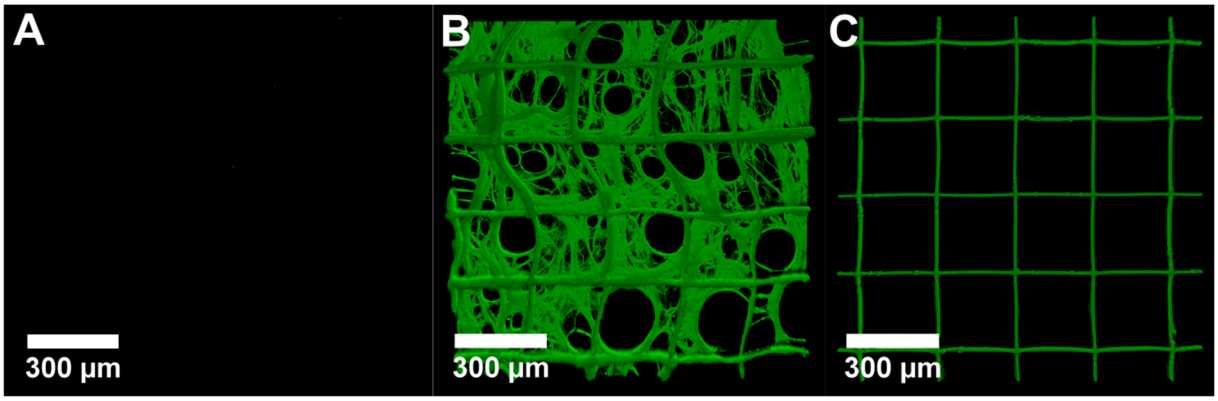

Figure 48: *Fluorescence images using the fluorescence dye fluorescein sodium. Image of a pristine MEW printed PCL scaffold (A), a scaffold coated with P(HEMA-co-MEDSAH) via static SIPGP (flow rate: 0 ml/min) (B) and of a dynamically coated scaffold (flow rate 2 ml/min) (C).*

The comparison between the pristine scaffold (Figure 48 A) and the dynamically coated scaffold (Figure 48 C) clearly shows the presence of a coating on top of the fibres. Additionally, there are no dark spots visible, which indicates a homogeneous coating over the fibres without the “webbing” that is predominant at the statically coated scaffold (Figure 48 B). This confirms the findings made in the previous chapter and also shows, that though not having macroscopically visible polymer, the sample coated via dynamic SIPGP is coated with P(HEMA-co-MEDSAH).

4.4.3.3 Scanning Electron Microscopy

Finally, the SEM can provide more information about the topology of the coated fibres. To do so an overview of the scaffolds (Figure 49 A-C), a close up on a crossing point (Figure 49 D-F) and images of the fibre surface (Figure 49 G-I) were taken.

As already described for the stereomicroscope images, the overview does not show differences between the dynamically coated scaffold (Figure 49 C) and the pristine scaffold (Figure 49 A). However, a huge amount of “webbing” can be observed when looking at the statically coated scaffold (Figure 49 B). The view on the crossing point however, already shows a slight difference between the dynamically coated scaffold (Figure 49 F) and the pristine scaffold (Figure 49 D), because a smooth structure can be observed at the surface of the fibres, which is even stronger at the fibres of the statically coated scaffold (Figure 49 E). These smooth structures, can be observed better when looking closely on the surface of the dynamically coated scaffold (Figure ***49*** I). The pristine scaffold instead, shows a more flat structure including small holes in the surface. The statically coated surface shows a combination of both, at some spots the smooth structure can be observed and on others the flat hole containing surface.

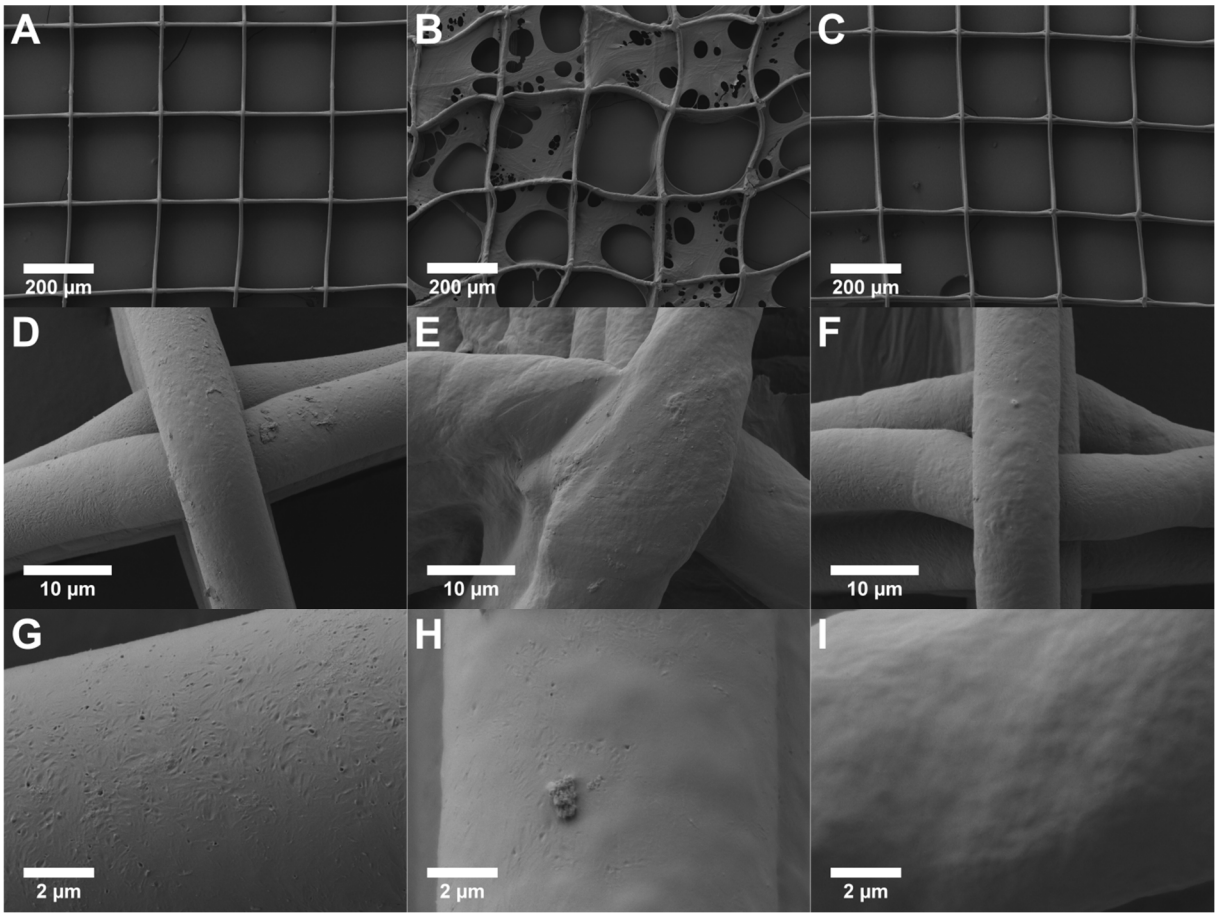

Figure 49: *SEM images of a pristine MEW printed PVDF sample (A, D, G), a P(HEMA-co-MEDSAH) statically (flow rate: 0 ml/min) coated sample (B,E,H) and a dynamically coated sample (C,F,I).*

The smooth structure is the structure the coating is forming. This shows that under static and dynamic conditions a coating can be achieved. However, the coating formed under static conditions shows irregularities in the coating in the form of spots that are not coated, which supports the findings of coating PVDF and P(VDF-TrFE) scaffolds. The overview definitely supports this, because the “webbing” that is occurring on the statically coated scaffold (Figure 49 B) is predominant, while not present on the dynamically coated fibre (Figure 49 C), at all.

This shows, that by applying a constant monomer flow to the system while coating scaffolds, the formation of “webbing” bulk polymer can be prevented by flushing out formed bulk polymer inside the solution.

4.4.4 SIPGP on Functionalized Silica Fibres

The fleeces used in this chapter were produced by Dr. Bastian Christ at the *Fraunhofer ISC* in Würzburg, Germany, as described in chapter 7.3.10. The fleeces consist of $[SiO_x(EOT)_y(OH)_z]_n$ and they are biodegradeable.[287] They have ethoxy groups on their surface, which means, that they are applicable to SIPGP. To examine this, static SIPGP was performed (dynamic SIPGP was not performed, because this project was not further pursued) on these fleeces to coat them with P(HEMA-co-MEDSAH) as an anti-fouling coating.

4.4.4.1 Stereomicroscopy

First stereomicroscopy was utilized to evaluate the coating on the fibres of the fleeces (Figure 50). To do so, an image of a pristine fleece (Figure 50 A) and images of P(HEMA-co-MEDSAH) coted fleeces (Figure 50 B-D) were taken. The pristine fleece consists of clear, transparent fibres without connections between them. The coated fleeces show connecting strands between the fibres (Figure 50 red circles). Additionally, the fibres are not clear anymore, but have a more turbid surface.

The strands probably consist of bulk P(HEMA-co-MEDSAH), which formed between the fibres. The turbid surface that is present after the coating of the fleeces indicates, that the surface was modified, which means, that the coating via SIPGP was successful.

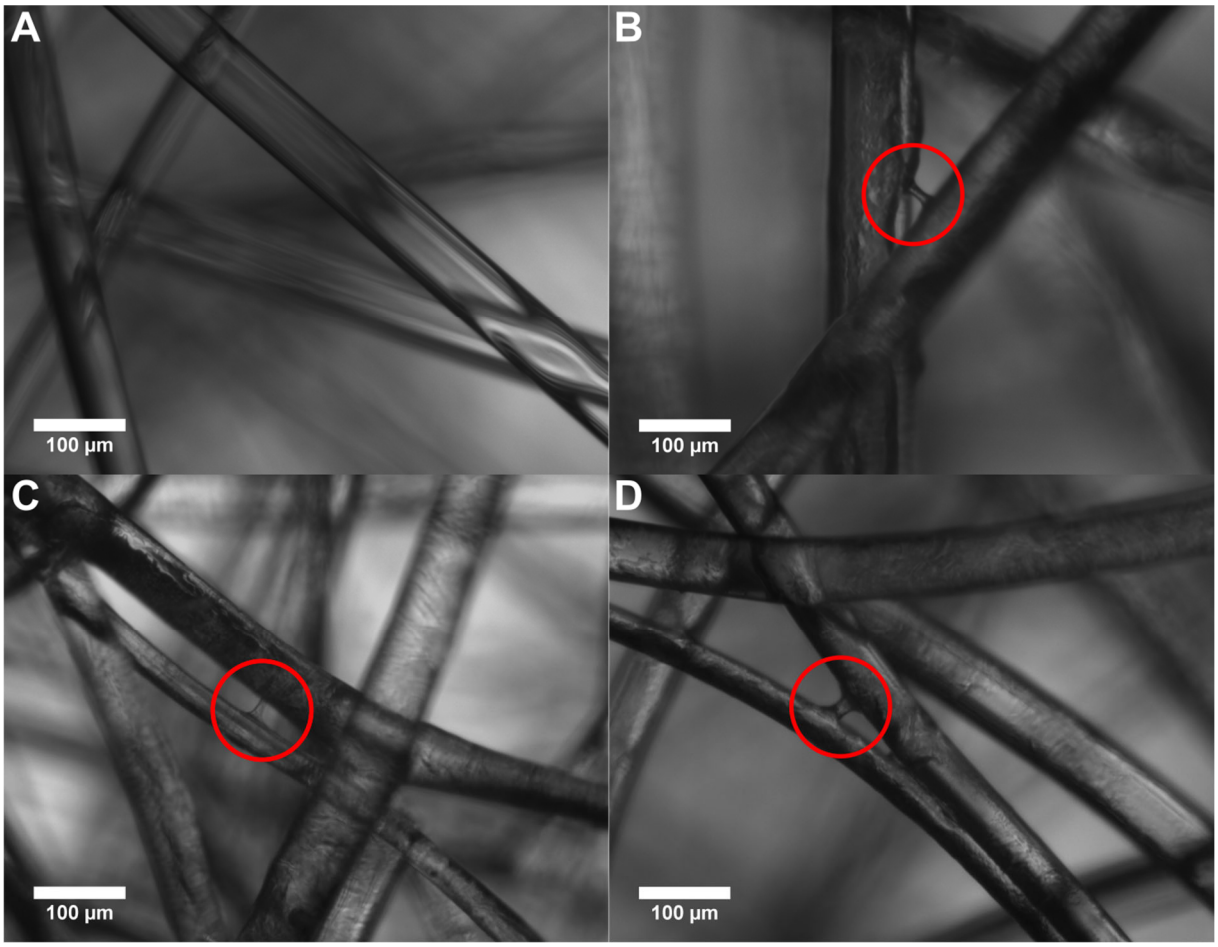

Figure 50: *Stereomicroscope images of pristine modified silica fibres (A) and P(HEMA-co-MEDSAH) coated silica fibres (B-D). The red circles mark a bridging of the coating between fibres.*

To further verify the presence of the coating, SEM images and EDX measurements were performed.

4.4.4.2 Scanning Electron Microscopy / Energy-Dispersive X-Ray Spectroscopy

The SEM provides more detailed information about the surface of the fibres (Figure ***51***). The smooth structure, which was described in the previous chapters, can be observed in the overview (Figure 51 A) and also the links between fibres can be observed with higher magnification (Figure 51 B). At a spot, where a fibre was cracked after the coating, the core of a coated fibre can be observed (Figure 51 C). There a

clear difference in structure between the fibre and the coating can be observed with higher magnification (Figure 51 D).

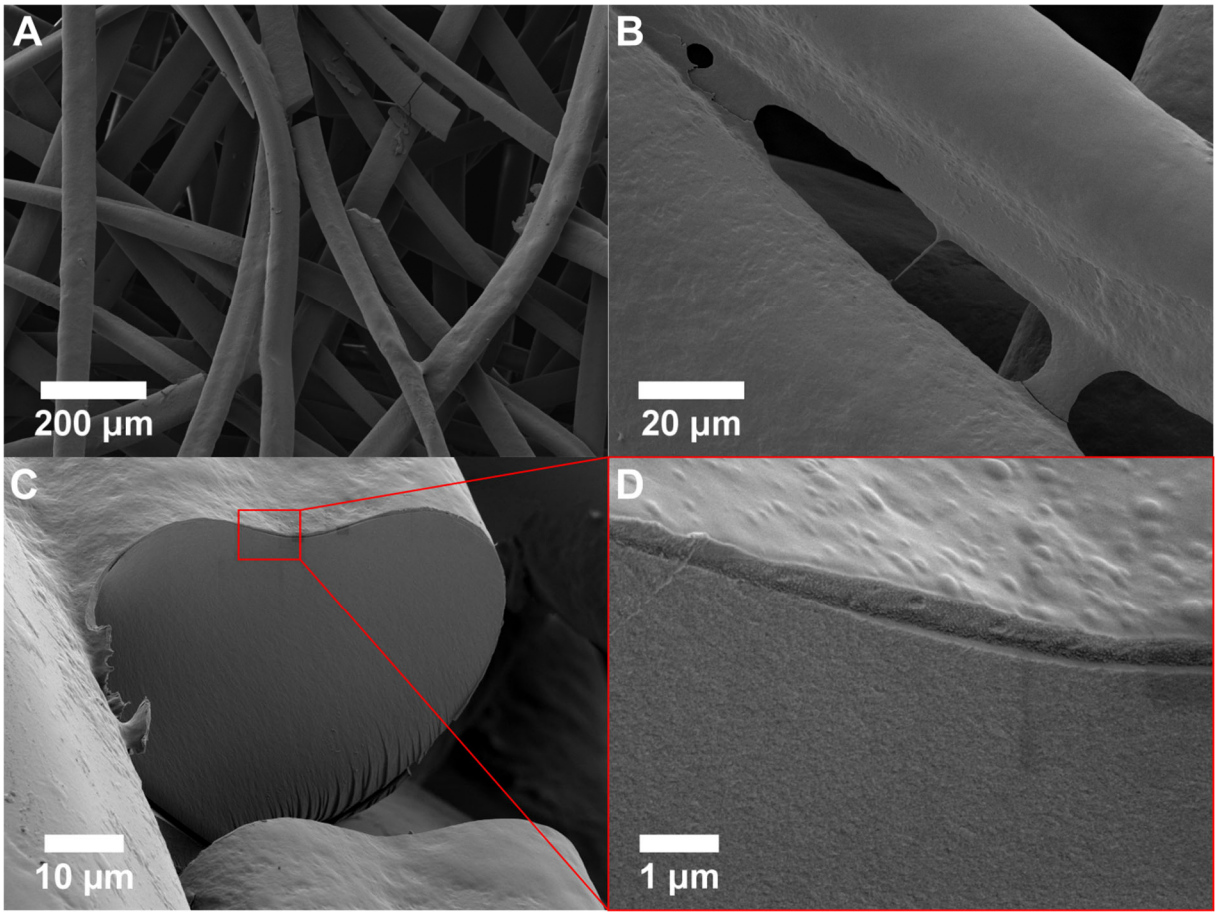

Figure 51: *SEM images of modified electro spun silica fibres that were coated with P(HEMA-co-MED-SAH) providing an overview (A), a close-up (B) and a look at a broken fibre that allows to look at the cross section (C) with the inset (D).*

The overview (Figure 51 A) and the close up (Figure 51 B) confirm the findings from the stereomicroscope image, that there is a coating on the surface with bulk polymer strands, that formed between the fibres. The cross section of the fibre (Figure 51 C, D) shows, the different topology of the coating and the fibre. The coating has the smooth surface, while the fibre shows a plane surface. To show, that these topologies differentiate the coating from the fibre, EDX measurements were performed.

The EDX measurements were performed at a spot, which contains strands between the two fibres as well uncoated and coated fibres (Figure 52 A). The fibre in the top shows mainly uncoated spots, while the lower fibre shows predominantly the smooth

structure. For the EDX measurements Si and C were chosen as the observed elements, because C is an atom that is highly contained by the coating and is only rarely present in the fibre. For Si it's vice versa. It makes a huge portion of the fibre, while not being present in the coating. So these two elements are predestined to distinguish between the fibre and the coating. N was also measured, because it is rarely present in the coating and not present at all in the fibre.

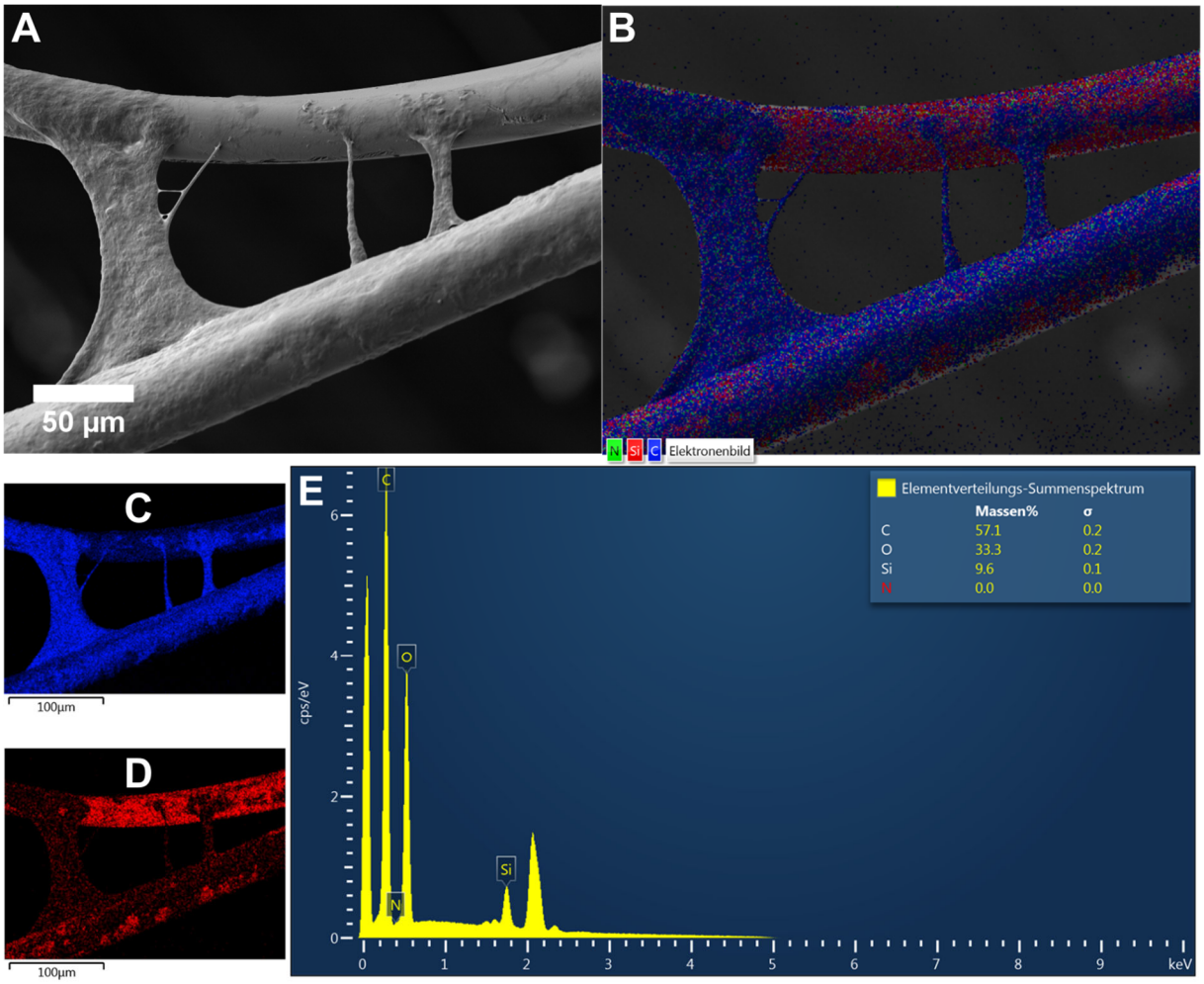

Figure 52: *SEM image of P(HEMA-co-MEDSAH) coated Silica Fibres (A). EDX spectrum of the measured electrons (E), image of the carbon signal (C), image of the silicon signal (D) And an overlay of the silicon, carbon and nitrogen signal (B).*

The overlay of the three measurements (Figure 52 B) clearly shows, that the red colour of Si (Figure 52 D) is dominant on all spots, which show the planar surface in the SEM image (Figure 52 A). The blue colour of C (Figure 52 C) is dominant in all places, where the smooth structure can be observed in the SEM image. The green colour of N is only present as noise. This proofs, that the smooth structure in these SEM images is formed

by the coating, while the plane surface is a property of the pristine modified silicon fibres.

4.4.5 Conclusion

In this chapter static and dynamic SIPGP were performed on MEW printed scaffolds of PVDF, P(VDF-TrFE) and PCL and were compared. Also modified silica fibres were successfully coated via static SIPGP. The most interesting finding was, that by using static SIPGP, bulk polymer is forming in between the fibres, which is called “webbing”. This phenomenon can be prevented by utilizing dynamic SIPGP. Additionally it could be shown, that the homogeneity of the formed coating can be increased by performing dynamic SIPGP compared to static SIPGP.

4.5 Biological properties

As mentioned earlier, SIPGP is a promising technique to be utilized for biomedical applications, since the omission of any initiator or organic solvent during the procedure is possible. The following chapter will evaluate the biological properties of the used P(HEMA-co-MEDSAH) coating, which is supposed to function as an anti-fouling coating, due to the anti-fouling properties of PMEDSAH.[106] Additionally a second coating material, P(HEMA-co-METAC), will be introduced and evaluated for its biological properties.

4.5.1 P(HEMA-co-METAC)

In order to find an appropriate ratio between the two monomers HEMA and METAC, a variety of ratios between those two was polymerized in bulk. The water content in all solutions was 55 wt%. The ratios in the following always are the ratios between HEMA and METAC, while the monomers together always make 45 wt% of the aqueous solution. The bulk polymers were produced as described in chapter 7.3.4.

All ratios with steps of 10 wt% were polymerized. The following data however, only shows the ratios HEMA:METAC 100:0 to 50:50, because with a higher METAC ratio than 50 wt% in the solution, the bulk polymer lost its shape during swelling. Already by comparing the size of the swollen bulk polymers (Figure 53 A-F) it can be observed, that the volume of the swollen bulk polymer is lowest without METAC as a copolymer (Figure 53 A). From 10 wt% of METAC (Figure 53 B) to 20 wt% (Figure 53 C) the volume is increasing, which indicates, that the swelling degree is higher with higher ratios of METAC.

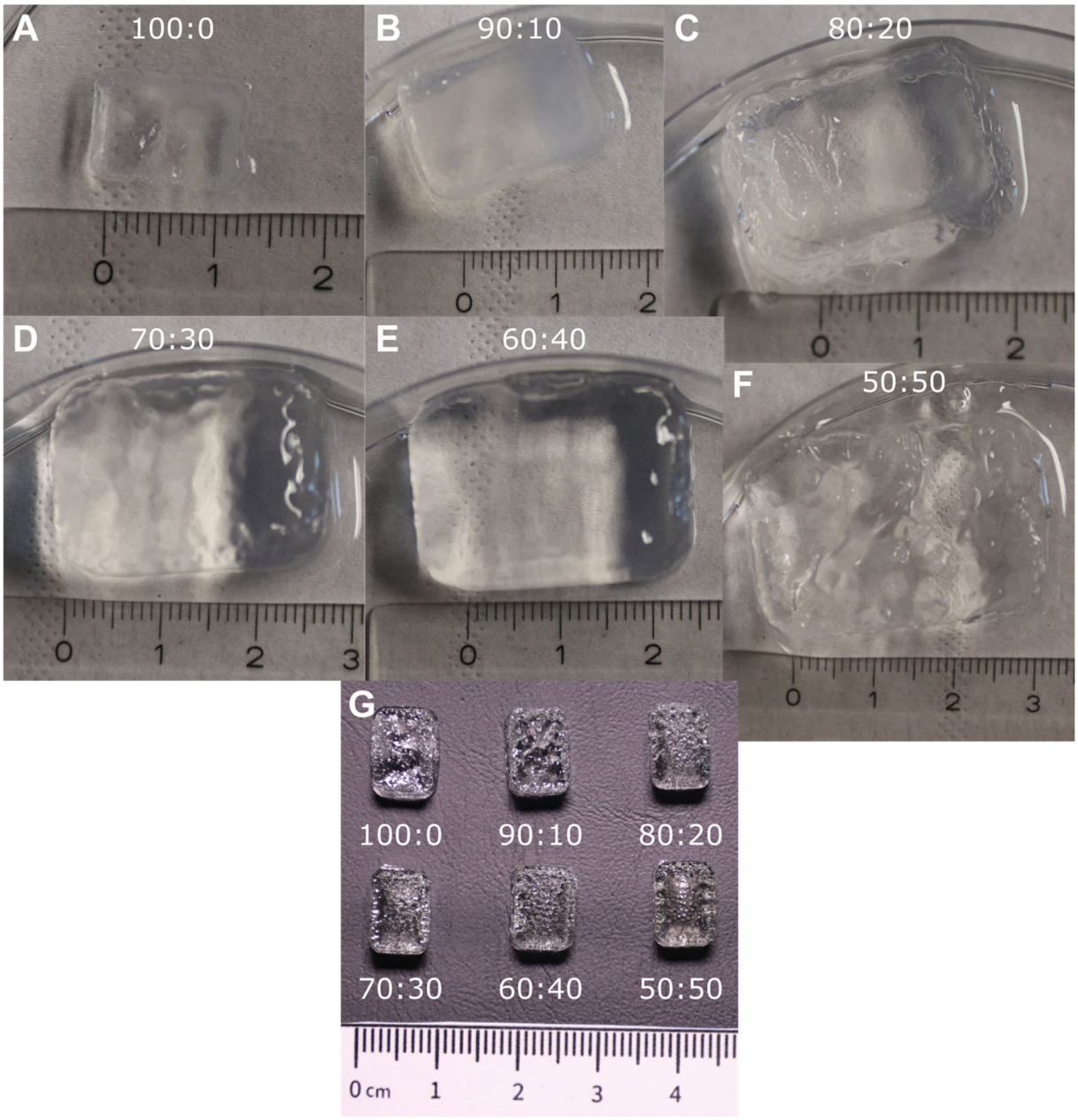

Figure 53: *Images of different P(HEMA-co-METAC) bulk polymers with different wt% ratios stated in the images. The ratios represent only the ratio between HEMA and METAC in a 45 wt% aqueous solution. Bulk polymers in swollen state (A-F) and dry state (G)*

These findings can be confirmed by looking at the swelling degree (Figure 54) (for more detail on the data see chapter 7.3.4). This shows, that the swelling degree of a P(HEMA-co-METAC) copolymer is increasing with higher ratios of METAC in the monomer solution, since METAC is more hydrophilic than HEMA due its cationic side chain. Interestingly, the swelling degree increases a lot more when METAC is added to the monomer solution compared to MEDSAH (see chapter 4.2.1). While 50 wt% of

MEDSAH show a swelling degree of 1124 %, 50 % of METAC show a swelling degree of about 24500 %, which is more than 20 times higher.

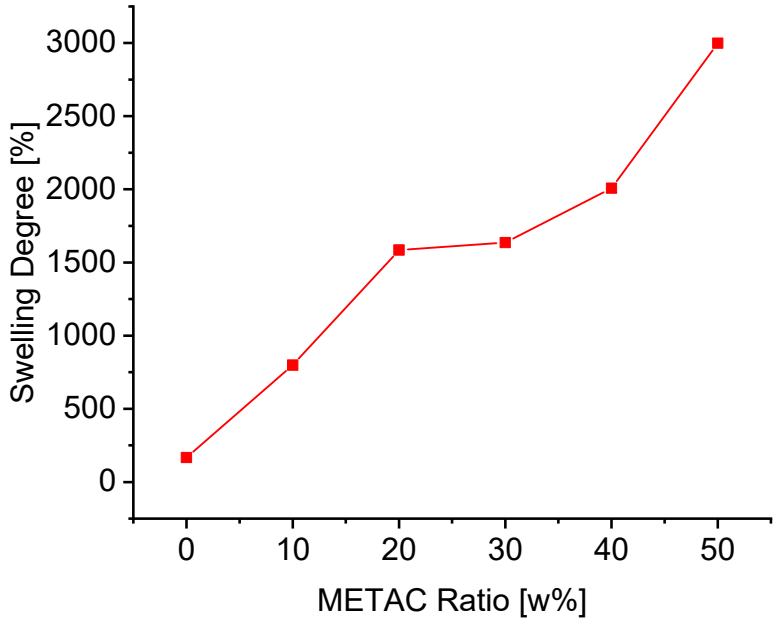

Figure 54: *Swelling degree of the different P(HEMA-co-METAC) bulk polymers, while the METAC ratio is the ratio between METAC and HEMA in a 45 wt% aqueous solution.*

For the following tests of the biological properties, the ratio of HEMA:METAC 80:20 was chosen, because from a METAC ratio of 30 wt% on, the bulk polymer, while keeping its shape, was very fragile and hard to handle. The 80:20 ratio in contrast still had a high swelling degree of 1298 %, but was rigid enough to be easily handled. For a coating, that is proposed to be suitable for implants, a soft, but sill rigid coating is desirable.

The coating was then performed via static SIPGP on MEW printed PCL scaffolds (printed by Ezgi Bakirci at the *Department for Functional Materials and Dentistry* (FMZ) in Würzburg, Germany) and PVDF scaffolds (printed by Juliane Kade at the *Department for Functional Materials and Dentistry* (FMZ) in Würzburg, Germany).

To proof a successful coating, stereomicroscope images of coated PCL (Figure 55 A) and PVDF (Figure 55 B) were taken. Interestingly, though being coated via static SIPGP there is no bulk polymer visible in between the hatches for the

P(HEMA-co-METAC) coating. To further investigate this, confocal fluorescence images were taken. To do so, the samples were immersed in a $3x10^{-4}$ M aqueous fluorescein sodium solution (for details on the procedure see chapter 7.3.6). The samples were then washed with water in order to remove dye adhered to the surface of the samples.

The pristine PCL scaffold (Figure 55 C), does not show any fluorescence, while the coated PCL scaffold (Figure 55 E) shows fluorescence on the surface of the fibres. This proofs the presence of the P(HEMA-co-METAC) coating on the PCL scaffold. For the PVDF scaffold, the pristine scaffold (Figure 55 D) shows low fluorescence, which results from adhered dye on the surface, which could not be removed by immersing the samples in water. The coated PVDF scaffold (Figure 55 F) in contrast, shows high fluorescence, which proofs that there is also a coating present on the PVDF scaffolds. Interestingly, also the fluorescence images show that the P(HEMA-co-METAC) coating is quite homogeneously distributed over the fibres in contrast to the P(HEMA-co-MEDSAH) coating on scaffolds described in chapter 4.4.

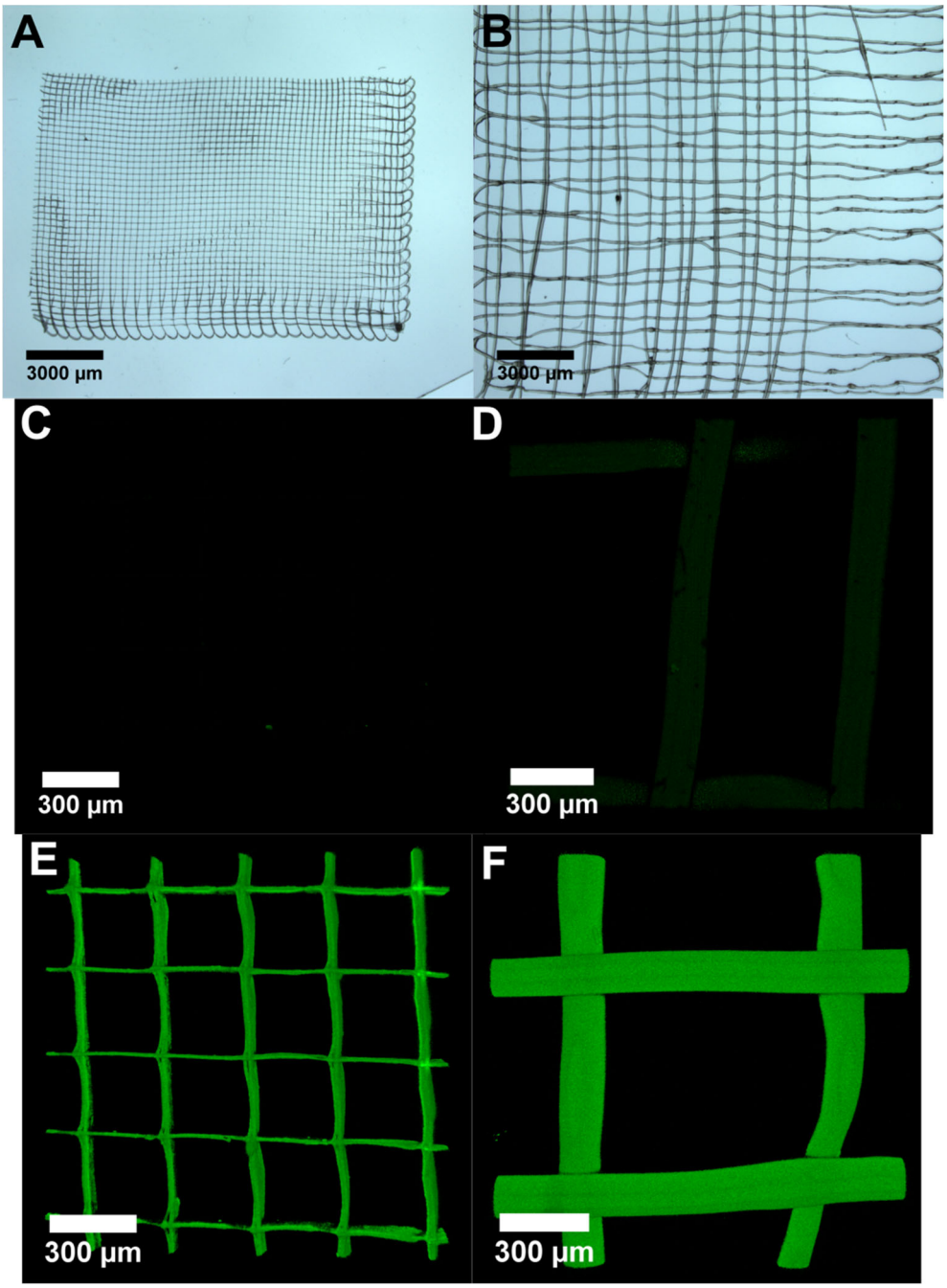

Figure 55: *Stereo microscope images of P(HEMA-co-METAC) coated PCL scaffold (A) and PVDF scaffold (B). Fluorescence images of pristine PCL scaffold (C) and PVDF Scaffold (D). Fluorescence images of P(HEMA-co-METAC coated PCL scaffold (E) and PVDF scaffold (F).*

In the following chapters the two described coatings P(HEMA-co-MEDSAH) and P(HEMA-co-METAC) will be examined for their biological properties.

4.5.2 Cytotoxicity

The biological experiments in this chapter were performed by Ezgi Bakirci at the *Department for Functional Materials and Dentistry* (FMZ) in Würzburg, Germany. For further improvement of cytocompatibility and, more important, improvement of cell adhesion, as a subsequent coating step RGD-sequences were added to the surface via static SIPGP (Figure 56). To be able to use RGD sequences for SIPGP, the sequences used were C_{ter} acrylate modified G-R-G-D-S-P sequences. Also scrambled RGD sequences, C_{ter} acrylate modified G-R-G-E-S-P, were used. The solution used for the coating is described in chapter 7.3.11.

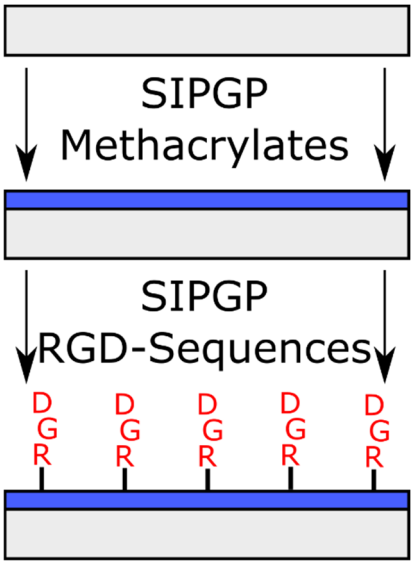

Figure 56: *2-Step static SIPGP. First step is the of coating with methacrylates such as P(HEMA-co-METAC) or P(HEMA-co-MEDSAH). The second step is static SIPGP of a RGD-sequence on top of the hydrogel.*

The RGD sequences however, cannot only be coated on top of a pre-existing coating, but can be coated directly on PCL as well. For the following experiments, PCL scaffolds were coated with only P(HEMA-co-METAC), with only the RGD-sequence and with P(HEMA-co-MEATC) as a first step and the RGD-sequence as a second step coating (same for scrambled RGD). The cytotoxicity of these samples was then tested by exposing L929 mouse fibroblasts to the scaffolds and evaluated by fluorescence images of a life/dead (green/red) staining (Figure 57).

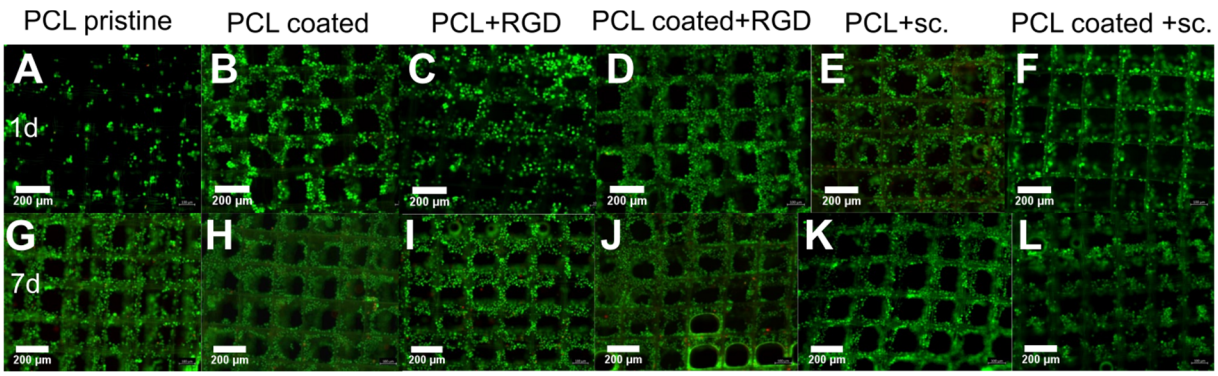

Figure 57: *Life(green)/dead(red) staining of L929 mouse fibroblasts after 1 d (A-F)and 7 d (E-L). The tests samples were pristine PCL scaffolds (A, G) P(HEMA-co-METAC) coated PCL scaffolds (B, H), RGD coated PCL scaffolds (C, I), PCL scaffolds coated with P(HEMA-co-METAC) as a first step and RGD as a second step (D, J), PCL coated with scrambled RGD (E, K) and PCL scaffolds coated with P(HEMA-co-METAC) as a first step and scrambled RGD as a second step (F, L).*

The cell count of these measurements was very high, so there could not be identified much difference between those samples. However, by analysing the life/dead staining it can be stated that there are the least cells visible after 1 d on the pristine PCL scaffolds (Figure 57 A). All the coated samples (Figure 57 B-F) show a higher number of visible cells on their surfaces. This means, that all the performed coatings are cytocompatible and can be used for further measurements of the cell adhesion. Also Picogreen and WST (water soluble tetrazolium) tests were performed, but since the cell number was so high on all the samples, they do not add much to the previously made statement and can be found in chapter 7.3.11.

4.5.3 Cell Adhesion

The biological experiments in this chapter were performed by Ezgi Bakirci at the *Department for Functional Materials and Dentistry* (FMZ) in Würzburg, Germany. U87 cells were used to perform the experiment (for more detail see chapter 7.3.11). The results are evaluated by the staining of the cell cytoskeleton protein F-actin (red), the membrane-cytoskeletal protein in focal adhesion plaques (green) and the cell nucleus (blue) after 1 d (Figure 58 A-F) and 3 d (Figure 58 G-L).

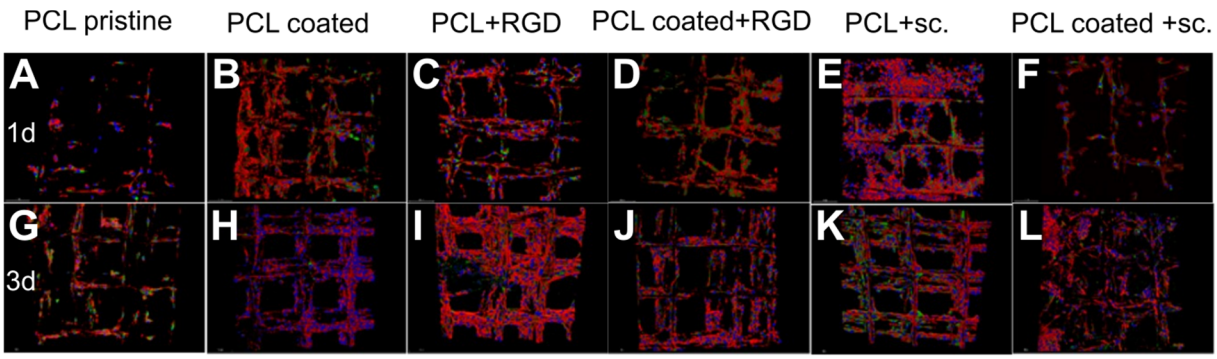

Figure 58: *Staining of U87 cells after 1 d (A-F)and 3 d (G-L). The cell cytoskeleton protein F-actin was stained with phalloidin (red), the membrane-cytoskeletal protein in focal adhesion plaques with vinculin (green) and the cell nucleus with DAPI (blue). The tests samples were pristine PCL scaffolds (A, G) P(HEMA-co-METAC) coated PCL scaffolds (B, H), RGD coated PCL scaffolds (C, I), PCL scaffolds coated with P(HEMA-co-METAC) as a first step and RGD as a second step (D, J), PCL coated with scrambled RGD (E, K) and PCL scaffolds coated with P(HEMA-co-METAC) as a first step and scrambled RGD as a second step (F, L).*

The images of the pristine scaffold (Figure 58 A, G) only show a very limited amount of cells on the scaffold after 1 d, as well as after 3 d. Also a low adhesion can be observed on the coated PCL scaffold coated with scrambled RGD as a second step after 1 d (Figure 58 F). After 3 d, however the adhesion improves in contrast to the pristine scaffold (Figure 58 G). All other coated scaffolds show an improved adhesion.

This shows, that not only the hydrogel coating of P(HEMA-co-METAC) on the scaffolds can improve the cell adhesion, but also the RGD coating on the scaffolds can do so. This makes the P(HEMA-co-METAC) coating a suitable candidate for a coating on implants. Additionally, SIPGP can also be used to modify surfaces with peptide sequences such as RGD sequences, if they are properly functionalized (as in this case with a C_{ter} acrylate moiety).

The P(HEMA-co-MEDSAH) coating instead is supposed to prevent adhesion due to its zwitterionic sidechains.[110] This behaviour was examined by placing U87 Glioblastoma cells on MEW printed PVDF scaffolds 1 d and 4 d (Figure 59). On the pristine PVDF scaffold (Figure 59 A, G) the red colour indicates the adhesion of some cells, where the PVDF scaffold coated with only RGD (Figure 59 B, H) shows a huge number of cells. When the PVDF scaffold is coated with P(HEMA-co-METAC) (Figure 59 C, I) the number of adhered cells is higher than on the pristine scaffold and could be increased by adding RGD-sequences as a second step to the coating (Figure 59 D, J). The P(HEMA-co-MEDSAH) coated PVDF scaffold (Figure 59 E, K) in contrast, shows no

adhered cells at all. The subsequent coating with RGD (Figure 59 F, L) then lead to a small number of adhered cells.

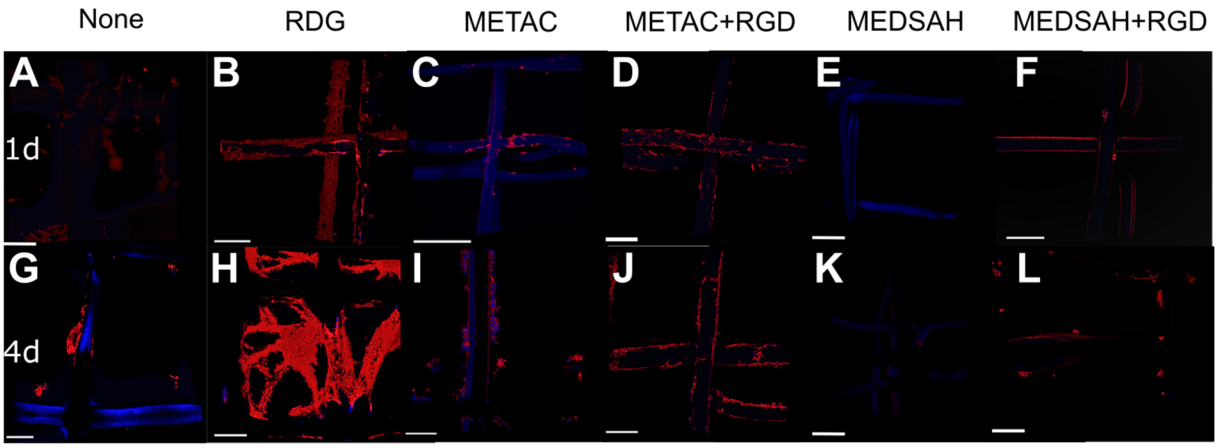

Figure 59: *Staining of U87 cells after 1 d (A-F)and 4 d (G-L). The cell cytoskeleton protein F-actin was stained with phalloidin (red) and the cell nucleus with DAPI (blue). The tests samples were pristine PVDF scaffolds (A, G), RGD coated PVDF scaffolds (B, H), P(HEMA-co-METAC) coated PVDF scaffolds (C, I), P(HEMA-co-METAC)+RGD coated PVDF scaffolds (D, J), P(HEMA-co-MEDSAH) coated PVDF scaffolds (E, K) and P(HEMA-co-MEDSAH)+RGD coated scaffolds (F, L). The writing above the images provides information about the used copolymer for HEMA. The scale bars are 200 µm.*

These experiments show, that SIPGP can be utilized to directly coat MEW printed PVDF scaffold with RGD sequences, if they are properly functionalized (as in this case with a C_{ter} acrylate moiety). The P(HEMA-co-METAC) (as previously shown) could be used to increase the number of cells adhered on the scaffolds. The P(HEMA-co-MEDSAH) coating instead proofed to function as a non-adhesive and with that an anti-fouling coating, since no cells adhered in this experiment. This property then could be masked to a small extent by adding a subsequent RGD coating in a second coating step. An increased concentration of the RGD-sequences on the solution for the coating reaction could be a way to increase this masking effect in the future.

4.5.4 Conclusion

Two coatings were examined for their use for biomedical applications. It was shown, that a coating with P(HEMA-co-METAC) via SIPGP is cytocompatible (L929 mouse fibroblasts) and can be used to increase cell adhesion (U87 glioblastoma cells) on the tested scaffolds. P(HEMA-co-MEDSAH) instead can be used as a non-adhesive (U87 glioblastoma cells) and with that anti-fouling coating. In addition, it was shown that MEW printed PCL and PVDF scaffolds can be coated with RGD sequences via SIPGP to improve the biological properties. These RGD-sequences could also be coated as a subsequent step on top of the P(HEMA-co-METAC) and P(HEMA-co-MEDSAH) coatings to do so.

5 Summary and Outlook

5.1 Summary

Self-initiated photografting and photopolymerization (SIPGP) is a coating technique that got little attention so far. This work however, enhanced the possibilities of SIPGP by developing dynamic SIPGP in addition the already present static SIPGP. Also the value of SIPGP for the field of biomedical applications was demonstrated. To achieve this, several steps were taken.

Custom designed reactor

To perform dynamic SIPGP, a special custom designed reactor was developed. After an initial reactor design was created using the 3D modelling software *blender*, the reactor was printed via DLP printing. The printed reactor was then tested for its suitability for static and dynamic SIPGP. The rapid prototyping was then used to further improve different types of reactors, until a final reactor design was fabricated of stainless steel, which could be used for both static and dynamic SIPGP. To examine the flow of monomer solution through this new reactor theoretical calculations were made for this system by using the multiphysics software *COMSOL*.

Static SIPGP Parameters for the new System

Having the custom designed reactor, appropriate coating parameters for this new reaction system were examined. To do so, P(VDF-TrFE-CTFE) films were used, which were not used for SIPGP to this point. The coating material used for these experiments was P(HEMA-co-MEDSAH), which proofed to be an anti-fouling coating, containing zwitterionic sidechains. The parameters for the reaction were mainly examined via contact angle. Using this coating the influence of two different UV sources (a 25 W lamp and a 400 W lamp) were examined. This showed, that, as expected, the reaction speed can be increased by using a lamp with increased irradiation, so the 400 W lamp was chosen to perform further experiments. Also the influence of oxygen inside the

reaction solution was examined, finding that a deoxygenation is not mandatory to perform SIPGP, but increases the reaction speed and the controllability of the reaction. For this reason, in further experiments all the solutions were deoxygenated prior to use. Two additional important parameters for SIPGP are the distance between the sample and the light source (d_{ls}) and the irradiation time (t_i). The examination of t_i showed, that the contact angle decreased linearly with increased t_i, because the dose is decreasing linearly. The second parameter influencing the dose is d_{ls}, which does so in a more quadratically nature. At d_{ls} = 5 cm and t_i = 60 s a contact angle of 55° could be achieved using static SIPGP.

The previously mentioned parameters were also verified by IR spectroscopy, fluorescence spectroscopy and scanning electron microscopy. This showed not only that the examined coating is a hydrogel, but also that this coating can even be used to add macroscopic movement by changing the air humidity on films with a thickness of 10 µm.

Dynamic SIPGP

After examining suitable parameters for the newly designed system, dynamic SIPGP could be developed. For the first time, SIPGP was performed while applying a constant flow of monomer solution through the reaction system. This added a new parameter: the flow rate (r_{fl}). Accordingly, this parameter was examined, comparing dynamic to static SIPGP. It could be shown, that by applying higher r_{fl} to the system, the contact angle increases, which indicates a slower coating. The flow patterns inside the reactor were then modelled and calculated. These calculations indicated, that, due to higher flow velocities, the contact angle on the coated samples would be lower on the sides of the sample and higher in the middle. This finding was verified by contact angle measurements. The influence of dynamic SIPGP on the temperature inside the reaction chamber during the reaction was examined by temperature sensors inside the reactor. This showed, that the constant flow of monomer solution can be utilized to decrease the warming of the reaction solution during the reaction. Finally it was shown, that dynamic SIPGP can decrease the formation of bulk polymer on the sample, which is forming during the reaction. This enables SIPGP to fabricate more homogeneous coatings by applying a constant monomer flow.

SIPGP on Scaffolds

After the System was examined and described on planar films, SIPGP was also performed on MEW printed scaffolds of PCL, PVDF and P(VDF-TrFE). It was shown, that not only planar samples can be coated using SIPGP, but also these more complex structures. The influence of dynamic SIPGP on coating MEW printed scaffolds was investigated and showed, that the “webbing” that occurs by using static SIPGP can be prevented by utilizing dynamic SIPGP. Additionally the homogeneity of the coating could be improved compared to static SIPGP. In order to examine the coated scaffolds, stereo microscopy, fluorescence microscopy and scanning electron microscopy were utilized.

Biological properties

To show the value of SIPGP for biomedical applications, a different coating material was introduced, P(HEMA-co-METAC). This material proved to be non-cytotoxic, as expected. Then P(HEMA-co-METAC) as well as P(HEMA-co-MEDSAH) were coated with RGD sequences by using SIPGP. The sequences also were coated directly to the scaffolds via SIPGP. This showed, that a second coating step via SIPGP can be utilized to further functionalize the fabricated coatings. The coating with RGD sequences, as well as the P(HEMA-co-METAC) coating showed improvements in cell adhesion of U87 cells. The P(HEMA-co-MEDSAH) coating showed anti-adhesion properties, that could be masked to a small extend by a second coating step with RGD sequences.

This implements that the value of these coating and SIPGP in general for biomedical applications is high and can be proposed as coating materials/techniques for biomedical implants.

5.2 Outlook

The presented work developed a new technique, which opens a wide perspective of further investigations.

The reactor was designed to coat samples of only a small size (maximum of 1 cm x 2 cm). New reactor types can be developed to coat bigger samples. Also reactors with a silica glass on the bottom could be developed in order to irradiate the upside and downside of the samples equally at the same time using two equal sources of UV light. Another interesting design would be a reactor containing obstacles for the flow in order to fabricate coating patterns on planar samples.

Especially interesting would be an upscaling of the system to industrial levels, since it is a fast coating procedure, which allows the use of water as a solvent and the omission of initiators or other expensive additions. In case of this work also comparably cheap monomers are used for the coating procedure. This would make SIPGP suitable for an industrial scale production.

Since SIPGP is capable of coating a huge variety of materials with a huge variety of polymers, a lot of different products can be fabricated in the future. For instance, the “webbing” could be produced intentionally to gain pores for scaffolds, which can open and close due to stimuli such as humidity, temperature or pH value. Also composite materials could be fabricated by adding many different functional layers utilizing SIPGP. The value of dynamic SIPGP, being a new technique, needs to be investigated in more detail, mostly when non-planar samples are being used. There the reactor design could be calculated according to the geometry of the sample, in order to achieve a homogeneous coating on a non-planar substrate.

The biological properties that could be added to materials via SIPGP were only treated roughly in this work. Here only the possibility of usage for biomedical applications was shown. Bigger studies however, could now be performed on SIPGP coated materials. With this, actual applications, such as implant coatings would be interesting to be tested in broader biological or even clinical studies.

6 Zusammenfassung und Ausblick

6.1 Zusammenfassung

Self-initiated photografting and photopolymerization (SIPGP) ist eine Beschichtungsmethode, die bisher nur wenig Beachtung fand. Diese Arbeit vergrößerte aber die Möglichkeiten von SIPGP, indem das dynamische SIPGP, zusätzlich zum schon bekannten statischen SIPGP, entwickelt wurde. Auch der Wert von SIPGP für biomedizinische Anwendungen wurde gezeigt.

Speziell angepasster Reaktor

Um dynamisches SIPGP durchführen zu können wurde ein speziell angepasster Reaktor entwickelt. Nachdem ein anfängliches Reaktordesign mit der 3D-Modellierungssoftware *blender* entworfen wurde, wurde der Reaktor mit einem DLP-Drucker gedruckt. Der so erhaltene Reaktor wurde anschließend auf seine Eignung für statisches und dynamisches SIPGP getestet. Das sogenannte *rapid prototyping* wurde genutzt, um mehrere Reaktortypen weiter zu verbessern, bis ein finaler Reaktor aus rostfreiem Stahl hergestellt wurde, der für statisches und dynamisches SIPGP genutzt werden konnte. Um den Fluss der Monomerlösung durch den neuen Reaktor zu untersuchen, wurden theoretische Berechnungen für dieses System mit der *multiphysics* Software *COMSOL* gemacht.

Parameter des neuen Systems für statisches SIPGP

Für das neu entwickelte Reaktionssystem wurden geeignete Beschichtungsparameter gesucht. Dafür wurden P(VDF-TrFE-CTFE)-Folien genutzt, die bisher noch nicht für SIPGP verwendet wurden. Als Beschichtungsmaterial für diese Experimente wurde P(HEMA-co-MEDSAH) genutzt, welches sich als eine *anti-fouling*-Beschichtung herausstellte, da es zwitterionische Seitenketten besitzt. Die Parameter für die Reaktion wurden hauptsächlich mit Kontaktwinkel-Messungen untersucht. Anhand dieser Beschichtung wurden zunächst zwei unterschiedliche UV-Quellen (eine 25 W Lampe und

eine 400 W Lampe) untersucht. Dies zeigte, dass die Reaktionsgeschwindigkeit, wie erwartet, erhöht werden kann, indem eine Lampe mit erhöhter Strahlung verwendet wird, weshalb die 400 W Lampe für weitere Experimente verwendet wurde. Auch der Einfluss von Sauerstoff in der Reaktionslösung wurde untersucht. Dabei wurde herausgefunden, dass das Entfernen von Sauerstoff vor der Reaktion nicht zwingend notwendig ist, um SIPGP durchführen zu können, es aber die Reaktionsgeschwindigkeit und die Kontrollierbarkeit der Reaktion erhöht. Deshalb wurden in den weiteren Experimenten Sauerstoff aus allen Reaktionslösungen entfernt. Zwei weitere wichtige Parameter für SIPGP sind der Abstand zwischen Probe und Lichtquelle (d_{ls}) sowie die Bestrahlungsdauer (t_i). Die Untersuchung von t_i zeigte, dass der Kontaktwinkel linear mit erhöhter t_i abfällt, weil die Strahlungsdosis linear abnimmt. Der zweite Parameter, der die Strahlungsdosis beeinflusst, ist d_{ls}, der darauf einen eher quadratischen Einfluss hat. Bei d_{ls} = 5 cm und t_i = 60 s konnte mit statischem SIPGP ein Kontaktwinkel von 55° erreicht werden.

Die genannten Parameter wurden auch durch IR-Spektroskopie, Fluoreszenzmikroskopie und Rasterelektronenmikroskopie bestätigt. Dies zeigte nicht nur, dass die untersuchte Beschichtung ein Hydrogel ist, sondern auch, dass diese Beschichtung dazu genutzt werden kann makroskopische Bewegungen bei Folien mit einer Dicke von 10 µm durch Veränderung der Luftfeuchtigkeit zu verursachen.

Dynamisches SIPGP

Nachdem für das neu entworfene System geeignete Parameter untersucht wurde, konnte das dynamische SIPGP entwickelt werden. Zum ersten Mal wurde SIPGP durchgeführt, während ein konstanter Fluss von Monomerlösung durch das System geleitet wurde. Das fügte einen neuen Parameter hinzu: die Flussrate (r_{fl}). Diese wurde untersucht, indem dynamisches und statisches SIPGP verglichen wurden. Es konnte gezeigt werden, dass mit höheren r_{fl} der Kontaktwinkel anstieg, was auf eine langsamere Beschichtung hindeutet. Daraufhin wurden die Flussmuster innerhalb des Reaktors modelliert und berechnet. Diese Berechnungen deuteten darauf hin, dass der Kontaktwinkel an den Seiten der beschichteten Probe, durch erhöhte Fließgeschwindigkeiten, höher sind als in der Mitte. Dies wurde dann auch durch Kontaktwinkel-Messungen bestätigt. Der Einfluss von dynamischem SIPGP auf die Temperatur innerhalb

der Reaktionskammer während der Reaktion wurde mit Temperatursensoren innerhalb des Reaktors untersucht. Dies zeigte, dass der konstante Fluss von Monomerlösung dazu genutzt werden kann, die Erwärmung der Reaktionslösung während der Reaktion zu verringern. Abschließend wurde gezeigt, dass dynamisches SIPGP die Entstehung von *bulk*-Polymer auf der Probe, welches während der Reaktion entsteht, reduzieren kann. Dadurch ist es möglich durch SIPGP gleichmäßigere Beschichtungen zu erzeugen, indem ein konstanter Monomerfluss hinzugefügt wird.

SIPGP auf Scaffolds

Nachdem das System auf planaren Folien untersucht und beschrieben wurde, wurde SIPGP auch auf MEW-gedruckten *scaffolds* aus PCL, PVDF und P(VDF-TrFE) durchgeführt. Es konnte gezeigt werden, dass nicht nur planare Proben, sondern auch komplexere Strukturen durch SIPGP beschichtet werden können. Der Einfluss von dynamischem SIPGP auf die MEW-gedruckten *scaffolds* wurde untersucht und hat gezeigt, dass das *„webbing“*, das bei statischem SIPGP auftritt, verhindert werden kann. Zur Untersuchung der beschichteten *scaffolds* wurden Stereomikroskopie, Fluoreszenzmikroskopie und Rasterelektronenmikroskopie genutzt.

Biologische Eigenschaften

Um den Wert von SIPGP für biomedizinische Anwendungen zu zeigen, wurde ein neues Beschichtungsmaterial genutzt, P(HEMA-co-METAC). Dieses Material hat sich, wie erwartet, als nicht zytotoxisch herausgestellt. Daraufhin wurden P(HEMA-co-METAC) und P(HEMA-co-MEDSAH) durch SIPGP mit RGD-Sequenzen beschichtet. Die *scaffolds* wurden auch direkt durch SIPGP mit diesen Sequenzen beschichtet. Dies zeigte, dass ein zweiter SIPGP-Beschichtungsschritt dazu genutzt werden kann, die erhaltenen Beschichtungen weiter zu funktionalisieren. Die Beschichtung mit RGD-Sequenzen und auch mit P(HEMA-co-METAC) zeigten Verbesserungen der Zelladhäsion von U87-Zellen. Die P(HEMA-co-MEDSAH)-Beschichtung zeigte anti-adhäsive Eigenschaften, welche durch eine zweite Beschichtung mit RGD-Sequenzen in geringem Maße maskiert werden konnte.

Dies zeigt, dass der Wert dieser Beschichtungen, und SIPGP generell, für biomedizinische Anwendungen hoch ist und somit gut für biomedizinische Implantate genutzt werden könnte.

6.2 Ausblick

In der gezeigten Arbeit wurde eine neue Technik entwickelt, welche eine weite Perspektive für weitere Untersuchungen bietet.

Der Reaktor wurde entworfen, um kleine Proben (maximal 1 cm x 2 cm) zu beschichten. Daher könnten neue Reaktortypen entwickelt werden, um größere Proben beschichten zu können. Auch Reaktoren mit einem Kieselglas-Boden könnten entwickelt werden, um die Ober- und Unterseite der Proben gleichmäßig mit identischen UV-Quellen bestrahlen zu können. Ein weiteres interessantes Design könnten Hindernisse für den Fluss sein, um so Beschichtungsmuster auf planaren Proben zu erzeugen.

Besonders interessant wäre ein *upscaling* des Systems auf industrielle Maße, da es eine schnelle Beschichtungsweise ist, die Wasser als Lösungsmittel und das Weglassen von Initiatoren oder teuren Additiven erlaubt. In dieser Arbeit wurden auch vergleichsweise billige Monomere für die Beschichtung genutzt. Dies macht SIPGP geeignet für eine Produktion von industriellem Maß.

Da es mit SIPGP möglich ist, eine große Anzahl an Materialien mit einer großen Anzahl an Polymeren zu beschichten, können in Zukunft sehr viele Produkte hergestellt werden. Zum Beispiel kann das *„webbing“* gezielt herbeigeführt werden, um Poren zu generieren, die sich durch Stimuli wie Luftfeuchtigkeit, Temperatur oder pH-Wert öffnen und schließen lassen. Auch Komposite könnten hergestellt werden, indem man einem Material durch SIPGP unterschiedliche funktionelle Schichten hinzufügt. Der Wert von dynamischem SIPGP, besonders für nicht-planare Proben, muss noch weiter untersucht werden, da es eine neue Technik ist. Es könnte zum Beispiel ein Reaktordesign passend zur Geometrie der Probe berechnet werden, um nicht-planare Proben gleichmäßiger zu beschichten.

Die biologischen Eigenschaften, die Materialien durch SIPGP hinzugefügt werden konnten, wurden in dieser Arbeit nur wenig untersucht. Es wurde nur die Möglichkeit für einen Nutzen für biomedizinische Anwendungen gezeigt. Breitere Studien könnten nun auf beschichteten Materialien durchgeführt werden. Dabei wären besonders Anwendungen wie Implantat-Beschichtungen interessant, um in größeren biologischen oder sogar klinischen Studien getestet zu werden.

7 Experimental

7.1 Equipment and Methods of Measurement

7.1.1 Equipment

Digital Light Processing (DLP) Printer and Resins

The DLP printer used was the *Autodesk Ember* with its open source software *Spark*. The Designs of the reactors were made by using the 3D software *Blender*. The resins used for the printer were the *Autodesk Clear PR48* with the following composition: 2,4,6-Trimethylbenzoyl-diphenyl-phosphineoxide 0.40 %; 2,2'-(2,5-thiophenediyl)-bis(5-tert-butylbenzoxazole) 0.16 %; genomer 1122 19.89 %; ebecryl 8210 39.78 %; stratomer SR 494 39.77 %, and the *Autodesk Black PR57-K* with black pigment added. The device for post curing was the *Otoflash G171 N2.*

Density

For measurement of densities a *DMA 4100 M* (*Anton Paar, Graz, Austria*) was used, working on the flexural resonator concept.

Viscosity

For viscosity measurements a *LOVIS 2000M* microviscosimeter (*Anton Paar, Graz, Austria*) was used by equipping a *LOVIS 1.8* capillary with a steel ball inside (Mat. No. 73109, diameter 1.5 mm, steel 1.4125)

Flow Calculations

The calculations of the reaction chamber was performed using the multiphysics software *COMSOL 5.3* containing the *microfluidics* module. The models were prepared previously with the 3D-software *Blender*.

Water Purification

For water purification the *Barnstead MicroPure* (*Thermo Scientific*) was used. With a water purity maximum of 0.057 µS/cm at 22 °C.

Photographs

The camera used to do the photographs was a *CANON 77D* with a *Sigma 18-300 mm* Objective attached.

UV-Lamp (25 W)

The lamp used was an *EXO TERRA Reptile UVB200 PT2341* with 25 W attached to an *EXO TERRA Light Dome Aluminium UV Reflector Lamp PT2057* with a diameter of 18 cm.

UV chamber (400 W)

This chamber was a *DYMAX ECE 5000 Flood* (*DYMAX Europe GmbH*, Wiesbaden, Germany) with a 400 W metal halide bulb and with an area for irradiation of 12.7x12.7 cm. For irradiation a timer for 1-99 s could be activated opening the shutter. For irradiations of more than 99 s the shutter was set to *manually*. The screw in the front right bottom was removed to insert a tube for argon supply. For dynamic SIPGP the screw in the back left bottom was removed to insert a polyurethane tube for monomer supply. For temperature measurements the front left screw was removed to insert the temperature sensor cables.

Radiometer

The radiometer to measure the dose of the *DYMAX ECE 5000 Flood* was the *DYMAX ACCU-CAL 160* (*DYMAX Europe GmbH*, Wiesbaden, Germany).

Contact Angle

For contact angle measurements the *KRÜSS Drop Shape Analyser DSA25S* (*Krüss GmbH*, Hamburg, Germany) was used with the software Advance.

Infrared Spectroscopy (IR)

The spectrometer used was the *Jasco FT/IR-4100* by *Jasco Deutschland GmbH* (Darmstadt, Germany) equipped with PIKE MIRacle single reflection attenuated total reflection sampling accessory (ZnSe crystal, *PIKE Technologies*, Madison, Wisconsin, USA) and a deuterated triglycine sulfatedetector. The corresponding JASCO spectra manager V.2.07.00 software was used to evaluate the obtained spectra.

Scanning Electron Microscopy (SEM)

The SEM measurements were performed with a *ZEISS Supra 25 SEM (Carl Zeiss Microscopy GmbH,* Jena, Germany)

Sputter coating

For coating the SEM samples with platinum, the *Leica EM ACE600* (*Leica Microsystems GmbH*, Wetzlar, Germany) was used with the software *LASX*.

Confocal Fluorescence Microscopy

The samples were measured using the *TCS SP8* (*Leica Microsystems GmbH,* Wetzlar Germany)

Dynamic Vapour Sorption

The device used for these measurements was the *SPS11-10µg* (Proumid GmbH & Co. KG, Ulm, Germany). The device was located at the *Zentrum für angewandte Energietechnik* (ZAE) in Würzburg and was operated by Stephan Braxmeier.

Environmental Scanning Electron Microscopy (ESEM)

For ESEM measurements a *FEI Quanta FEG 250* was used with LFD,GAD and GSED for ESEM measurements. The machine was located at the university of Bayreuth and operated by Andreas Frank. The samples were frozen in liquid nitrogen und then broken in the middle by using two flat tweezers. This way a sharp breaking edge was produced.

Syringe pump

The pump used was the *Syringe Pump LA-30* by the company *behr Labor-Technik GmbH* (Düsseldorf, Germany).

Temperature Measurement

The device used for the temperature measurements was the *Pico USB TC-08 Temperature Data logger* by *Pico Technology* (Cambridgeshire, United Kingdom). With 3 K-type thermos elements with a diameter of 1.5 mm for -75 °C – 250 °C attached.

Stereomicroscopy

The microscope used was the *Cal Zeiss Discovery V.20* (*Carl Zeiss Microscopy GmbH,* Jena, Germany) with the *Zeiss icc5* 5 MP, 12 Bit colour camera. The software used was the Zen2012 pro.

7.1.2 Methods of Measurement

Infrared Spectroscopy (IR)

For Infrared Spectroscopy the samples were dried at room temperature for 24 h (after this time they reached a constant weight) and then placed face down on the ATR-Element.

Scanning electron Microscopy (SEM)

For SEM measurements conductive double sided adhesive carbon tabs were put on 12.7 mm pin stubs. On these carbon stubs the samples were placed and then sputtered with 4 nm of platinum.

Confocal Fluorescence Microscopy

The samples used for this method were immersed in an aqueous $3x10^{-4}$ M fluorescein sodium solution for 1 h. Then they were washed by immersing the samples in three different water baths for 24 h respectively and dried on air for 24 h.

7.2 Reagents and Solvents

2-Hydroxyethyl methacrylate (HEMA, CAS: 868-77-9), was purchased from *Merck KGaA*, (Darmstadt, Germany) containing ≤250 ppm monomethyl ether hydroquinone as inhibitor and a purity of 97 %. HEMA was distilled prior to use.

[2-(Methacryloyloxy)ethyl]dimethyl-(3-sulfoproply)ammonium hydroxide (MEDSAH, CAS: 3637-26-1) was purchased from *Merck KGaA*, (Darmstadt, Germany) with a purity of 95 %.

PVDF films were purchased from *Precision Acoustics LTD* (Dorchester, United Kingdom).

P(VDF-TrFE) powder (*Piezotech FC*) was purchased from *Piezotech Arkema* (Lyon, France).

P(VDF-TrFE-CTFE) powder (*Piezotech RT-TS*) was purchased from *Piezotech Arkema* (Lyon, France).

The P(VDF-TrFE-CTFE) (*Piezotech RT T sheets*) films were purchased from *Piezotech Arkema* (Lyon, France) annealed with a thickness of 10 µm ± 10 %.

Fluorescein disodium salt extra concentrated (C.I. 45350) (CAS: 518-47-8) was purchased from *Carl Roth GmbH & Co. KG* (Karlsruhe Germany).

Fluorescein-O-Methacrylate (CAS: 480439-15-4) was purchased from *Merck KGaA*, (Darmstadt, Germany) with a purity of 95 %.

Methanol (CAS: 67-56-1) was purchased from *Merck KGaA*, (Darmstadt, Germany) with a purity of ≥99.8 %.

The RGD sequence was a C_{ter} modified G-R-G-D-S-P sequence purchased from *GeneCust* (Boynes, France) with a purity of 97.1 %.

The scrambled RGD sequence was a C_{ter} modified G-R-G-E-S-P sequence purchased from *GeneCust* (Boynes, France) with a purity of 95.9 %.

7.3 Methods

7.3.1 Reactor Design

Reactor Printing

The reactors were printed with either the PR48-Clear Resin or the PR57-Black Resin from Autodesk. The models for the print were designed with *blender* and imported into *Spark* as STL files. The prints were performed with a layer thickness of 10 µm and 4 burn-in layers irradiated for 8 sec and the other layers for 4 sec. For the post processing the printed object was immersed in a bath of 2-propanol for 15 min and then in a second bath of 2-propanol for 15 min. After that the printed Object was dried in an oven at 55 °C for 30 min the post curing was performed with 30,000 UV-flashes at 10 Hz.

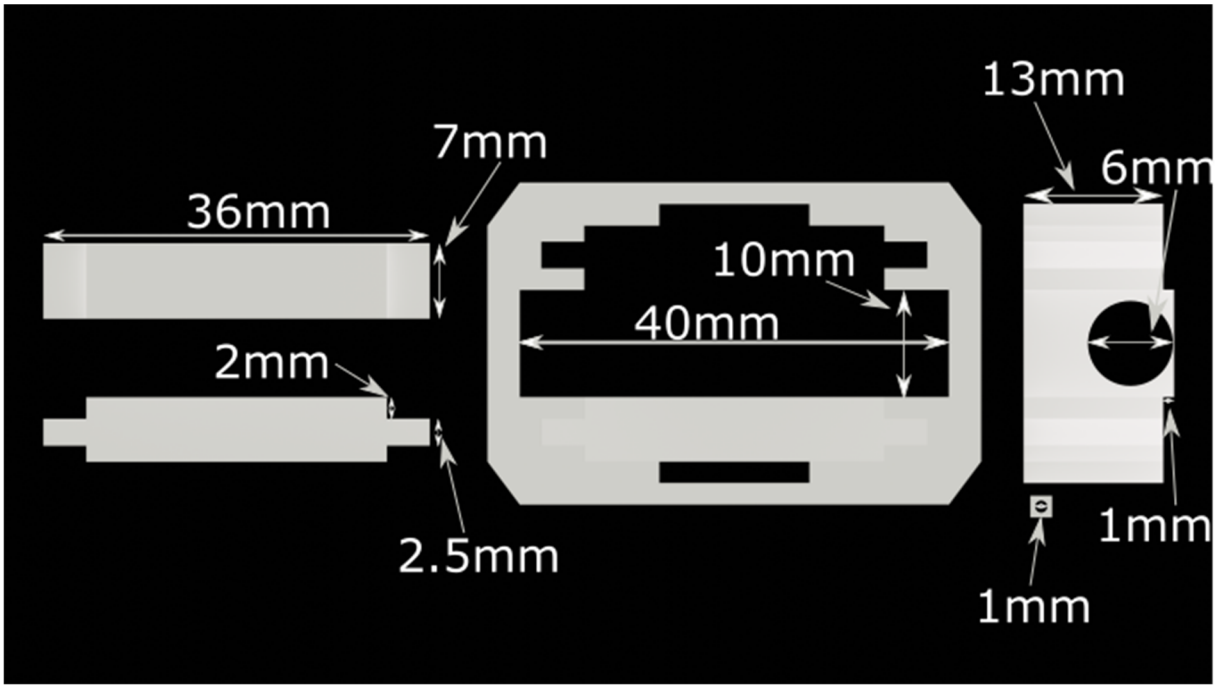

Figure 60: *Dimensions of the reactor body and the walls of the most frequently used model.*

Density and Viscosity

For density measurements the solution was put into the device via an aluminium foil covered syringe. The density data gathered was then used for the viscosity measurements. To perform those, the solution was put into the capillary and measurements between 20 °C and 50 °C with steps of 1 °C were performed.

Flow Calculations

The models for the calculations were designed with *blender* and imported into *COMSOL* as STL files. For the simulations the viscosity and density of the aqueous HEMA/MEDSAH solution was used.

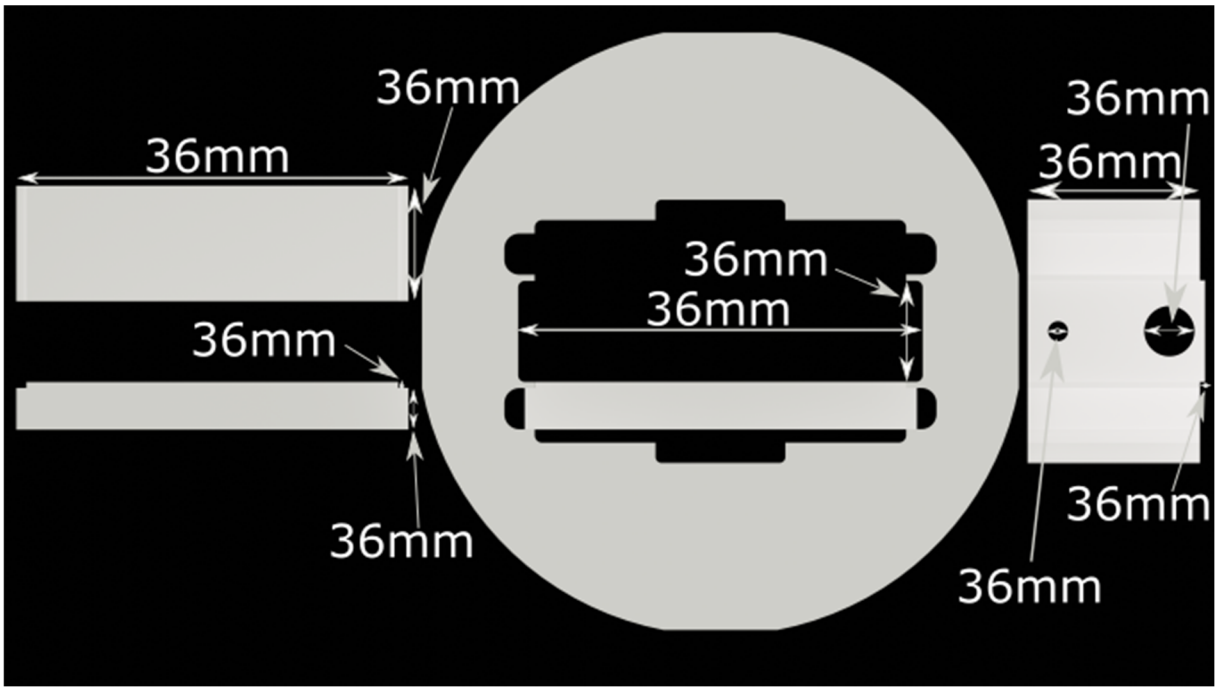

Figure 61: *Dimensions of the reactor body and the walls of the metal reactor.*

7.3.2 Preparation of self-made Polymer Films

P(VDF-TrFE) and P(VDF-TrFE-CTFE) films were fabricated from their respective polymer powders. To do so a silicon template made from *Sylgard 184* was fabricated for films with an area of 0.8x1.3 cm and a cut corner to know which is the front and which the back side during coating. Then 20 wt% of the powders were dissolved in 80 wt% acetone. Each film template was filled with 0.5 ml of the powder solution and was then dried at room temperature. The rims of these films were cut after drying. The P(VDF-TrFE-CTFE) films were only used to perform preliminary experiments. The data presented in this work was gathered by only using the purchased films. The P(VDF-TrFE) films however, were used as such.

7.3.3 Monomer solutions

HEMA/MEDSAH solution

For this solution HEMA was distilled prior to use. Millipore water with a maximum of 0.057 µS/cm at 22 °C was used. The composition of the solution was the following:

Water:	19.20 g
HEMA:	13.70 g
MEDSAH:	1.79 g

The solution was prepared in flasks wrapped in aluminium foil to exclude light and closed with a septum. Prior to polymerization the solution was deoxygenated passing argon for 30 min through the solution.

HEMA/METAC solution

For this solution HEMA was distilled prior to use. Millipore water with a maximum of 0.057 µS/cm at 22 °C was used. The composition of the solution was the following:

Water: 20.90 g

HEMA: 14.40 g

METAC: 3.60 g

The solution was prepared in flasks wrapped in aluminium foil to exclude light and closed with a septum. Prior to polymerization the solution was deoxygenated by passing argon for 30 min through the solution.

7.3.4 Bulk polymers

Bulk Polymerization of P(HEMA-co-MEDSAH)

For the bulk polymerization of P(HEMA-co-MEDSAH) 0.2 ml of the prepared solutions were filled into a silicon-form with an area of 0.7x1.0 cm and height of 1 cm for each solution. On top of the silicon form a silica glass was placed. Then the form was put under a 25 W UV lamp with a distance between the lamp and the silica glass of 1 cm. After 48 h of irradiation the samples were taken out of the silicon form and dried in an oven at 60 °C until their weight was constant. At that point the dry weight (W_d) was measured. Then the samples were put into Millipore water until their weight was constant. At this point their swollen weight (W_s) was measured out of this data the swelling degree was calculated. In these different solutions the ratio of monomer:water stayed the same at 55:45 wt%, while the ratio between the monomers was altered (Table 6). The swelling degree was calculated as follows:

$$S_D = \frac{W_s - W_d}{W_d} * 100$$

Table 6: *Swelling degree of P(HEMA-co-MEDSAH) bulk polymers with different ratios of monomers.*

HEMA [wt%]	MEDSAH [wt%]	W_d [mg]	W_s [mg]	S_d [%]
100	0	183	375	195
90	10	193	510	223
88	12	114	281	250
80	20	175	492	297
70	30	180	711	441
60	40	249	1837	824
50	50	246	2257	1124

Bulk Polymerzation of P(HEMA-co-METAC)

For the bulk polymerization of P(HEMA-co-METAC) 0.2 ml of the prepared solutions were filled into a silicon-form with an area of 0.7x1.0 cm and height of 1 cm for each solution. On top of the silicon form a silica glass was placed. Then the form was put under a 25 W UV lamp with a distance between the lamp and the silica glass of 1 cm. After 48 h of irradiation the samples were taken out of the silicon form and dried in an oven at 60 °C until their weight was constant. At that point the dry weight (W_d) was measured. Then the samples were put into Millipore water until their weight was constant. At this point their swollen weight (W_s) was measured out of this data the swelling degree was calculated. In these different solutions the ratio of monomer:water stayed the same at 55:45 wt%, while the ratio between the monomers was altered (Table 7). The swelling degree was calculated as follows:

$$S_D = \frac{W_s - W_d}{W_d} * 100$$

Table 7: *Swelling degree of P(HEMA-co-METAC) bulk polymers with different ratios of monomers.*

HEMA [wt%]	METAC [wt%]	W_d [mg]	W_s [mg]	S_d [%]
100	0	340	568	154
90	10	284	2268	605
80	20	324	5135	1298
70	30	394	6443	10764
60	40	273	5481	16535
50	50	348	10436	24526

7.3.5 Contact Angle measurements

For these measurements the films were cut in pieces of 0.7x1.2 cm and the top right corner was cut in order to identify the top and bottom side of the films while coating. The samples were rinsed with water and ethanol prior to use. Then they were placed into the reactor with the walls on top. Then the argon supply was attached and 1.5 ml of HEMA/MEDSAH solution was added. The monomer composition and deoxygenation was performed as described in chapter 7.3.3. Then the silica glass was put on top of the reactor. The 400 W or 15 W lamp was then placed above the sample. After the reaction the samples were immersed in water for 24 h in three different baths of water. For contact angle measurements every sample was measured 10 times on different locations and the software *Advance* was used. To measure the contact angle, the sessile drop method as utilized, with a drop volume of 2.0 µl and a dosing velocity of 2.67 µl/s. The fitting method used was *Ellipse (tangent-1)*.

Examination of Deoxygenation

For these reactions the 25 W lamp with d_{ls} = 1.5 cm was used. The results of using a non-deoxygenated solution are shown in Table 8 and the results of using the deoxygenated solution are shown in Table 9.

Table 8: *Results of contact angle measurements while using the 25 W lamp and non-deoxygenated HEMA/MEDSAH solution.*

Irradiation Time [min]	Contact Angle [°]	Deviation
0	87.9	1.8
5	80.4	2.8
10	82.4	3.3
15	65.5	8.0
20	49.3	12.5

Table 9: *Results of contact angle measurements while using the 25 W lamp and deoxygenated HEMA/MEDSAH solution.*

Irradiation Time [min]	Contact Angle [°]	Deviation
0	86.3	4.2
2	71.1	7.9
4	58.6	15.0
6	56.8	6.3
8	47.7	9.2
10	46.7	10.7
12	41.8	5.7

Examination of the two Lamps

The samples were prepared as described preciously in this chapter and only deoxygenated solutions were used. The results for the 25 W lamp are shown in Table 9. The results for the 400 W lamp are shown in Table 10.

Table 10: *Results of contact angle measurements while using the 400 W lamp and deoxygenated HEMA/MEDSAH solution.*

Irradiation Time [s]	Contact Angle [°]	Deviation
0	86.3	4.2
10	81.8	2.2
20	77.3	3.0
30	71.3	4.4
40	66.7	5.0
50	59.2	5.2
60	53.5	4.4
70	48.2	3.7
80	45.1	5.1

Examination of the Irradiation Time

The samples were prepared as described preciously in this chapter and the 400 W lamp was used. To measure the dose, after the reaction a radiometer was place at the same spot as the sample and the dose was measured three times with the same irradiation settings as the sample and a median and standard deviation were calculated. The results are shown in Table 11.

Table 11: *Results of the contact angle measurements while varying the irradiation time, using the 400 W lamp and the deoxygenated HEMA/MEDSAH solution.*

Irradiation Time [s]	Contact Angle [°]	Deviation	Dose [J/cm^2]	Deviation
0	86.3	4.2	0.00	0.00
10	81.8	2.2	1.98	0.02
20	77.3	3.0	3.86	0.01
30	71.3	4.4	5.71	0.04
40	66.7	5.0	7.53	0.05
50	59.2	5.2	9.34	0.06
60	53.5	4.4	11.24	0.21
70	48.2	3.7	13.11	0.01
80	45.1	5.1	14.75	0.13

Examination of the Distance between Sample and Light Source

The samples were prepared as described preciously in this chapter and the 400 W lamp was used. To measure the dose, after the reaction a radiometer was place at the same spot as the sample and the dose was measured 3 times with the same irradiation settings as the sample and a median and standard deviation were calculated. The results are shown in Table 12.

Table 12: *Results of the contact angle measurements while varying the distance between the light source and the sample, using the 400 W lamp and the deoxygenated HEMA/MEDSAH solution.*

Distance Light – Sample [cm]	Contact Angle [°]	Deviation	Dose [J/cm^2]	Deviation
2.4	28.1	4.2	13.51	0.02
3.7	32.8	3.6	12.50	0.03
5.0	55.9	5.5	11.16	0.02
6.3	62.7	5.3	9.74	0.02
7.6	72.9	5.6	8.50	0.02
8.9	75.0	2.8	7.36	0.05
10.2	77.7	4.8	6.58	0.02
11.5	79.8	6.4	5.86	0.03
12.8	84.3	2.8	5.29	0.01
14.1	86.3	3.3	4.76	0.01
15.4	93.8	4.8	4.46	0.02

Comparison between PVDF, P(VDF-TrFE) and P(VDF-TrFE-CTFE)

The PVDF and P(VDF-TrFE-CTFE) films used were cut from purchased films as described earlier in this chapter. The P(VDF-TrFE) film were self-made from its powder as described in chapter 7.3.2. The coating was then performed as described earlier in this chapter, with t_i = 60 s, d_{ls} = 5.0 cm and the 400 W UV lamp. The results are shown in Table 13.

Table 13: *Result of the contact angle measurements of pristine and P(HEMA-co-MEDSAH) coated PVDF, P(VDF-TrFE) and P(VDF-TrFE-CTFE).*

	Contact angle (pristine) [°]	Deviation	Contact angle (coated) [°]	Deviation
PVDF	93.6	2.5	55.9	4.6
P(VDF-CTFE)	97.4	2.3	64.1	3.9
P(VDF-TrFE-CTFE)	89.5	1.2	55.3	3.0

Soxhlet extraction

For the extraction a soxhlet apparatus was filled with 500 ml of methanol. After the film was put in the apparatus, the extraction was performed for 5 d. One extraction cycle took approximately 1 h, so an estimated number of 120 extraction cycles were performed.

7.3.6 Fluorescence spectroscopy

Parts of the measurements were performed by Sebastian Hasselmann at the *Fraunhofer ISC* in Würzburg. For the polymerization a solution of fluorescein O-methacrylate of $5x10^{-4}$ g/ml was produced (to dissolve all the dye, the solution was put in an ultrasonic bath for 60 min at room temperature). This solution was then mixed 1:20 with the HEMA/MEDSAH solution described in chapter 7.3.3. The polymerization was performed with t_i = 60 s and a d_{ls} = 5 cm. then the sample was embedded in *Sylgard 184* and hardened afterwards. This way the sample was embedded in silicone and the silicon was then cut with a scalpel in a way that a small block of silicon contained the cross section of the middle of the sample at its edge. By putting this silicone block to the side, the cross section of the sample was facing downwards and could be measured by the confocal fluorescence microscope.

7.3.7 Dynamic Vapour Sorption (DVS)

The samples for swelling degree measurements of the bulk polymers were fabricated as described in chapter 7.3.4. One of each sample were placed in an aluminium tray. Then the device keeps the temperature at 25 °C while increasing the air humidity from 0-90 % in 10 % steps. In every step all samples were weighted until their weight is constant. At the constant point the swelling degree is calculated as described in chapter 7.3.4. Figure 62 shows the results of the calculated swelling degrees.

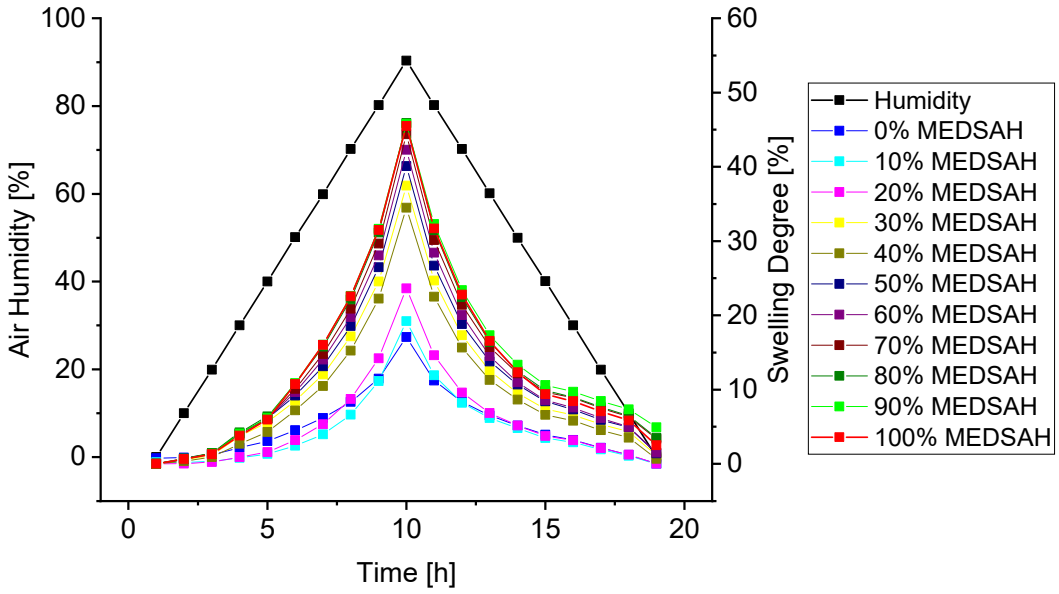

Figure 62: *Measurement of the swelling degree of P(HEMA-co-MEDSAH) bulk polymers with varying MEDSAH ratios with respect to HEMA. Measurement was performed with a dynamic vapour sorption device. Every swelling degree is calculated for the point at which the weight was constant at the respective humidity step.*

To measure the coated films, three samples of every ratio were fabricated to increase the mass of polymer for every aluminium tray. The films were produced t_i = 60 s and d_{ls} = 5 cm. The coating procedure was performed as described in chapter 7.3.5. An aluminium net was plate on top of the samples to prevent a movement of the samples through the constant air exchange of the device. The result of these measurement are shown in Figure 63.

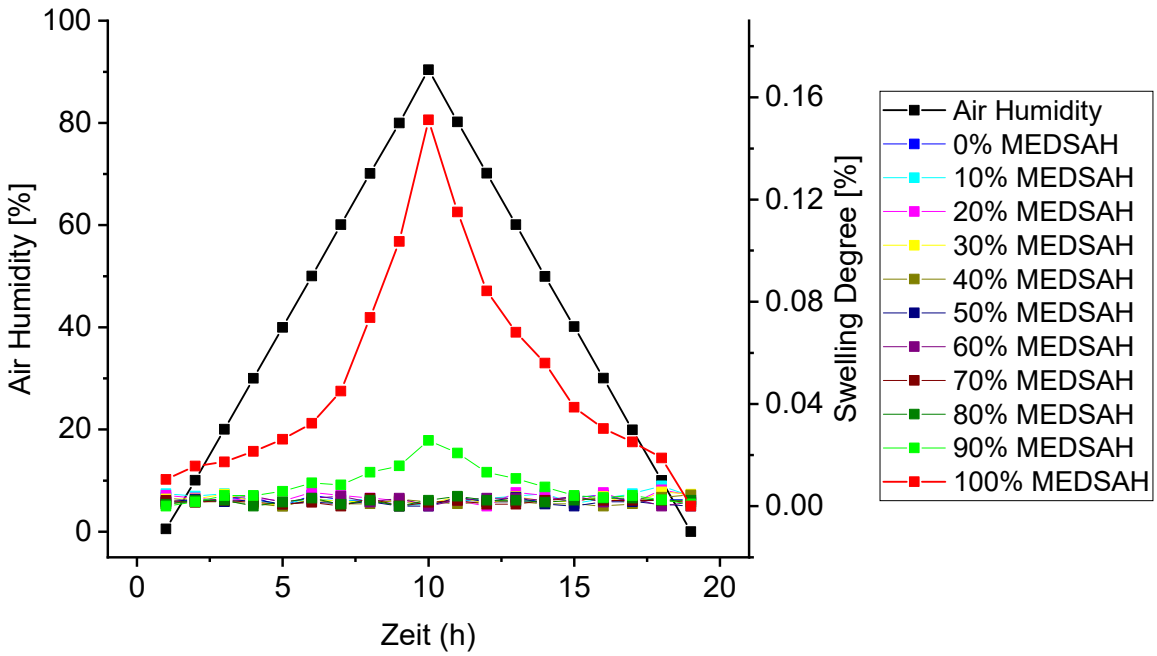

Figure 63: *Measurement of the swelling degree of P(HEMA-co-MEDSAH) coated P(VDF-TrFE-CTDE) films with varying MEDSAH ratios with respect to HEMA. Measurement was performed with a dynamic vapour sorption device. Every swelling degree is calculated for the point at which the weight was constant at the respective humidity step.*

7.3.8 Environmental Scanning Electron Microscope

The samples were prepared as described earlier with only MEDSAH as a monomer. For preparation, the samples were frozen in liquid nitrogen und then broken in the middle by using two flat tweezers. This way a sharp breaking edge was produced. The machine was operated by Andreas Frank at the *University of Bayreuth*, Germany. Figure 64 shows the ESEM images presented in chapter 4.2.2.7 without colouring.

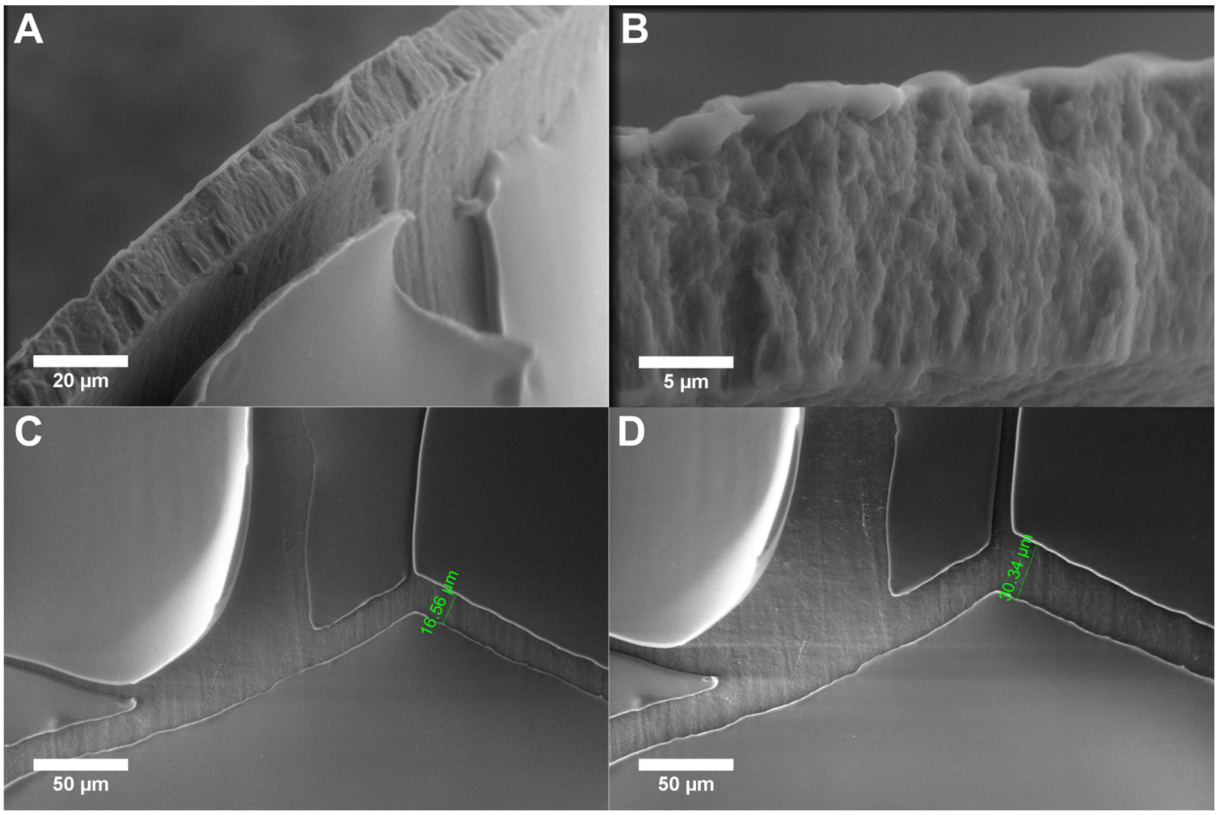

Figure 64: *Environmental SEM images of P(VDF-TrFE-CTFE) films coated with. View at a broken edge of the film (A) with inset (B). Distance of a crack measured on the film with an air humidity of 99.5 % and 2 °C (C) and an air humidity of 42.4 % and 2 °C (D).*

7.3.9 Dynamic SIPGP

The samples of P(VDF-TrFE-CTFE) films for dynamic SIPGP were cut into small pieces of 1.0x0.5 cm and a corner was cut to identify the upper and lower side during the coating procedure. The samples were then rinsed with water and ethanol prior to use. The samples were placed inside the reactor with the walls on top of the samples. Then the argon supply was attached and the silica glass was put on top of the reactor. The monomer solution was filled into a syringe, which was covered with aluminium foil. The syringe, as well as the drain, were connected to the reactor via a polyurethane tube. Then the reactor was filled with monomer solution by turning on the monomer flow via a syringe pump. As soon as the reactor was filled with monomer solution and the flow was constant, the irradiation was started (the irradiation was performed with the HEMA/MEDSAH solution, which was prepared as described in chapter 7.3.3., with

the 400 W lamp, t_i = 60 s and d_{ls} = 5 cm, if not stated otherwise). After the reaction the samples were immersed in water for 24 h in three different baths of water.

Contact Angle

The samples were prepared as described earlier in this chapter. A flowrate of 1-10 ml/min with steps of 1 ml/min was applied. Table 14 shows the results in detail.

Table 14: *Result of the contact angle measurements of P(HEMA-co-MEDSAH) coated P(VDF-TrFE-CTFE) under dynamic conditions with flow rates of 1-10 ml/min.*

Flow Rate [ml/min]	Contact Angle [°]	Deviation
1	48.8	2.5
2	54.4	2.7
3	59.0	2.2
4	65.9	2.4
5	71.1	2.5
6	83.1	2.7
7	83.0	3.3
8	82.09	2.7
9	86.14	2.2
10	86.52	1.4

Cross Section Measurements

The samples were prepared as described earlier in this chapter. The samples were coated with flow rates of 1-5 ml/min. Every sample was measured at the spots on the sides of the cross section (0.0 cm and 1.0 cm) and in the middle of the sample (0.5 cm). Table 15 shows the detailed results.

Table 15: *Result of the contact angle measurements of P(HEMA-co-MEDSAH) coated P(VDF-TrFE-CTFE) under dynamic conditions with flow rates of 1-5 ml/min. The contact angle was measured on three different spots of the cross section of the samples.*

Flow Rate [ml/min]	Contact Angle [°] at 0.0 cm location	Contact Angle [°] at 0.5 cm location	Contact Angle [°] at 1.0 cm location
1	40.6±1.6	39.8±2.6	39.9±2.6
2	51.3±1.5	51.4±1.9	51.5±1.5
3	58.3±1.8	59.6±1.1	58.9±1.7
4	59.7±1.9	71.5±1.5	60.0±2.0
5	58.3±2.4	81.4±1.5	61.6±1.9

Temperature Measurements

For the temperature measurements the samples were prepared as described previously in this chapter. The temperature was measured during the reaction directly behind the sample in the middle of the flow channel with 10 measurements per second. The start (T_0) and end (T_t) point (t_i = 0 s and t_i = 60 s) and the difference between the two (T_t-T_0) are listed in Table 16.

Table 16: *Temperature measurements at 0 s and 60 s of the HEMA/MEDSAH solution during the coating of P(VDF-TrFE-CTFE) films. The warming shows the difference between those two.*

Flow Rate	Temperature 0 s [°C]	Temperature 60 s [°C]	Warming [°C]
0	24.2±0.4	36.7±3.8	12.5
1	24.2±0.3	35.0±2.4	10.8
2	23.7±0.2	32.6±2.2	8.9
3	24.3±0.7	33.3±0.4	9.0
4	23.5±0.9	31.9±1.2	8.4
5	24.5±0.5	32.3±1.0	7.8

Formation of Bulk Polymer SEM

The samples for the SEM images were prepared as described earlier in this chapter. One sample was not coated, one was coated with 2 ml/min and one was coated under static conditions, but was prepared as the samples under dynamic conditions. This

means, that the reactor was filled by the syringe pump until a constant flow inside the reactor. Then the pump was turned out prior to the start of the reaction.

Formation of Bulk Polymer

The samples were prepared as described previously in this chapter with r_{fl} = 1-5 ml/min. Only this time, not the samples were the important part, but the solution after the reaction was. After removing the samples from the reactor, 3 ml of water were added to the solution inside the reactor, because the bulk polymer is transparent right after the reaction, but gets turbid after adding water. This makes the bulk polymer more visible. After adding the water to the solution, the solution was filtered through a 50 µm pore sized filter that was weighted before and the residue was washed with ethanol and water. Then the filters were dried until the weight was constant. Table 17 shows these result in detail.

Table 17: *Results of the measurements of bulk polymer inside the HEMA/MEDSAH solution after filtering with a 50 µm pore sized filter.*

Flow Rate [ml/min]	Filter Tara [mg]	Filter with polymer [mg]	weight of Polymer [mg]
0	270	465	195
1	271	378	107
2	273	306	33
3	270	293	23
4	272	282	10
5	270	291	21

7.3.10 SIPGP on Scaffolds

Printing of the MEW Scaffolds

The MEW printed scaffolds of PVDF and P(VDF-TrFE) were printed by Juliane Kade at the *Department for Functional Materials and Dentistry* (FMZ) in Würzburg. The PCL scaffolds were printed by Ezgi Bakirci at the FMZ. The scaffolds were printed with custom build printers. Table 18 shows the printing parameters and the literature for the printers. The samples were washed with water and ethanol prior to use.

Table 18: *Printing parameters for the used MEW scaffolds. T = Temperature; V = Voltage; Distance = Distance between the print head and the collector; Pressure = overpressure inside the print head.*

Parameters	PVDF	P(VDF-TrFE)	PCL
Needle	26 G	22 G	22G
T_{Needle} [°C]	220	170	-
$T_{Syringe}$ [°C]	220	170	85
$T_{Collector}$ [°C]	-	120	-
Distance [mm]	2.5	4.4	4.5
Pressure [bar]	2.0 (synth. air)	0.5 (N_2)	0.5
V_{Needle} [kV]	1.5	3.7	5.0
$V_{Collector}$ [kV]	-1.5	-	-1.5
Writing velocity [mm/min]	2000	70	1300
Hatch spacing [µm]	1000	500	250
Printer Literature	[73]	[77]	[73]

Fabrication of the Silica Fibres

The silica fibres used were produced by Dr. Bastian Christ at the *Fraunhofer ISC* in Würzburg. The fibres were Electrospun fleeces of $[SiO_x(EOt)_y(OH)_z]_n$ with an estimated silanol content of 5 % prior to coating. The procedure was performed according to literature.[287]

Coating of the Scaffolds

All samples were prepared as described in chapter 7.3.9. The PVDF and P(VDF-TrFE) scaffolds however, were not cut, but printed as 2x2 cm samples and were used as such. The used flow rate was r_{fl} = 0 ml/min for the static SIPGP coatings and r_{fl} = 2 ml/min for the dynamic SIPGP coatings.

7.3.11 Biological properties

RGD Sequences

The RDG and scrambled RGD sequences used were a C_{ter} acrylate modified G-R-G-D-S-P and a C_{ter} acrylate modified G-R-G-E-S-P sequence. The sequences were dissolved in Millipore water with a concentration of 0.1 mg/l. Prior to polymerization the solution was deoxygenated by passing argon for 30 min through the solutions. The coating procedure then was performed as described in chapter 7.3.5.

Cytotoxicity

These measurements were performed by Ezgi Bakirci at the *Department for Functional Materials and Dentistry* (FMZ) in Würzburg. The live/dead staining was performed using the live/dead Assay Cell Staining Kit (*PromoKine*, Heidelberg, Germany) at 1 d and 7 d after seeding 500000 cells per scaffold. The samples were washed twice with PBS before staining solution ($4x10^{-6}$ M ethidium homodimer III and $2x10^{-6}$ M calcein acetoxymethylester in PBS) was added and incubated for 45 min at 37 °C in the dark.

The cell activity on the samples is shown in Figure 65, the cell number in Figure 66 and the cell activity per cell in Figure 67.

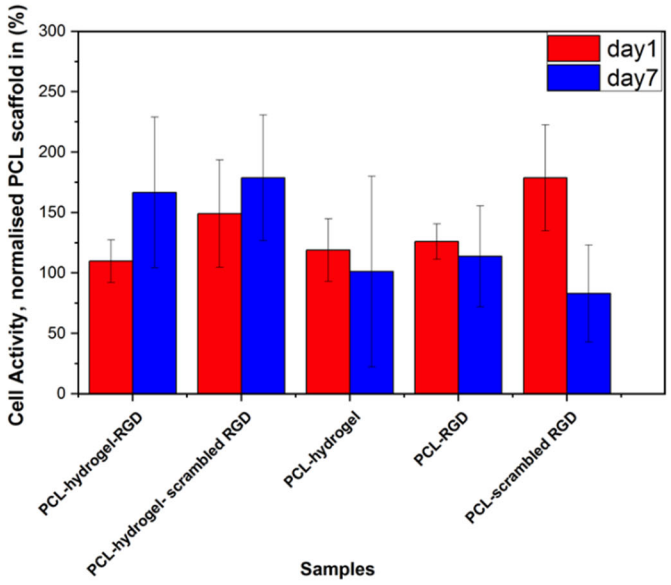

Figure 65: *Cell activity on the measured samples after 1 d and 7 d, The data is normalized to the cell activity of pristine PCL scaffolds (100 %).*

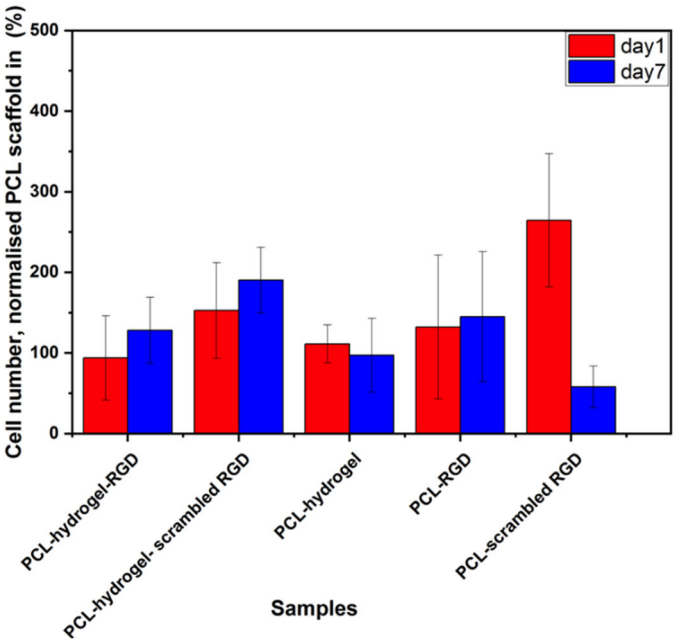

Figure 66: *Cell number on the measured samples after 1 d and 7 d, The data is normalized to the cell number of pristine PCL scaffolds (100 %).*

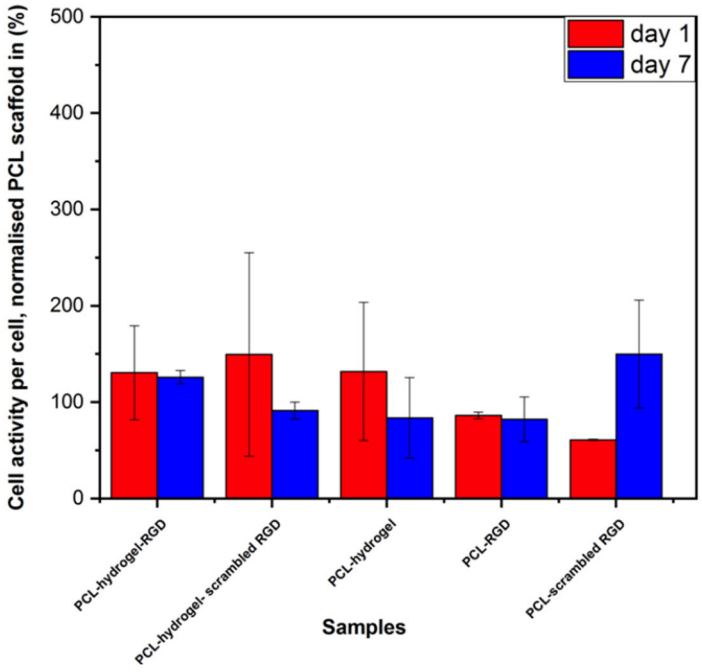

Figure 67: *Cell activity per cell on the measured samples after 1 d and 7 d, The data is normalized to the cell activity per cell of pristine PCL scaffolds (100 %).*

Cell Adhesion

The cell adhesion experiments were performed by Ezgi Bakirci at the Department for Functional Materials and Dentistry (FMZ) in Würzburg. U87 glioblastoma cells were placed on either MEW printed PCL scaffolds with a fibre spacing of 250 µm, or MEW printed PVDF scaffolds with a fibre spacing of 1000 µm. The cell cytoskeleton protein F-actin was stained with phalloidin (red), the membrane-cytoskeletal protein in focal adhesion plaques with vinculin (green) and the cell nucleus with 4´,6-diamidino-2-phenylindole (DAPI) (blue). Briefly, the U87 cells were seeded on the scaffolds (500000 cells per scaffold). At Day 1 and Day3 or 4, the scaffolds were washed with PBS 2 times and fixed with 4% formaldehyde for two hours at room temperature (RT). The samples were washed twice with PBS and incubated in 0.5 % Triton X for 10 min , then washed with PBS two times again. After it was blocked with 1 % bovine serum albumin in PBS for 30 min at 37 °C. Primary antibody against vinculin (1:100) and phalloidin (1:500) were applied overnight at 4 °C. Subsequently, fluorescence-labelled secondary antibody was applied in 1%BSA for 1hour at 37 °C.

8 References

[1] Barski, D.; Arndt, C.; Gerullis, H.; Yang, J.; Boros, M.; Otto, T.; Kolberg, H.-C. *International journal of surgery,* **2017**, *39*, 249–254.

[2] Klinge, U.; Klosterhalfen, B.; Öttinger, A. P.; Junge, K.; Schumpelick, V. *Biomaterials,* **2002**, *23* (16), 3487–3493.

[3] Cho, Y.; Ahn, D.; Park, J. B.; Pak, S.; Lee, S.; Jun, B. O.; Hong, J.; Lee, S. Y.; Jang, J. E.; Hong, J.; Morris, S. M.; Sohn, J. I.; Cha, S. N.; Kim, J. M. *Advanced Electronic Materials,* **2016**, *2* (10), 1600225.

[4] Legrand, J. F. *Ferroelectrics,* **1989**, *91* (1), 303–317.

[5] Wan, C.; Bowen, C. R. *Journal of Materials Chemistry A,* **2017**, *5* (7), 3091–3128.

[6] Malikmammadov, E.; Tanir, T. E.; Kiziltay, A.; Hasirci, V.; Hasirci, N. *Journal of biomaterials science. Polymer edition,* **2018**, *29* (7-9), 863–893.

[7] Bartnikowski, M.; Vaquette, C.; Ivanovski, S. *Clinical oral implants research,* **2020**, *31* (5), 431–441.

[8] Fuchs, A.; Youssef, A.; Seher, A.; Hochleitner, G.; Dalton, P. D.; Hartmann, S.; Brands, R. C.; Müller-Richter, U. D. A.; Linz, C. *BMC oral health,* **2019**, *19* (1), 28.

[9] Florczak, S.; Lorson, T.; Zheng, T.; Mrlik, M.; Hutmacher, D. W.; Higgins, M. J.; Luxenhofer, R.; Dalton, P. D. *Polymer International,* **2019**, *37*, 1079.

[10] Kade, J. C.; Tandon, B.; Weichhold, J.; Pisignano, D.; Persano, L.; Luxenhofer, R.; Dalton, P. D. *ChemRxiv,* **2021**.

[11] WICHTERLE, O.; LÍM, D. *Nature,* **1960**, *185*, 117-118

[12] Ravalico, G.; Baccara, F.; Lovisato, A.; Tognetto, D. *Ophthalmology,* **1997**, *104* (7), 1084–1091.

[13] Higa, O. Z.; Faria, H. A. M.; Queiroz, A. A. de. *Radiation Physics and Chemistry,* **2014**, *98*, 118–123.

[14] Zhu, L.-J.; Zhu, L.-P.; Zhao, Y.-F.; Zhu, B.-K.; Xu, Y.-Y. *Journal of Materials Chemistry A,* **2014**, *2* (37), 15566.

[15] Politakos, N.; Azinas, S.; Moya, S. E. *Macromolecular rapid communications,* **2016**, *37* (7), 662–667.

[16] La Gatta, A.; Schiraldi, C.; Esposito, A.; D'Agostino, A.; Rosa, A. de. *Journal of biomedical materials research. Part A,* **2009**, *90* (1), 292–302.

[17] Deng, J.-P.; Yang, W.-T.; Rånby, B. *Macromolecular Rapid Communications,* **2001**, *22* (7), 535–538.

[18] Wengler, A.; Nimptsch, U.; Mansky, T. *Deutsches Ärzteblatt international,* **2014**, *111* (23-24), 407–416.

[19] Healy, W. L.; Iorio, R.; Clair, A. J.; Pellegrini, V. D.; Della Valle, C. J.; Berend, K. R. *Clinical orthopaedics and related research,* **2016**, *474* (2), 357–364.

[20] Healy, W. L.; Della Valle, C. J.; Iorio, R.; Berend, K. R.; Cushner, F. D.; Dalury, D. F.; Lonner, J. H. *Clinical orthopaedics and related research,* **2013**, *471* (1), 215–220.

[21] Wisbey, A.; Gregson, P. J.; Tuke, M. *Biomaterials,* **1987**, *8* (6), 477–480.

[22] Bergemann, C.; Zaatreh, S.; Wegner, K.; Arndt, K.; Podbielski, A.; Bader, R.; Prinz, C.; Lembke, U.; Nebe, J. B. *World journal of transplantation,* **2017**, *7* (3), 193–202.

[23] Camargo, S. E. A.; Roy, T.; Carey Iv, P. H.; Fares, C.; Ren, F.; Clark, A. E.; Esquivel-Upshaw, J. F. *Journal of functional biomaterials,* **2020**, *11* (2).

[24] Veronesi, F.; Giavaresi, G.; Fini, M.; Longo, G.; Ioannidu, C. A.; Scotto d'Abusco, A.; Superti, F.; Panzini, G.; Misiano, C.; Palattella, A.; Selleri, P.; Di Girolamo, N.; Garbarino, V.; Politi, L.; Scandurra, R. *Materials science & engineering. C, Materials for biological applications,* **2017**, *70* (Pt 1), 264–271.

[25] Ni, S.; Chang, J.; Chou, L.; Zhai, W. *Journal of biomedical materials research. Part B, Applied biomaterials,* **2007**, *80* (1), 174–183.

[26] Sarmento, C.; Luklinska, Z. B.; Brown, L.; Anseau, M.; Aza, P. N. de; Aza, S. de; Hughes, F. J.; McKay, I. J. *Journal of biomedical materials research. Part A,* **2004**, *69* (2), 351–358.
[27] Ducheyne, P.; van Raemdonck, W.; Heughebaert, J. C.; Heughebaert, M. *Biomaterials,* **1986**, *7* (2), 97–103.
[28] Bi, Q.; Song, X.; Chen, Y.; Zheng, Y.; Yin, P.; Lei, T. *Colloids and surfaces. B, Biointerfaces,* **2020**, *189*, 110813.
[29] Jaafar, A.; Hecker, C.; Árki, P.; Joseph, Y. *Bioengineering,* **2020**, *7* (4).
[30] Lu, X.; Wang, Y.; Liu, Y.; Wang, J.; Qu, S.; Feng, B.; Weng, J. *Materials Letters,* **2007**, *61* (18), 3970–3973.
[31] Khalid, M.; Mujahid, M.; Khan, A. N.; Rawat, R. S.; Salam, I.; Mehmood, K. *Key Engineering Materials,* **2012**, *510-511*, 547–553.
[32] Fatehi, K.; Moztarzadeh, F.; Solati-Hashjin, M.; Tahriri, M.; Rezvannia, M.; Saboori, A. *Surface Engineering,* **2009**, *25* (8), 583–588.
[33] Dinh, T. M. T.; Nguyen, T. T.; Pham, T. N.; Nguyen, T. P.; Nguyen, T. T. T.; Hoang, T.; Grossin, D.; Bertrand, G.; Drouet, C. *Advances in Natural Sciences: Nanoscience Nanotechnology,* **2016**, *7* (2), 25008.
[34] Gunawarman; Nuswantoro, N. F.; Juliadmi, D.; Fajri, H.; Budiman, A.; Tjong, D. H.; Manjas, M. *IOP Conf. Ser.: Materials Sciences and Engineering,* **2019**, *602*, 12071.
[35] Krause, A.; Höh, N. von der; Bormann, D.; Krause, C.; Bach, F.-W.; Windhagen, H.; Meyer-Lindenberg, A. *Journal of Materials Sciences,* **2010**, *45* (3), 624–632.
[36] Thomann, M.; Krause, C.; Angrisani, N.; Bormann, D.; Hassel, T.; Windhagen, H.; Meyer-Lindenberg, A. *Journal of biomedical materials research. Part A,* **2010**, *93* (4), 1609–1619.
[37] Rammelt, S.; Schulze, E.; Bernhardt, R.; Hanisch, U.; Scharnweber, D.; Worch, H.; Zwipp, H.; Biewener, A. *Journal of orthopaedic research : official publication of the Orthopaedic Research Society,* **2004**, *22* (5), 1025–1034.
[38] Diefenbeck, M.; Schrader, C.; Gras, F.; Mückley, T.; Schmidt, J.; Zankovych, S.; Bossert, J.; Jandt, K. D.; Völpel, A.; Sigusch, B. W.; Schubert, H.; Bischoff, S.; Pfister, W.; Edel, B.; Faucon, M.; Finger, U. *Biomaterials,* **2016**, *101*, 156–164.
[39] Schmidmair, G.; Wildemann, B.; Stemberger, A.; Haas, N. P.; Raschke, M.
[40] Liu, Y.; Deng, K.; Wang, S.; Xiao, M.; Han, D.; Meng, Y. *Polymer Chemistry,* **2015**, *6* (11), 2076–2083.
[41] Athanasiou, K. A.; Agrawal, C. M.; Barber, F. A.; Burkhart, S. S. *Arthroscopy: The Journal of Arthroscopic & Related Surgery,* **1998**, *14* (7), 726–737.
[42] Gilding, D. K.; Reed, A. M. *Polymer,* **1979**, *20* (12), 1459–1464.
[43] Díaz, E.; Sandonis, I.; Valle, M. B. *Journal of Nanomaterials,* **2014**, *2014*, 1–8.
[44] Gleadall, A.; Pan, J.; Kruft, M.-A.; Kellomäki, M. *Acta biomaterialia,* **2014**, *10* (5), 2223–2232.
[45] Gleadall, A.; Pan, J.; Kruft, M.-A.; Kellomäki, M. *Acta biomaterialia,* **2014**, *10* (5), 2233–2240.
[46] Fialho, S. L.; Behar-Cohen, F.; Silva-Cunha, A. *European journal of pharmaceutics and biopharmaceutics : official journal of Arbeitsgemeinschaft für Pharmazeutische Verfahrenstechnik e.V,* **2008**, *68* (3), 637–646.
[47] Salmoria, G. V.; Cardenuto, M. R.; Roesler, C.; Zepon, K. M.; Kanis, L. A. *Procedia CIRP,* **2016**, *49*, 188–192.
[48] Chou, P.-Y.; Chou, Y.-C.; Lai, Y.-H.; Lin, Y.-T.; Lu, C.-J.; Liu, S.-J. *Polymers,* **2021**, *13* (3).
[49] Li, C.; Cheng, L.; Zhang, Y.; Guo, S.; Wu, W. *International journal of pharmaceutics,* **2010**, *386* (1-2), 23–29.

[50] Xue, J.; He, M.; Liang, Y.; Crawford, A.; Coates, P.; Chen, D.; Shi, R.; Zhang, L. *Journal of Materials Chemistry B,* **2014**, *2* (39), 6867–6877.
[51] Bernstein, M.; Gotman, I.; Makarov, C.; Phadke, A.; Radin, S.; Ducheyne, P.; Gutmanas, E. Y. *Advanced Engineering Materials,* **2010**, *12* (8), B341-B347.
[52] Catauro, M.; Bollino, F.; Papale, F.; Piccolella, S.; Pacifico, S. *Materials science & engineering. C, Materials for biological applications,* **2016**, *58*, 945–952.
[53] Chen, J.; Tu, C.; Tang, X.; Li, H.; Yan, J.; Ma, Y.; Wu, H.; Liu, C. *Stem cell research & therapy,* **2019**, *10* (1), 379.
[54] Doyle, S. E.; Henry, L.; McGennisken, E.; Onofrillo, C.; Di Bella, C.; Duchi, S.; O'Connell, C. D.; Pirogova, E. *Polymers,* **2021**, *13* (2).
[55] Song, W.; Yu, X.; Markel, D. C.; Shi, T.; Ren, W. *Biofabrication,* **2013**, *5* (3), 35006.
[56] Zumbrunn, T.; Varadarajan, K. M.; Rubash, H. E.; Malchau, H.; Li, G.; Muratoglu, O. K. *The Journal of arthroplasty,* **2015**, *30* (12), 2143–2148.
[57] Ishii, Y.; Noguchi, H.; Sato, J.; Sakurai, T.; Toyabe, S.-I. *Knee surgery, sports traumatology, arthroscopy : official journal of the ESSKA,* **2017**, *25* (12), 3711–3717.
[58] Boia, R.; Dias, P. A. N.; Martins, J. M.; Galindo-Romero, C.; Aires, I. D.; Vidal-Sanz, M.; Agudo-Barriuso, M.; Sousa, H. C. de; Ambrósio, A. F.; Braga, M. E. M.; Santiago, A. R. *Journal of controlled release : official journal of the Controlled Release Society,* **2019**, *316*, 331–348.
[59] Häusler, E.; Stein, L.; Harbauer, G. *Ferroelectrics,* **1984**, *60* (1), 277–282.
[60] Liu, H.; Zhao, T.; Jiang, W.; Jia, R.; Niu, D.; Qiu, G.; Fan, L.; Li, X.; Liu, W.; Chen, B.; Shi, Y.; Yin, L.; Lu, B. *Advanced Functional Materials,* **2015**, *25* (45), 7071–7079.
[61] Tjong, S. C. *Express Polymer Letters* **2018**, *12* (5), 395.
[62] Han, M.; Wang, H.; Yang, Y.; Liang, C.; Bai, W.; Yan, Z.; Li, H.; Xue, Y.; Wang, X.; Akar, B.; Zhao, H.; Luan, H.; Lim, J.; Kandela, I.; Ameer, G. A.; Zhang, Y.; Huang, Y.; Rogers, J. A. *Nature Electronics,* **2019**, *2* (1), 26–35.
[63] Park, S.; Guan, X.; Kim, Y.; Creighton, F. P. X.; Wei, E.; Kymissis, I. J.; Nakajima, H. H.; Olson, E. S. *Trends in hearing,* **2018**, *22*, 2331216518774450.
[64] Laroche, G.; Marois, Y.; Guidoin, R.; King, M. W.; Martin, L.; How, T.; Douville, Y. *Journal of biomedical materials research,* **1995**, *29* (12), 1525–1536.
[65] Klink, C. D.; Junge, K.; Binnebösel, M.; Alizai, H. P.; Otto, J.; Neumann, U. P.; Klinge, U. *Journal of investigative surgery : the official journal of the Academy of Surgical Research,* **2011**, *24* (6), 292–299.
[66] Sánchez-Arteaga, A.; Tallón-Aguilar, L.; Tinoco-González, J.; Perea Del-Pozo, E.; Navas-Cuellar, A.; Padillo-Ruíz, J. *Hernia : the journal of hernias and abdominal wall surgery,* **2021**, *25* (1), 99–106.
[67] Houis, S.; Engelhardt, E. M.; Wurm, F.; Gries, T. *Medical and Healthcare Textiles*, **2010**, 342–352.
[68] Chu, B.; Neese, B.; Lin, M.; Lu, S.; Zhang, Q. M. *Applied Physics Letters,* **2008**, *93* (15), 152903.
[69] Nunes-Pereira, J.; Ribeiro, S.; Ribeiro, C.; Gombek, C. J.; Gama, F. M.; Gomes, A. C.; Patterson, D. A.; Lanceros-Méndez, S. *Polymer Testing,* **2015**, *44*, 234–241.
[70] Wang, A.; Liu, Z.; Hu, M.; Wang, C.; Zhang, X.; Shi, B.; Fan, Y.; Cui, Y.; Li, Z.; Ren, K. *Nano Energy,* **2018**, *43*, 63–71.
[71] Li, Y.; Liao, C.; Tjong, S. C. *Nanomaterials,* **2019**, *9* (7), 952.
[72] Della Schiava, N.; Pedroli, F.; Thetpraphi, K.; Flocchini, A.; Le, M.-Q.; Lermusiaux, P.; Capsal, J.-F.; Cottinet, P.-J. *Scientific reports,* **2020**, *10* (1), 8805.
[73] Brown, T. D.; Dalton, P. D.; Hutmacher, D. W. *Advanced materials,* **2011**, *23* (47), 5651–5657.
[74] Hrynevich, A.; Elçi, B. Ş.; Haigh, J. N.; McMaster, R.; Youssef, A.; Blum, C.; Blunk, T.; Hochleitner, G.; Groll, J.; Dalton, P. D. *Small,* **2018**, *14* (22), e1800232.

[75] Hochleitner, G.; Fürsattel, E.; Giesa, R.; Groll, J.; Schmidt, H.-W.; Dalton, P. D. *Macromolecular rapid communications,* **2018**, *39* (10), e1800055.
[76] Hochleitner, G.; Hümmer, J. F.; Luxenhofer, R.; Groll, J. *Polymer,* **2014**, *55* (20), 5017–5023.
[77] Haigh, J. N.; Dargaville, T. R.; Dalton, P. D. *Materials science & engineering. C, Materials for biological applications,* **2017**, *77*, 883–887.
[78] Heuts, J.; Salber, J.; Goldyn, A. M.; Janser, R.; Möller, M.; Klee, D. *Journal of biomedical materials research. Part A,* **2010**, *92* (4), 1538–1551.
[79] Zhang, S.; Cao, J.; Ma, N.; You, M.; Wang, X.; Meng, J. *Applied Surface Science,* **2018**, *428*, 41–53.
[80] Wu, L.; Lin, Q.; Liu, C.; Chen, W. *Polymers,* **2019**, *11* (12), 1975.
[81] Chanachai, A.; Meksup, K.; Jiraratananon, R. *Separation and Purification Technology,* **2010**, *72* (2), 217–224.
[82] Sydow, S.; Cassan, D. de; Hänsch, R.; Gengenbach, T. R.; Easton, C. D.; Thissen, H.; Menzel, H. *Biomaterials science,* **2018**, *7* (1), 233–246.
[83] Croisier, F.; Atanasova, G.; Poumay, Y.; Jérôme, C. *Advanced healthcare materials,* **2014**, *3* (12), 2032–2039.
[84] Refojo, M. F.; Yasuda, H. *Journal of Applied Polymer Sciences,* **1965**, *9* (7), 2425–2435.
[85] Ratner, B. D.; Weathersby, P. K.; Hoffman, A. S.; Kelly, M. A.; Scharpen, L. H. *J. Applied Polymer Sciences,* **1978**, *22* (3), 643–664.
[86] Andrade J. D.; King R. N.; Gregonis D. E.; Coleman D. L. *Journal of Polymer Science, C Polymer Symposia,* **1979**, *66* (1), 313–336.
[87] Xu, J.; Stangel, I.; Butler, I. S.; Gilson, D. F. *Journal of Dental Research,* **1997**, *76* (1), 596–601.
[88] Ciolino, J. B.; Hoare, T. R.; Iwata, N. G.; Behlau, I.; Dohlman, C. H.; Langer, R.; Kohane, D. S. *Investigative ophthalmology & visual science,* **2009**, *50* (7), 3346–3352.
[89] McGinty, K. M.; Brittain, W. J. *Polymer,* **2008**, *49* (20), 4350–4357.
[90] Lee, W.-F.; Lai, C.-C. *Journal of Applied Polymer Science,* **1998**, *67* (2), 307–319.
[91] Giglio, E. de; Cometa, S.; Ricci, M. A.; Cafagna, D.; Savino, A. M.; Sabbatini, L.; Orciani, M.; Ceci, E.; Novello, L.; Tantillo, G. M.; Mattioli-Belmonte, M. *Acta biomaterialia,* **2011**, *7* (2), 882–891.
[92] Hanak, B. W.; Hsieh, C.-Y.; Donaldson, W.; Browd, S. R.; Lau, K. K. S.; Shain, W. *Journal of biomedical materials research. Part B, Applied biomaterials,* **2018**, *106* (3), 1268–1279.
[93] Jhaveri, S. J.; Hynd, M. R.; Dowell-Mesfin, N.; Turner, J. N.; Shain, W.; Ober, C. K. *Biomacromolecules,* **2009**, *10* (1), 174–183.
[94] Wu, L.; Brazel, C. S. *International journal of pharmaceutic,s* **2008**, *349* (1-2), 1–10.
[95] Chouhan, R.; Bajpai, A. *Journal of nanobiotechnology,* **2009**, *7*, 5.
[96] Tsukada, M. *Journal of Applied Polymer Science,* **1988**, *35* (8), 2133–2140.
[97] Wang, J.; Ma, X.; Wei, L.; Zhu, X.; Zhu, Y.; Wang, G.; Mei, T.; Li, J.; Wang, X. *Colloid Polymer Science,* **2018**, *296* (4), 745–752.
[98] Boztas, A. O.; Guiseppi-Elie, A. *Biomacromolecules,* **2009**, *10* (8), 2135–2143.
[99] Ojha, U.; Feng, D.; Chandekar, A.; Whitten, J. E.; Faust, R. *Langmuir : the ACS journal of surfaces and colloids,* **2009**, *25* (11), 6319–6327.
[100] Villa-Diaz, L. G.; Nandivada, H.; Ding, J.; Nogueira-de-Souza, N. C.; Krebsbach, P. H.; O'Shea, K. S.; Lahann, J.; Smith, G. D. *Nature biotechnology,* **2010**, *28* (6), 581–583.
[101] Villa-Diaz, L. G.; Brown, S. E.; Liu, Y.; Ross, A. M.; Lahann, J.; Parent, J. M.; Krebsbach, P. H. *Stem cells,* **2012**, *30* (6), 1174–1181.

[102] Ross, A. M.; Nandivada, H.; Ryan, A. L.; Lahann, J. *Polymer,* **2012**, *53* (13), 2533–2539.
[103] Nandivada, H.; Villa-Diaz, L. G.; O'Shea, K. S.; Smith, G. D.; Krebsbach, P. H.; Lahann, J. *Nature protocols,* **2011**, *6* (7), 1037–1043.
[104] Azarin, S. M.; Palecek, S. P. *Cell stem cell,* **2010**, *7* (1), 7–8.
[105] Villa-Diaz, L. G.; Kim, J. K.; Lahann, J.; Krebsbach, P. H. *Stem cells translational medicine,* **2014**, *3* (12), 1410–1417.
[106] Yang, Z.; Saeki, D.; Wu, H.-C.; Yoshioka, T.; Matsuyama, H. *Journal of Membrane Science,* **2019**, *582*, 111–119.
[107] Yang, Z.; Zhang, X.; Xie, M.; Wu, H.-C.; Yoshioka, T.; Saeki, D.; Matsuyama, H. *Journal of Membrane Science,* **2020**, *614*, 118515.
[108] Yang, Z.; Zhang, S.; Tarabara, V. V.; Bruening, M. L. *Macromolecules,* **2018**, *51* (3), 1161–1171.
[109] Wang, H.; Akcora, P. *Colloids and surfaces. B, Biointerfaces,* **2017**, *160*, 215–219.
[110] Cho, W. K.; Kong, B.; Choi, I. S. *Langmuir : the ACS journal of surfaces and colloids,* **2007**, *23* (10), 5678–5682.
[111] Sun, J.-T.; Yu, Z.-Q.; Hong, C.-Y.; Pan, C.-Y. *Macromolecular rapid communications,* **2012**, *33* (9), 811–818.
[112] Qian, X.; Villa-Diaz, L. G.; Kumar, R.; Lahann, J.; Krebsbach, P. H. *Biomaterials,* **2014**, *35* (36), 9581–9590.
[113] Wang, Z.; Fei, G.; Xia, H.; Zuilhof, H. *Journal of materials chemistry. B,* **2018**, *6* (43), 6930–6935.
[114] Venkidasubramonian, G.; Kratzer, D.; Trouillet, V.; Zydziak, N.; Franzreb, M.; Barner, L.; Lahann, J. *Polymer,* **2018**, *150*, 26–34.
[115] Zhou, J.; Ye, L.; Lin, Y.; Wang, L.; Li Zhou; Hu, H.; Zhang, Q.; Yang, H.; Luo, Z. *Journal of Applied Polymer Science,* **2019**, *136* (24), 47653.
[116] Azzaroni, O.; Brown, A. A.; Huck, W. T. S. *Angewandte Chemie* **2006**, *118* (11), 1802–1806.
[117] Lim, C.-M.; Hur, J.; Jang, H.; Seo, J.-H. *Acta biomaterialia,* **2019**, *85*, 180–191.
[118] Lim, C.-M.; Seo, J.; Jang, H.; Seo, J.-H. *Applied Surface Science,* **2018**, *452*, 102–112.
[119] Osaheni, A. O.; Mather, P. T.; Blum, M. M. *Materials science & engineering. C, Materials for biological applications,* **2020**, *111*, 110736.
[120] Farhan, T.; Azzaroni, O.; Huck, W. T. S. *Soft matter,* **2005**, *1* (1), 66–68.
[121] Osborne, V. L.; Jones, D. M.; Huck, W. T. S. *Chemical communications,* **2002** (17), 1838–1839.
[122] Rosso, F.; Barbarisi, A.; Barbarisi, M.; Petillo, O.; Margarucci, S.; Calarco, A.; Peluso, G. *Materials Science and Engineering: C,* **2003**, *23* (3), 371–376.
[123] Kim, S.; English, A. E.; Kihm, K. D. *Acta biomaterialia,* **2009**, *5* (1), 144–151.
[124] Dong, R.; Molloy, R. P.; Lindau, M.; Ober, C. K. *Biomacromolecules,* **2010**, *11* (8), 2027–2032.
[125] Zhou, Z.; Yu, P.; Geller, H. M.; Ober, C. K. *Biomacromolecules,* **2013**, *14* (2), 529–537.
[126] Chowdhury, P.; Mondal, P.; Roy, K. *Polymer Bulletin,* **2010**, *64* (4), 351–362.
[127] Li, Z.; Zhang, Y.; Lu, D.; Liu, Z. *Journal of Applied Polymer Science,* **2015**, *132* (39), 42596.
[128] Vilela, C.; Oliveira, H.; Almeida, A.; Silvestre, A. J. D.; Freire, C. S. R. *Carbohydrate polymers,* **2019**, *217*, 207–216.
[129] Oh, Y. J.; Khan, E. S.; Del Campo, A.; Hinterdorfer, P.; Li, B. *ACS applied materials & interfaces,* **2019**, *11* (32), 29312–29319.

[130] Chen, L.; Li, P.; Lu, X.; Wang, S.; Zheng, Z. *Faraday discussions,* **2019**, *219* (0), 189–202.
[131] Kumar, N.; Banerjee, C.; Jagadevan, S. *Energy Reports,* **2020**, *6*, 2803–2815.
[132] Zhang, K.; Simic, R.; Spencer, N. D. *Biotribology,* **2021**, 100161.
[133] Wang, J.-S.; Matyjaszewski, K. *Journal of American Chemical Society,* **1995** (117), 5614–5615.
[134] Sarbu, T.; Matyjaszewski, K. *Macromolecular Chemistry and Physics,* **2001**, *202* (17), 3379–3391.
[135] Charvet, R.; Novak, B. M. *Macromolecules,* **2004**, *37* (23), 8808–8811.
[136] Ma, H.; Hyun, J.; Stiller, P.; Chilkoti, A. *Advanced Materials,* **2004**, *16* (4), 338–341.
[137] Min, K.; Gao, H.; Matyjaszewski, K. *Journal of the American Chemical Society,* **2005**, *127* (11), 3825–3830.
[138] Mandal, J.; Varunprasaath, R. S.; Yan, W.; Divandari, M.; Spencer, N. D.; Dübner, M. *RSC Advances,* **2018**, *8* (36), 20048–20055.
[139] Matyjaszewski, K.; Dong, H.; Jakubowski, W.; Pietrasik, J.; Kusumo, A. *ACS Journal of Surfaces and Colloids,* **2007**, *23* (8), 4528–4531.
[140] Siegwart, D. J.; Oh, J. K.; Matyjaszewski, K. *Progress in Polymer Science,* **2012**, *37* (1), 18–37.
[141] Hui, C. M.; Pietrasik, J.; Schmitt, M.; Mahoney, C.; Choi, J.; Bockstaller, M. R.; Matyjaszewski, K. *Chemistry of Materials,* **2014**, *26* (1), 745–762.
[142] Yan, J.; Kristufek, T.; Schmitt, M.; Wang, Z.; Xie, G.; Dang, A.; Hui, C. M.; Pietrasik, J.; Bockstaller, M. R.; Matyjaszewski, K. *Macromolecules,* **2015**, *48* (22), 8208–8218.
[143] Matyjaszewski, K. *Macromolecules,* **2012**, *45* (10), 4015–4039.
[144] Yan, J.; Pan, X.; Wang, Z.; Zhang, J.; Matyjaszewski, K. *Macromolecules,* **2016**, *49* (23), 9283–9286.
[145] Michl, T. D.; Giles, C.; Mocny, P.; Futrega, K.; Doran, M. R.; Klok, H.-A.; Griesser, H. J.; Coad, B. R. *Biointerphases,* **2017**, *12* (5), 05G602.
[146] Gao, H.; Matyjaszewski, K. *Journal of the American Chemical Society,* **2007**, *129* (20), 6633–6639.
[147] Osborne, V. L.; Jones, D. M.; Huck, W. T. S. *Chemical Communications Journal,* **2002** (17), 1838–1839.
[148] Liu, P.; Su, Z. *Polymer International,* **2005**, *54* (11), 1508–1511.
[149] Mrabet, B.; Nguyen, M. N.; Majbri, A.; Mahouche, S.; Turmine, M.; Bakhrouf, A.; Chehimi, M. M. *Surface Science,* **2009**, *603* (16), 2422–2429.
[150] Lei, Z.; Ren, N.; Li, Y.; Li, N.; Mu, B. *Journal of agricultural and food chemistry,* **2009**, *57* (4), 1544–1549.
[151] Ren, X.; Wu, Y.; Cheng, Y.; Ma, H.; Wei, S. *ACS Journal of Surfaces and Colloids,* **2011**, *27* (19), 12069–12073.
[152] Pop-Georgievski, O.; Rodriguez-Emmenegger, C.; Pereira, A. d. l. S.; Proks, V.; Brynda, E.; Rypáček, F. *Journal of Materials Chemistry B,* **2013**, *1* (22), 2859.
[153] Gualandi, C.; Vo, C. D.; Focarete, M. L.; Scandola, M.; Pollicino, A.; Di Silvestro, G.; Tirelli, N. *Macromolecular Rapid Communications,* **2013**, *34* (1), 51–56.
[154] Baek, S.; Green, R.; Granville, A.; Martens, P.; Poole-Warren, L. *Journal of Materials Chemistry. B,* **2013**, *1* (31), 3803–3810.
[155] Matyjaszewski, K.; Pintauer, T.; Gaynor, S. *Macromolecules,* **2000**, *33* (4), 1476–1478.
[156] Honigfort, M. E.; Brittain, W. J.; Bosanac, T.; Wilcox, C. S. *Macromolecules,* **2002**, *35* (13), 4849–4851.
[157] Honigfort, M. E.; Brittain, W. J. *Macromolecules,* **2003**, *36* (9), 3111–3114.
[158] Nasser-Eddine, M.; Delaite, C.; Dumas, P.; Vataj, R.; Louati, A. *Macromolecular Materials Engineering,* **2004**, *289* (2), 204–207.

[159] Barner-Kowollik, C. *Handbook of RAFT Polymerization*, **2008**.
[160] Barner-Kowollik, C.; Davis, T. P.; Heuts, J. P. A.; Stenzel, M. H.; Vana, P.; Whittaker, M. *Journal of Polymer Science A: Polymer Chemisrty,* **2003**, *41* (3), 365–375.
[161] Moad, G.; Chiefari, J.; Chong, Y.; Krstina, J.; Mayadunne, R. T.; Postma, A.; Rizzardo, E.; Thang, S. H. *Polymer International,* **2000**, *49* (9), 993–1001.
[162] Chong, Y. K.; Krstina, J.; Le, T. P. T.; Moad, G.; Postma, A.; Rizzardo, E.; Thang, S. H. *Macromolecules,* **2003**, *36* (7), 2256–2272.
[163] Barsbay, M.; Güven, O.; Stenzel, M. H.; Davis, T. P.; Barner-Kowollik, C.; Barner, L. *Macromolecules,* **2007**, *40* (20), 7140–7147.
[164] Chong, Y. K.; Le, T. P. T.; Moad, G.; Rizzardo, E.; Thang, S. H. *Macromolecules,* **1999**, *32* (6), 2071–2074.
[165] Mayadunne, R. T. A.; Rizzardo, E.; Chiefari, J.; Krstina, J.; Moad, G.; Postma, A.; Thang, S. H. *Macromolecules,* **2000**, *33* (2), 243–245.
[166] Chiefari, J.; Chong, Y. K.; Ercole, F.; Krstina, J.; Jeffery, J.; Le, T. P. T.; Mayadunne, R. T. A.; Meijs, G. F.; Moad, C. L.; Moad, G.; Rizzardo, E.; Thang, S. H. *Macromolecules,* **1998**, *31* (16), 5559–5562.
[167] Darling, T. R.; Davis, T. P.; Fryd, M.; Gridnev, A. A.; Haddleton, D. M.; Ittel, S. D.; Matheson, R. R.; Moad, G.; Rizzardo, E. *Journal of Polymer Science A: Polymer Chemistry,* **2000**, *38* (10), 1706–1708.
[168] Tsujii, Y.; Ejaz, M.; Sato, K.; Goto, A.; Fukuda, T. *Macromolecules,* **2001**, *34* (26), 8872–8878.
[169] Park, J.-W.; Thomas, E. L. *Journal of the American Chemical Society,* **2002**, *124* (4), 514–515.
[170] Ranjan, R.; Brittain, W. J. *Macromolencular Rapid Communications,* **2007**, *28* (21), 2084–2089.
[171] Wu, D.; Song, X.; Tang, T.; Zhao, H. *Journal of Polymer Science A: Polymer Chemistry,* **2010**, *48* (2), 443–453.
[172] Roy, D.; Guthrie, J. T.; Perrier, S. *Macromolecules,* **2005**, *38* (25), 10363–10372.
[173] Hua, D.; Tang, J.; Cheng, J.; Deng, W.; Zhu, X. *Carbohydrate polymers,* **2008**, *73* (1), 98–104.
[174] De, P.; Li, M.; Gondi, S. R.; Sumerlin, B. S. *Journal of the American Chemical Society,* **2008**, *130* (34), 11288–11289.
[175] Li, M.; Li, H.; De, P.; Sumerlin, B. S. *Macromolecular rapid communications,* **2011**, *32* (4), 354–359.
[176] Sumerlin, B. S. *ACS Macro Letters,* **2012**, *1* (1), 141–145.
[177] Zammarelli, N.; Luksin, M.; Raschke, H.; Hergenröder, R.; Weberskirch, R. *ACS Journal of Surfaces and Colloids,* **2013**, *29* (41), 12834–12843.
[178] Zamfir, M.; Rodriguez-Emmenegger, C.; Bauer, S.; Barner, L.; Rosenhahn, A.; Barner-Kowollik, C. *Journal of Materials Chemistry B,* **2013**, *1* (44), 6027–6034.
[179] Shanmugam, S.; Xu, J.; Boyer, C. *Macromolecules,* **2014**, *47* (15), 4930–4942.
[180] Tucker, B. S.; Coughlin, M. L.; Figg, C. A.; Sumerlin, B. S. *ACS Macro Letters,* **2017**, *6* (4), 452–457.
[181] Talelli, M.; Oliveira, S.; Rijcken, C. J. F.; Pieters, E. H. E.; Etrych, T.; Ulbrich, K.; van Nostrum, R. C. F.; Storm, G.; Hennink, W. E.; Lammers, T. *Biomaterials,* **2013**, *34* (4), 1255–1260.
[182] Huang, X.; Hu, J.; Li, Y.; Xin, F.; Qiao, R.; Davis, T. P. *Biomacromolecules,* **2019**, *20* (12), 4243–4257.
[183] Huang, Z.; Zhang, X.; Zhang, X.; Wang, S.; Yang, B.; Wang, K.; Yuan, J.; Tao, L.; Wei, Y. *Polymer Bulletin,* **2017**, *74* (11), 4525–4536.
[184] Zhang, Z.; Corrigan, N.; Bagheri, A.; Jin, J.; Boyer, C. *Angewandte Chemie,* **2019**, *131* (50), 18122–18131.

[185] Hu, J.; Qiao, R.; Whittaker, M. R.; Quinn, J. F.; Davis, T. P. *Australian Journal of Chemistry,* **2017**, *70* (11), 1161.
[186] Fairbanks, B. D.; Gunatillake, P. A.; Meagher, L. *Advanced Drug Delivery Reviews,* **2015**, *91*, 141–152.
[187] Thomas, D. B.; Convertine, A. J.; Hester, R. D.; Lowe, A. B.; McCormick, C. L. *Macromolecules,* **2004**, *37* (5), 1735–1741.
[188] Andreasen, S. Ø.; Chong, S.-F.; Kryger, M. B. L.; Jensen, B. E. B.; Postma, A.; Alves, M.-H.; Städler, B.; Goldie, K. N.; Zelikin, A. N. *Particle & Particle Systems Characterization,* **2013**, *30* (6), 514–522.
[189] Williams, C. G.; Malik, A. N.; Kim, T. K.; Manson, P. N.; Elisseeff, J. H. *Biomaterials,* **2005**, *26* (11), 1211–1218.
[190] Sanches-Silva, A.; Andre, C.; Castanheira, I.; Cruz, J. M.; Pastorelli, S.; Simoneau, C.; Paseiro-Losada, P. *Journal of Agricultural and Food Chemistry,* **2009**, *57* (20), 9516–9523.
[191] Bail, R.; Patel, A.; Yang, H.; Rogers, C. M.; Rose, F.; Segal, J. I.; Ratchev, S. M. *Procedia CIRP,* **2013**, *5*, 222–225.
[192] Radebner, J.; Eibel, A.; Leypold, M.; Jungwirth, N.; Pickl, T.; Torvisco, A.; Fischer, R.; Fischer, U. K.; Moszner, N.; Gescheidt, G.; Stueger, H.; Haas, M. *Chemistry,* **2018**, *24* (33), 8281–8285.
[193] Tomal, W.; Ortyl, J. *Polymers,* **2020**, *12* (5), 1073.
[194] Löblein, J.; Lorson, T.; Komma, M.; Kielholz, T.; Windbergs, M.; Dalton, P.; Luxenhofer, R. *Beilstein Journal of organic Chemistry,* **2021**, 17, 2095–2101.
[195] Fang, W.-H.; Liu, R.-Z. *Journal of American Chemical Society,* **2000**, *122* (44), 10886–10894.
[196] Liu, S.; Srinivasan, S.; Tao, J.; Grady, M. C.; Soroush, M.; Rappe, A. M. *The Journal of Physical Chemistry A,* **2014**, *118* (40), 9310–9318.
[197] Wang, H.; Brown, H. R. *Macromolecular Rapid Communications,* **2004**, *25* (11), 1095–1099.
[198] Pittman, C. U.; Lai, J. C.; Vanderpool, D. P. *Macromolecules,* **1970**, *3* (1), 105–107.
[199] Buback, M.; Müller, E. *Macromolecular Chemistry and Physics* **2007**, *208* (6), 581–593.
[200] Styan, K. E.; Easton, C. D.; Weaver, L. G.; Meagher, L. *Macromolecular rapid communications,* **2016**, *37* (13), 1079–1086.
[201] Ekblad, T.; Andersson, O.; Tai, F.-I.; Ederth, T.; Liedberg, B. *ACS Journal of Surfaces and Colloids,* **2009**, *25* (6), 3755–3762.
[202] Zhang, N.; Steenackers, M.; Luxenhofer, R.; Jordan, R. *Macromolecules,* **2009**, *42* (14), 5345–5351.
[203] Bai, G.; Ma, S.; Qie, R.; Liu, Z.; Shi, Y.; Li, C.; Wang, R.; Guo, X.; Zhou, F.; Jia, X. *Macromolecular Rapid Communications,* **2016**, *37* (15), 1256–1261.
[204] Wang, W.; Zou, H.; Xing, G.; Shang, M.; Chen, T. *RSC Advances,* **2017**, *7* (45), 28024–28028.
[205] Wang, Q.; Chen, S.; Liang, Y.; Dong, D.; Zhang, N. *Macromolecules* ,**2017**, *50* (21), 8456–8463.
[206] Hafner, D.; Ziegler, L.; Ichwan, M.; Zhang, T.; Schneider, M.; Schiffmann, M.; Thomas, C.; Hinrichs, K.; Jordan, R.; Amin, I. *Advanced Materials,* **2016**, *28* (7), 1489–1494.
[207] Bian, H.; Dong, X.; Chen, S.; Dong, D.; Zhang, N. *Chinese Chemical Letters,* **2018**, *29* (1), 171–174.
[208] Tao Zhang; D. Rodriguez, R.; Amin, I.; Gasiorowski, J.; Rahaman, M.; Sheng, W.; Kalbacova, J.; Sheremet, E.; Zahn, T. D. R.; Jordan, R. *Journal of Materials Chemistry C,* **2018**, *6* (18), 4919–4927.

[209] Hutter, N. A.; Steenackers, M.; Reitinger, A.; Williams, O. A.; Garrido, J. A.; Jordan, R. *Soft matter,* **2011**, *7* (10), 4861.
[210] Yang, W.; Rånby, B. *Journal of Applied Polymer Science,* **1996**, *62* (3), 533–543.
[211] Gam-Derouich, S.; Mahouche-Chergui, S.; Truong, S.; Ben Hassen-Chehimi, D.; Chehimi, M. M. *Polymer,* **2011**, *52* (20), 4463–4470.
[212] Faxälv, L.; Ekblad, T.; Liedberg, B.; Lindahl, T. L. *Acta biomaterialia,* **2010**, *6* (7), 2599–2608.
[213] Hou, L.; Bian, H.; Wang, Q.; Zhang, N.; Liang, Y.; Dong, D. *RSC Advances,* **2016**, *6* (58), 53062–53068.
[214] Steenackers, M.; Sharp, I. D.; Larsson, K.; Hutter, N. A.; Stutzmann, M.; Jordan, R. *Chemistry of Materials,* **2010**, *22* (1), 272–278.
[215] Hou, L.; Liang, Y.; Wang, Q.; Zhang, Y.; Dong, D.; Zhang, N. *ACS Macro Letters,* **2018**, *7* (1), 65–69.
[216] Toader, M.; Schubel, R.; Hartmann, M.; Scharfenberg, L.; Jordan, R.; Mertig, M.; Schulz, S. E.; Gessner, T.; Hermann, S. *Chemical Physics Letters,* **2016**, *661*, 1–5.
[217] Riedel, E. *Anorganische Chemie*, 4. Aufl.; de Gruyter, **1999**.
[218] Gam-Derouich, S.; Mahouche-Chergui, S.; Turmine, M.; Piquemal, J.-Y.; Hassen-Chehimi, D. B.; Omastová, M.; Chehimi, M. M. *Surface Science,* **2011**, *605* (21-22), 1889–1899.
[219] Xiao, P.; Gu, J.; Chen, J.; Zhang, J.; Xing, R.; Han, Y.; Fu, J.; Wang, W.; Chen, T. *Chemcal Communications Journal,* **2014**, *50* (54), 7103–7106.
[220] Gölzhäuser, A.; Wöll, C. *Physical Chemistry Chemical Physics : PCCP,* **2010**, *12* (17), 4273–4274.
[221] Zhang, N.; Pompe, T.; Amin, I.; Luxenhofer, R.; Werner, C.; Jordan, R. *Macromolecular bioscience,* **2012**, *12* (7), 926–936.
[222] Seifert, M.; Koch, A. H. R.; Deubel, F.; Simmet, T.; Hess, L. H.; Stutzmann, M.; Jordan, R.; Garrido, J. A.; Sharp, I. D. *Chemistry of Materials,* **2013**, *25* (3), 466–470.
[223] Rakickas, T.; Ericsson, E. M.; Ruželė, Z.; Liedberg, B.; Valiokas, R. *Small,* **2011**, *7* (15), 2153–2157.
[224] Chen, J.; Xiao, P.; Gu, J.; Huang, Y.; Zhang, J.; Wang, W.; Chen, T. *RSC Advances,* **2014**, *4* (84), 44480–44485.
[225] Nawroth, J. F.; Neisser, C.; Erbe, A.; Jordan, R. *Nanoscale,* **2016**, *8* (14), 7513–7522.
[226] Bian, H.; Yang, J.; Zhang, N.; Wang, Q.; Liang, Y.; Dong, D. *Polymer Chemistry,* **2016**, *7* (5), 1191–1196.
[227] Yang, Y.; Wang, W.; Chen, T.; Chen, Z.-R. *ACS Applied Materials & Interfaces,* **2014**, *6* (23), 21468–21473.
[228] Amin, I.; Steenackers, M.; Zhang, N.; Schubel, R.; Beyer, A.; Gölzhäuser, A.; Jordan, R. *Small,* **2011**, *7* (5), 683–687.
[229] Steenackers, M.; Küller, A.; Stoycheva, S.; Grunze, M.; Jordan, R. *ACS Journal of Surfaces and Colloids,* **2009**, *25* (4), 2225–2231.
[230] Amin, I.; Steenackers, M.; Zhang, N.; Beyer, A.; Zhang, X.; Pirzer, T.; Hugel, T.; Jordan, R.; Gölzhäuser, A. *Small,* **2010**, *6* (15), 1623–1630.
[231] Cėpla, V.; Rakickas, T.; Stankevičienė, G.; Mazėtytė-Godienė, A.; Baradokė, A.; Ruželė, Ž.; Valiokas, R. N. *ACS Applied Materials & Interfaces,* **2020**, *12* (29), 32233–32246.
[232] Gu, J.; Xiao, P.; Chen, J.; Zhang, J.; Huang, Y.; Chen, T. *ACS Applied Materials & Interfaces,* **2014**, *6* (18), 16204–16209.
[233] Di Han; Xiao, P.; Gu, J.; Chen, J.; Cai, Z.; Zhang, J.; Wang, W.; Chen, T. *RSC Advances,* **2014**, *4* (43), 22759.
[234] Zhang, N.; Salzinger, S.; Deubel, F.; Jordan, R.; Rieger, B. *Journal of the American Chemical Society,* **2012**, *134* (17), 7333–7336.

[235] Sun, Y.; Yang, Z.; Li, L.; Wang, Z.; Sun, Q. *Journal of Membrane Science,* **2019**, *581*, 224–235.
[236] Chen, J.; Chen, K.; Tong, D.; Huang, Y.; Zhang, J.; Xue, J.; Huang, Q.; Chen, T. *Chemical Communications,* **2015**, *51* (2), 314–317.
[237] Wadsworth, B. L.; Beiler, A. M.; Khusnutdinova, D.; Jacob, S. I.; Moore, G. F. *ACS Catalysis,* **2016**, *6* (12), 8048–8057.
[238] Men, Y.; Xiao, P.; Chen, J.; Fu, J.; Huang, Y.; Zhang, J.; Xie, Z.; Wang, W.; Chen, T. *ACS Journal of Surfaces and Colloids,* **2014**, *30* (16), 4863–4867.
[239] Hou, Y.; Xiao, P.; Zhang, J.; Peng, M.; Lu, W.; Huang, Y.; Ouyang, C.; Chen, T. *RSC Advances,* **2015**, *5* (75), 60990–60992.
[240] Neuhaus, S.; Padeste, C.; Spencer, N. D. *ACS Journal of Surfaces and Colloids,* **2011**, *27* (11), 6855–6861.
[241] Peng, M.; Xiao, P.; Huang, Y.; Cai, M.; Hou, Y.; Chen, J.; Liu, Z.; Xiao, Z.; Chen, T. *Journal of Materials Chemisrty C,* **2015**, *3* (33), 8659–8664.
[242] Zhai, Q.; Jiang, H.; Zhang, X.; Li, J.; Wang, E. *Talanta* ,**2016**, *149*, 280–284.
[243] Zhou, Y.; Zhang, N.; Zhou, X.; Hu, Y.; Hao, G.; Li, X.; Jiang, W. *Industrial Engineering Chemisrty Research,* **2019**, *58* (8), 3249–3257.
[244] Rahimpour, A.; Madaeni, S. S.; Zereshki, S.; Mansourpanah, Y. *Applied Surface Science,* **2009**, *255* (16), 7455–7461.
[245] Krawicz, A.; Yang, J.; Anzenberg, E.; Yano, J.; Sharp, I. D.; Moore, G. F. *Journal of the American Chemical Society,* **2013**, *135* (32), 11861–11868.
[246] Xiao, P.; Gu, J.; Chen, J.; Di Han; Zhang, J.; Cao, H.; Xing, R.; Han, Y.; Wang, W.; Chen, T. *Chemical communications,* **2013**, *49* (95), 11167–11169.
[247] Sheng, W.; Amin, I.; Neumann, C.; Dong, R.; Zhang, T.; Wegener, E.; Chen, W.-L.; Förster, P.; Tran, H. Q.; Löffler, M.; Winter, A.; Rodriguez, R. D.; Zschech, E.; Ober, C. K.; Feng, X.; Turchanin, A.; Jordan, R. *Small,* **2019**, *15* (19), e1805228.
[248] Steenackers, M.; Lud, S. Q.; Niedermeier, M.; Bruno, P.; Gruen, D. M.; Feulner, P.; Stutzmann, M.; Garrido, J. A.; Jordan, R. *Journal of the American Chemical Society,* **2007**, *129* (50), 15655–15661.
[249] Hou, L.; Fang, J.; Wang, W.; Xie, Z.; Dong, D.; Zhang, N. *Journal of materials chemistry B,* **2017**, *5* (18), 3348–3354.
[250] Hess, L. H.; Lyuleeva, A.; Blaschke, B. M.; Sachsenhauser, M.; Seifert, M.; Garrido, J. A.; Deubel, F. *ACS Applied Materials & Interfaces,* **2014**, *6* (12), 9705–9710.
[251] Gupta, S.; Agrawal, M.; Conrad, M.; Hutter, N. A.; Olk, P.; Simon, F.; Eng, L. M.; Stamm, M.; Jordan, R. *Advanced Functional Materials,* **2010**, *20* (11), 1756–1761.
[252] Gu, J.; Xiao, P.; Chen, J.; Liu, F.; Huang, Y.; Li, G.; Zhang, J.; Chen, T. *Journal of Materials Chemistry A,* **2014**, *2* (37), 15268.
[253] Ye, Q.; Xiao, P.; Liu, W.; Chen, K.; Chen, T.; Xue, J.; Du, S.; Huang, Q. *RSC Advances,* **2015**, *5* (86), 70339–70344.
[254] Men, Y.; Wang, W.; Xiao, P.; Gu, J.; Sun, A.; Huang, Y.; Zhang, J.; Chen, T. *RSC Advances,* **2015**, *5* (40), 31519–31524.
[255] Xiao, P.; Gu, J.; Wan, C.; Wang, S.; He, J.; Zhang, J.; Huang, Y.; Kuo, S.-W.; Chen, T. *Chemistry of Materials,* **2016**, *28* (19), 7125–7133.
[256] Xiao, P.; Gu, J.; He, J.; Wang, S.; Zhang, J.; Huang, Y.; Kuo, S.-W.; Chen, T. *Journal of Materials Chemistry C,* **2016**, *4* (41), 9750–9755.
[257] Sheng, W.; Li, W.; Yu, B.; Li, B.; Jordan, R.; Jia, X.; Zhou, F. *Angewandte Chemie,* **2019**, *58* (35), 12018–12022.
[258] Bian, H.; Zhang, X.; Huang, D.; Zhang, N. *Chinese Chemical Letters,* **2019**, *30* (2), 311–313.

[259] Sheng, W.; Li, W.; Tan, D.; Zhang, P.; Zhang, E.; Sheremet, E.; Schmidt, B. V. K. J.; Feng, X.; Rodriguez, R. D.; Jordan, R.; Amin, I. *ACS Applied Materials & Interfaces,* **2020**, *12* (8), 9797–9805.
[260] Zheng, J.; Xiao, P.; Liu, W.; Zhang, J.; Huang, Y.; Chen, T. *Macromolecular Rapid Communications,* **2016**, *37* (3), 265–270.
[261] Xiao, P.; Du, S.; Zhang, T.; Qiu, N.; Zhang, J.; Huang, Y.; Wan, C.; Jordan, R.; Huang, Q.; Liu, Z.; Chen, T. *Advanced Materials Interfaces,* **2017**, *4* (3), 1600867.
[262] Xiao, P.; Qiu, N.; Gu, J.; Wang, S.; He, J.; Huang, C.-F.; Zhang, J.; Huang, Y.; Chen, T. *Chemical communications,* **2017**, *53* (12), 1949–1952.
[263] Xing, G.; Wang, W.; Wang, K.; Li, P.; Chen, T. *Chemistry,* **2017**, *23* (69), 17549–17555.
[264] Feng, L.; Wang, K.; Li, P.; Wang, W.; Chen, T. *New Journal of Chemistry,* **2018**, 42,17016-17020.
[265] Chen, J.; Ma, X.; Gnanasekar, P.; Qin, D.; Luo, Q.; Sun, Z.; Zhu, J.; Yan, N. *New Journal of Chemistry,* **2020**, *44* (45), 19440–19444.
[266] Zhu, H.; Mumtaz, F.; Zhang, C.; Tan, L.; Liu, S.; Zhang, Y.; Pan, C.; Wang, Y. *Applied Surface Science,* **2017**, *426*, 817–826.
[267] Ederth, T.; Ekblad, T. *ACS Journal of Surfaces and Colloids,* **2018**, *34* (19), 5517–5526.
[268] Kasprów, M.; Machnik, J.; Otulakowski, Ł.; Dworak, A.; Trzebicka, B. *RSC Advances,* **2019**, *9* (70), 40966–40974.
[269] Davison III, G. R.; Peppas, N. A. *Journal of Controlled Release,* **1986** (3), 243–258.
[270] Hill, D. J.; O'Donnell, J. H.; Pomery, P. J.; Whittaker, M. R. *Polymer Gels and Networks,* **1995** (3), 85–97.
[271] Komma, M., *Oberflächenmodifikation von Poly(ε-caprolacton) Scaffolds mittels Self-Initiated Photografting and Photopolymerisation*, **2015**.
[272] Ziegler, S., *UV-initiierte Oberflächenmodifikation von Poly-ε-Caprolacton mit verschiedenen Methacrylaten im kontinuierlichen Monomerstrom,* **2016**.
[273] Alexander, M. R.; Williams, P. *Biointerphases,* **2017**, *12* (2), 02C201.
[274] Menzies, K. L.; Jones, L. *Optometry and Vision Science,* **2010** (87), 387–399.
[275] Faucheux, N.; Schweiss, R.; Lützow, K.; Werner, C.; Groth, T. *Biomaterials,* **2004**, *25* (14), 2721–2730.
[276] Lee; Khang. *Journal of colloid and interface science,* **2000**, *230* (1), 84–90.
[277] Miller, A. A.; Mayo, F. R. *Journal of American Chemical Society,* **1956**, 78 (5), 1017-1023.
[278] Mayo, R. R.; Miller, A. A. *Journal of American Chemical Society,* **1956**, 78 (5), 1023-1034.
[279] Scherzer, T.; Langguth, H. *Macromolecular Chemistry Physics,* **2005**, *206* (2), 240–245.
[280] Scherzer, T.; Decker, U. *Polymer,* **2000**, *41* (21), 7681–7690.
[281] Bhanu, V. A.; Kishore, K. *Chemical Reviews*, **1991**, 91 (2) 99-117.
[282] Glock, J., *Self-Initiated Photografting and Photopolymerization von Methacrylaten auf Polyvinylidenfluorid-Terpolymer- Filmen,* **2019**.
[283] Dušička, E.; Nikitin, A. N.; Lacík, I. *Polymer Chemistry,* **2019**, *10* (43), 5870–5878.
[284] Varma, I. K.; Patnaik, S. *European Polymer Journal,* **1977** (13), 175–178.
[285] Miao, J.; Cheng, Z.; Zhou, M.; Pan, D. *Journal of Macromolecular Science, Part A,* **2012**, *49* (10), 869–875.
[286] Barson, C. A.; Turner, M. J. *European Polymer Journal,* **1974** (10), 1053–1055.
[287] Kursawe, M.; Glaubitt, W.; Thierauf, A. *Journal of Sol-Gel Science and Technology,* **1998** (13), 267–271.

Curriculum Vitae

03/2018-05/2021	PhD student at the University of Würzburg, Chair of Chemical Technology of Material Synthesis; Supervisor: Prof. Dr. Robert Luxenhofer
02/2019-02/2021	Scientific assistant at Initiative junge Forscherinnen und Forscher e.V.
11/2017-02/2018	Research assistant at Fraunhofer ISC, Würzburg; Optics and Electronic
10/2014-6/2017	Master of Science, Chemistry, University of Würzburg; Supervisor: Prof. Dr. Peer Löbmann
10/2010-10/2014	Bachelor of Science, Chemistry, University of Würzburg: Supervisor: Prof. Dr. Maik Finze

Jochen Löblein, Würzburg

Affidavit

I hereby confirm that my thesis entitled "Development of Dynamic Self-Initiated Photografting and Photopoly-merization" is the result of my own work. I did not receive any help or support from commercial consultants. All sources and / or materials applied are listed and specified in the thesis.

Furthermore, I confirm that this thesis has not yet been submitted as part of another examination process neither in identical nor in similar form.

Place, Date Signature

Eidesstattliche Erklärung

Hiermit erkläre ich an Eides statt, die Dissertation "Entwicklung von dynamischem Self-Initiated Photografting and Photopolymerization" eigenständig, d.h. insbesondere selbständig und ohne Hilfe eines kommerziellen Promotionsberaters, angefertigt und keine anderen als die von mir angegebenen Quellen und Hilfsmittel verwendet zu haben.

Ich erkläre außerdem, dass die Dissertation weder in gleicher noch in ähnlicher Form bereits in einem anderen Prüfungsverfahren vorgelegen hat.

Ort, Datum Unterschrift